

Electronic Thesis and Dissertation Repository

---

12-12-2013

## A single cell based model for cell divisions with spontaneous topology changes

Anna Mkrтчyan  
*The University of Western Ontario*

Supervisor  
Dr. Mikko Karttunen  
*The University of Western Ontario*

Graduate Program in Applied Mathematics  
A thesis submitted in partial fulfillment of the requirements for the degree in Doctor of Philosophy  
© Anna Mkrтчyan 2013

Follow this and additional works at: <https://ir.lib.uwo.ca/etd>

---

### Recommended Citation

Mkrтчyan, Anna, "A single cell based model for cell divisions with spontaneous topology changes" (2013). *Electronic Thesis and Dissertation Repository*. 1814.  
<https://ir.lib.uwo.ca/etd/1814>

This Dissertation/Thesis is brought to you for free and open access by Scholarship@Western. It has been accepted for inclusion in Electronic Thesis and Dissertation Repository by an authorized administrator of Scholarship@Western. For more information, please contact [wlsadmin@uwo.ca](mailto:wlsadmin@uwo.ca).

A SINGLE CELL BASED MODEL FOR CELL DIVISIONS WITH  
SPONTANEOUS TOPOLOGY CHANGES  
(Thesis format: Monograph)

by

Anna Mkrtchyan

Graduate Program in Applied Mathematics

A thesis submitted in partial fulfillment  
of the requirements for the degree of  
Doctor of Philosophy

The School of Graduate and Postdoctoral Studies  
The University of Western Ontario  
London, Ontario, Canada

© Anna Mkrtchyan 2013

# Abstract

The development of multicellular organisms is accompanied by the formation of tissues of precise shapes, sizes and topologies. Remarkable similarities between tissue topologies, in particular proliferating epithelial topologies, in various species suggest that the mechanisms that govern the formation of tissues are conserved among species. To understand these mechanisms various models have been developed.

In this thesis, we present a novel mechanical model for cell divisions and tissue formation. The model accounts for cell mechanics and cell-cell adhesion. In our model, each cell is treated individually, thus the changes in cell's shape and its local rearrangements occur naturally as a response to the evolving cellular environment and cell-cell interactions. We introduce the processes of cell growth and divisions and numerically simulate tissue proliferation. As tissue grows starting from few cells, we follow the dynamics of the tissue growth and cell packing topologies. The outcomes are compared with experimental observations in *Drosophila* wing growth. Our model accounts for the exponential decay of the mitotic index and reproduces commonly observed cell packing topologies in proliferating epithelia.

Next, we consider two biologically relevant division schemes, namely, division through asymmetric division plane and division by Hertwig's rule. We study the impact of division planes on tissue growth and show that the division plane may affect cell packing topologies. Development of the tissue is accompanied by cellular rearrangements. We vary the extent of cellular rearrangements and analyse their effects on tissue topology. We find that when cells are allowed to move freely, more organized packing topologies emerge.

**Keywords:** Cell division; proliferation; tissue topology; tissue growth; sub-cellular element model.

# Statement of Co-Authorship

The article versions of Chapters 4 and 5 are co-authored with Jan Åström and Mikko Karttunen. All the simulations, analysis and large majority of programming were made by the author.

# Acknowledgements

First and foremost, I would like to thank my supervisor, Dr. Mikko Karttunen, for his guidance, support and encouragement. This work would not be possible without him.

I would also like to thank Dr. Jan Åström for the inspiring discussions, interesting suggestions and comments. I am grateful to my supervisory committee, Dr. Volodya Miransky, whose interest in my work and kind attention (and apples) have been very helpful, and Dr. Colin Denniston for his insightful comments. Dr. Ortrud Wartlick helped me to understand her experimental work and I am thankful for that.

Throughout my years in the Department of Applied Mathematics I enjoyed the friendly and supportive atmosphere. I am thankful to all the professors, graduate students, Audrey, Karen and Cinthia for their assistance and encouragement.

Many thanks to Mona, Frances, Susanna, Jingya and Wenjing. Our friendship has been great for me. Special thanks to Bernard for his continuous support, encouragement and valuable advice.

I am especially grateful to my mother and my brother for their love and encouragement throughout all these years.

Thank you everyone for making this work possible.

# Contents

|  |            |
|--|------------|
| <b>Abstract</b>  | <b>ii</b>  |
| <b>Statement of Co-Authorship</b>                            | <b>iii</b> |
| <b>Acknowledgements</b>                                      | <b>iv</b>  |
| <b>Table of Contents</b>                                     | <b>v</b>   |
| <b>List of Figures</b>                                       | <b>vi</b>  |
| <b>List of Abbreviations, Symbols, and Nomenclature</b>      | <b>ix</b>  |
| <b>1 Introduction</b>  | <b>1</b>   |
| <b>2 Biological Background</b>                               | <b>5</b>   |
| 2.1 Cell Structure . . . . .                                 | 5          |
| 2.1.1 Chromosomes and Nucleus . . . . .                      | 6          |
| 2.1.2 Plasma Membrane . . . . .                              | 8          |
| 2.1.3 Cytoskeleton . . . . .                                 | 10         |
| 2.2 Cell Cycle . . . . .                                     | 12         |
| 2.3 Structure and Development of Epithelial Tissue . . . . . | 17         |
| 2.4 Cell Packing in Proliferating Epithelia . . . . .        | 20         |
| 2.5 Models For Tissue Growth and Morphology . . . . .        | 23         |
| <b>3 Physical and Numerical Background</b>                   | <b>28</b>  |
| 3.1 Physical Background . . . . .                            | 28         |
| 3.1.1 Elasticity . . . . .                                   | 29         |
| 3.1.2 Viscosity . . . . .                                    | 32         |
| 3.1.3 Inter-membrane adhesion . . . . .                      | 34         |
| 3.2 Numerical Methods . . . . .                              | 37         |

|          |  |            |
|----------|--|------------|
| 3.2.1    | Introduction . . . . .   | 37         |
| 3.2.2    | Equations of Motion . . . . .  | 39         |
| 3.2.3    | Numerical Integration . . . . .  | 40         |
| 3.2.4    | Initial and Boundary Conditions . . . . .  | 42         |
| 3.2.5    | Packing of particles: Voronoi Diagram . . . . .  | 45         |
| <b>4</b> | <b>Model and Methods</b>   | <b>48</b>  |
| 4.1      | Model . . . . .  | 49         |
| 4.1.1    | Isolated Cell . . . . .  | 49         |
| 4.1.2    | Cell in tissue . . . . .   | 49         |
| 4.1.3    | Cellular processes . . . . .   | 52         |
| 4.2      | Numerical Implementation . . . . .   | 54         |
| 4.2.1    | Simulation of Tissue Growth . . . . .  | 55         |
| 4.2.2    | Parametrization . . . . .  | 56         |
| 4.3      | Summary . . . . .  | 59         |
| <b>5</b> | <b>The Dynamics of Proliferating Epithelium</b>  | <b>60</b>  |
| 5.1      | Time evolution of mitotic index . . . . .  | 61         |
| 5.2      | Cell packing topology . . . . .  | 63         |
| 5.3      | Summary . . . . .  | 66         |
| <b>6</b> | <b>Influence of Division Plane and Cellular Rearrangements</b>                                   | <b>70</b>  |
| 6.1      | The effect of asymmetric division and division by Hertwig's rule on tissue topology . . . . .    | 71         |
| 6.2      | The effect of cellular rearrangements influenced by viscous damping on tissue topology . . . . . | 77         |
| 6.3      | Summary . . . . .  | 82         |
| <b>7</b> | <b>Conclusions and Future Works</b>  | <b>87</b>  |
| 7.1      | Conclusions . . . . .  | 87         |
| 7.2      | Future Work . . . . .  | 89         |
|          | <b>Bibliography</b>  | <b>90</b>  |
|          | <b>Curriculum Vitae</b>  | <b>102</b> |

# List of Figures

|      |   |    |
|------|---|----|
| 1.1  | Sand dollar zygote during first mitosis . . . . .                                 | 2  |
| 2.1  | Prokaryotic Cell . . . . .  | 6  |
| 2.2  | Eukaryotic Cell . . . . .   | 7  |
| 2.3  | Plasma Membrane of the Cell . . . . .   | 9  |
| 2.4  | Structures formed by actin filaments . . . . .                                    | 11 |
| 2.5  | Cell cycle diagrams for prokaryotic and eukaryotic cells . . . . .                | 13 |
| 2.6  | Mitotic spindle . . . . .   | 15 |
| 2.7  | Cell packing topologies . . . . .   | 17 |
| 2.8  | <i>Drosophila</i> wing imaginal disc . . . . .                                    | 19 |
| 2.9  | Distribution of cell polygon types in proliferating epithelia . . . . .           | 21 |
| 2.10 | Vertex model of the cell . . . . .  | 24 |
| 2.11 | Viscoelastic model of the cell . . . . .  | 25 |
| 2.12 | Newman's model of the cell . . . . .  | 26 |
| 3.1  | Deformation of an elastic body . . . . .  | 29 |
| 3.2  | Two-dimensional normal and shear strains . . . . .                                | 30 |
| 3.3  | Velocity gradient in a fluid under shear flow . . . . .                           | 33 |
| 3.4  | The Lennard-Jones potential . . . . .   | 36 |
| 3.5  | Periodic Boundary Condition . . . . .   | 44 |
| 3.6  | Minimum image convention . . . . .  | 45 |
| 3.7  | A two dimensional Voronoi diagram for a random set of points . . . . .            | 46 |
| 4.1  | Mass-spring model of the cell . . . . .   | 50 |
| 4.2  | Three mechanisms of cell division . . . . .                                       | 53 |
| 4.3  | Data are collected from the central part of the tissue . . . . .                  | 56 |
| 4.4  | Initial configuration of four simulation samples . . . . .                        | 56 |
| 5.1  | Mitotic index of <i>Drosophila</i> wing disc determined by PH3-staining . . . . . | 61 |
| 5.2  | Snapshots of tissue growth through random symmetric division line . . . . .       | 62 |



|      |   |    |
|------|---|----|
| 5.3  | Time evolution of simulated mitotic index . . . . .   | 63 |
| 5.4  | Spatial distribution of mitotic cells for proliferation time interval . . . .   | 64 |
| 5.5  | Averaged spatial distribution of mitotic indices . . . . .  | 65 |
| 5.6  | The Voronoi diagram of simulated tissue . . . . .   | 65 |
| 5.7  | Time evolution of the polygon type distribution for four simulation sam-<br>ples . . . . .  | 67 |
| 5.8  | Polygon type distribution compared with experimentally observed topol-<br>ogy of <i>Drosophila</i> wing epithelium topology . . . . . | 68 |
|      |   |    |
| 6.1  | The ratio of small and large cell areas during the asymmteric division . .  | 71 |
| 6.2  | Snapshots from a simulation of tissue growth through asymmetric cell<br>division . . . . .  | 72 |
| 6.3  | Snapshots from a simulation of tissue growth through Hertwig's divi-<br>sion rule . . . . .   | 73 |
| 6.4  | Mitotic index for asymmetric division plane . . . . .   | 73 |
| 6.5  | Mitotic index for longest axis division plane . . . . .   | 74 |
| 6.6  | Comparison of mitotic indices for three division schemes . . . . .  | 75 |
| 6.7  | Time evolution of the polygon type distribution for the asymmetric di-<br>vision scheme . . . . .                                     | 76 |
| 6.8  | Time evolution of the polygon type distribution for Hertwig's division<br>scheme . . . . .  | 77 |
| 6.9  | Cell polygon type distributions for three division schemes . . . . .  | 78 |
| 6.10 | Snapshots of simulated tissue growth for damping coefficient $\gamma = 10$ . .  | 79 |
| 6.11 | Snapshots of simulated tissue growth for damping coefficient $\gamma = 0$ . .   | 80 |
| 6.12 | Snapshots of the Voronoi diagrams of the tissue for three different sce-<br>narios of cellular rearrangements . . . . .               | 80 |
| 6.13 | Mitotic index for the case of unrestricted cellular rearrangements . . . .  | 81 |
| 6.14 | Mitotic index for the case of cellular rearrangements defined by viscous<br>damping with the coefficient $\gamma = 10$ . . . . .      | 81 |
| 6.15 | Comparison of mitotic indices for three various amounts of cellular re-<br>arrangements . . . . .                                     | 82 |
| 6.16 | Time evolution of the polygon type distribution for the $\gamma = 10$ case . . .  | 83 |
| 6.17 | Time evolution of the polygon type distribution for the $\gamma = 0$ case . . .   | 84 |
| 6.18 | Polygon type distribution for various amount of cell rearrangements. . .  | 85 |

# List of Abbreviations, Symbols, and Nomenclature

## Abbreviations

|               |  |
|---------------|--|
| DNA           | Deoxyribonucleic acid                      |
| IF            | Intermediate filament                      |
| MT            | Microtubule                                |
| MCA           | Membrane-to-cortex attachment              |
| MTOC          | Microtubule-organizing centres             |
| E. coli       | Escherichia coli                           |
| C. crescentus | Caulobacter crescentus                     |
| B. subtilis   | Bacillus subtilis                          |
| oriC          | Origin of replication                      |
| ter           | Terminus of replication                    |
| CAM           | Cell adhesion molecule                     |
| FtsZ          | Filamenting Temperature-Sensitive Mutant Z |
| MD            | Molecular dynamics                         |
| CG            | Coarse grained                             |
| PBC           | Periodic boundary condition                |
| VDW           | Van der Waals potential                    |
| LJ            | Lennard-Jones potential                    |

# Chapter 1

## Introduction

Cells are the smallest structural and functional units of living organisms. They are often called the “building blocks of life”. Each cell stores the necessary information for its existence, is capable of getting energy from interactions with its environment and has the ability to evolve, regenerate and replicate [1]. Some organisms, such as bacteria and yeast, consist of a single cell, while others, called multicellular organisms, may contain trillions of cells. For instance, humans consist of up to 100 trillion cells of varying kinds and functionality [2].

One of the most fundamental properties of the cell is their ability to replicate. Cells replicate through division (Fig. 1.1). The cell division cycle is a highly regulated multistage process, during which the parental cell gives rise to two daughter cells [4, 5]. It is hard to overstate the importance of cell division. During the lifetime of the human body, for example, about 10,000 trillion cell divisions occur [6]. Precise cell divisions are necessary for proper tissue development, cell differentiation and renewal. Abnormalities in cell divisions result in various diseases, cancer among them [7, 8, 9]. Mitosis has been studied since early 1880s, when Flemming first observed mitotic cells. Much work has been done to understand the molecular machinery of cell divisions, their regulatory mechanisms and the proteins participating in mitosis [10]. Recent studies show that cell divisions are not only governed by the signalling of molecules, but also depend upon cell mechanics. Mechanical forces ensure mitotic cells have a rounded shape before the division [11]. They define the selection of the division plane [12, 13]. During cytokinesis and cell migrations, cell shape changes rely on the mechanical properties of the cell’s cortex [14, 4, 15]. Thus, cell divisions are complex processes that depend on both molecular signals encoded in genes and cell mechanics.

Cell division is the mechanism by which multicellular organisms develop from a

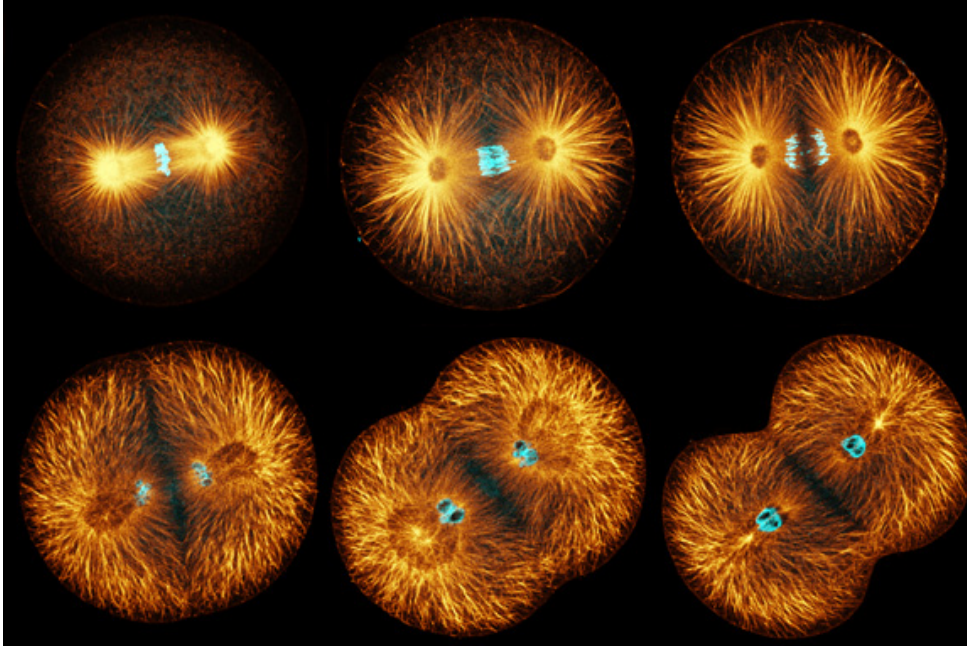


Figure 1.1: Sand dollar zygote during first mitosis. Staining highlights microtubules and chromosomes. Top panel: mitotic spindle segregates chromosomes. Bottom panel: successive stages of cortical contraction during cytokinesis. Image is taken by George von Dassow (adapted from [3] with the George von Dassow's permission)

single fertilized egg cell. During development, a series of mitoses produces tissues of various shapes and sizes. Tissue in its functional form has a specific shape, size and topology. One example is the packing of cells in the vertebrate's eye lens [16]. Fibre cells are tightly packed into a hexagonal structure. This structure minimizes light scattering by cell membranes, which is essential for transparency of the lens. Another example is the hexagonal packing of cells in the *Drosophila* fruit fly wing. Regular spacing of wing cells define the regular spacing of wing hair, essential for air flow guidance during flight [17]. Mechanisms that govern tissue growth and morphogenesis are not completely understood [18]. They regulate tissue topology by means of a few cellular processes, most importantly, through cell divisions [19]. Understanding the processes involved in cells divisions, as well as their impact on tissue formation is one of the challenges in developmental biology.

Computer simulations are often used to predict the behaviour of biological systems [20]. Simulations are run on model systems, which approximate real systems with some degree of accuracy. The extent of details of the real system that should be included in the model depends on the phenomenon of interest, its length and time

scales [21]. For example, in studies of transportation through the cell membrane, the latter is modelled as a bilayer of lipid molecules [22], whereas studies of red blood cell shapes treat the membrane as an elastic sheet [23]. Cellular processes in tissue have different time scales. Processes involving relaxation of cell shapes take several minutes, cell divisions happen within hours and tissue morphogenesis may take several days [24]. As for the length scales, they range from nanometres (various cellular components) to micrometers (cells themselves) to millimetres and higher (tissues) [2]. These time and length scales exceed typical scales of all atom classical molecular dynamics simulations, and a coarse-grained modelling approach should be used.

Models with various degrees of coarse-graining have been used to address the effects of proliferation on tissue development [25, 26, 27, 28, 29, 30, 31, 32]. In particular, vertex models are a common choice to examine the effects of cell divisions on tissue growth and cell packing topology. Vertex models are inspired by the structure of epithelial tissue, commonly used as a model system [27]. In epithelium, cells tightly adhere to their neighbors and display little rearrangement during tissue development [19]. Such tissue can be described as a polygonal network, where each polygon represents a cell [27]. Vertex models have been used to study the effects of cell mechanics, proliferation and growth control on tissue topology [28, 27, 33, 34]. Lack of extensive cell rearrangements and tight packing justifies the modelling of cell shape and topology through its neighbors. A more realistic approach is to model each cell independently. Existing single cell based models have been used to study a wide range of processes in multicellular systems [32, 35, 36, 37, 38, 39]. However, only a few recent works address topological patterning [39].

In this thesis, we develop a novel mechanical single-cell based model to study the dynamics of tissue growth and the emergence of cell packing topologies in epithelium-like tissues. The advantages of using a model in which each cell is treated individually, include a more realistic and detailed description of the cell shapes, a more natural response of cell to external stimuli and the ability to incorporate cell migrations, that are common in various biological processes [40, 9].

This thesis is organized as follows. In Chapter 2, background on biological aspects of cell divisions, tissue formation and cell packing topologies are presented. Selected models, previously used to explore tissue growth and formation, are discussed as well. Chapter 3 introduces the physical and numerical background relevant to this work. We present the details of our model in Chapter 4 along with the parametrization and simulation details. In Chapter 5 we follow the dynamics of epithelial tissue proliferation,

when the proliferation mechanism is similar to the one observed experimentally in the development of *Drosophila* wing epithelium [19]. Alternative proliferation schemes are explored in Chapter 6. Finally, we present our conclusions in Chapter 7.

# Chapter 2

## Biological Background

### 2.1 Cell Structure

There are two classes of cells: prokaryotic and eukaryotic cells. Bacteria and archaea belong to prokaryotes, whereas all animal, plant and fungi are eukaryotes [2].

Prokaryotic cells have a relatively simple structure (Fig. 2.1). These are small cells, with an average diameter of about 1 to 10  $\mu\text{m}$  [41]. A prokaryotic cell is enclosed in a cell envelope, consisting of a capsule, a rigid cell wall, and a plasma membrane. Some bacteria also have an outer membrane, located between the cell wall and capsule. Both the capsule and the cell wall provide structural support to the cell and protection from the external environment [42]. The main difference between prokaryotes and eukaryotes is the lack of compartments in prokaryotic cells. The plasma membrane in prokaryotes forms a single closed compartment filled with aqueous solution, or cytoplasm, where genetic material is dissolved along with other contents of the cell.

Eukaryotic cells are bigger, with an average diameter of 10 – 100  $\mu\text{m}$ . Unlike prokaryotic cells, the interior of an eukaryotic cell is divided into several compartments, each with its specific function. These compartments are called organelles. Each organelle is separated from the rest of the cell interior by a membrane, and the entire cell itself is encapsulated in a plasma membrane.

Although animal and plant cells belong to the same class of eukaryotes, they are structurally and functionally different. Plant cells have rigid cell walls, which define their rectangular shapes. Animal cells, on the contrary, lack cell walls and have irregular shapes. Due to the absence of rigid cell walls, animal cells are flexible and mobile, whereas plant cells are immobile inside the tissue. Schematic structures of eukaryotic animal and plant cells are shown in Figure 2.2.

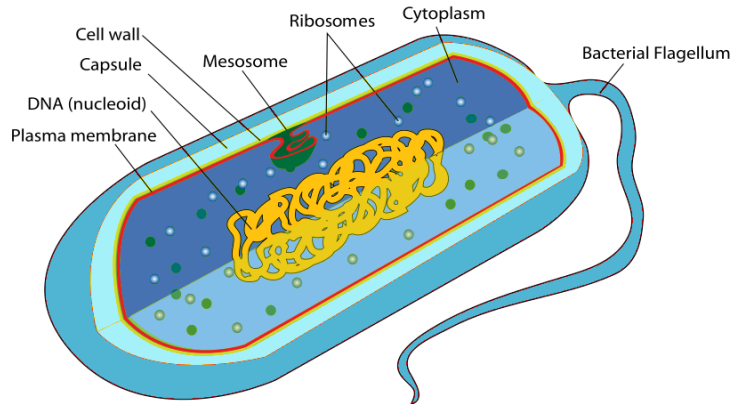


Figure 2.1: Prokaryotic Cell. Plasma membrane encapsulates cell, which is filled with cytoplasm. Prokaryotic cells lack a nucleus. Source: wikipedia:prokaryote cell diagram. This picture is available under the Creative Commons License.

In the following sections we briefly review organelles and structures of cell that are related to the process of cell division.

### 2.1.1 Chromosomes and Nucleus

In both prokaryotic and eukaryotic cells, the genome is encoded in large macromolecules, called DNA. Most prokaryotes have a single circular DNA molecule, while the genome in eukaryotes is encoded in multiple DNA molecules [41]. The entire length of extended DNA molecules can achieve orders of millimetres for prokaryotes and meters for eukaryotes [41]. For example, the total DNA length in a human cell is about 2 m [43]. In order to fit into small spaces, namely prokaryotic cells or nuclei with diameters of  $\mu\text{ms}$ , DNA undergoes compaction by forming complexes with proteins [43]. Below, we describe the organization of DNA in eukaryotic cells based on the review of Ref. [43]. In eukaryotes, DNA first wraps about 2 turns around proteins called histones. This DNA-histone complex is called the nucleosome. Linear chains of nucleosomes form a fibre-like structure 10 nm in diameter, known as a chromatin. In the next organization levels, chromatin can further fold on itself and form even denser structures, called chromosomes. While a higher level of condensation makes chromatin more compact, it also blocks access to genetic information. The compaction of chromatin varies throughout the cell cycle in eukaryotes. It is relatively decondensed in the stages where the cell grows and replicates its genetic material, and achieves its maximum condensation right before the division.



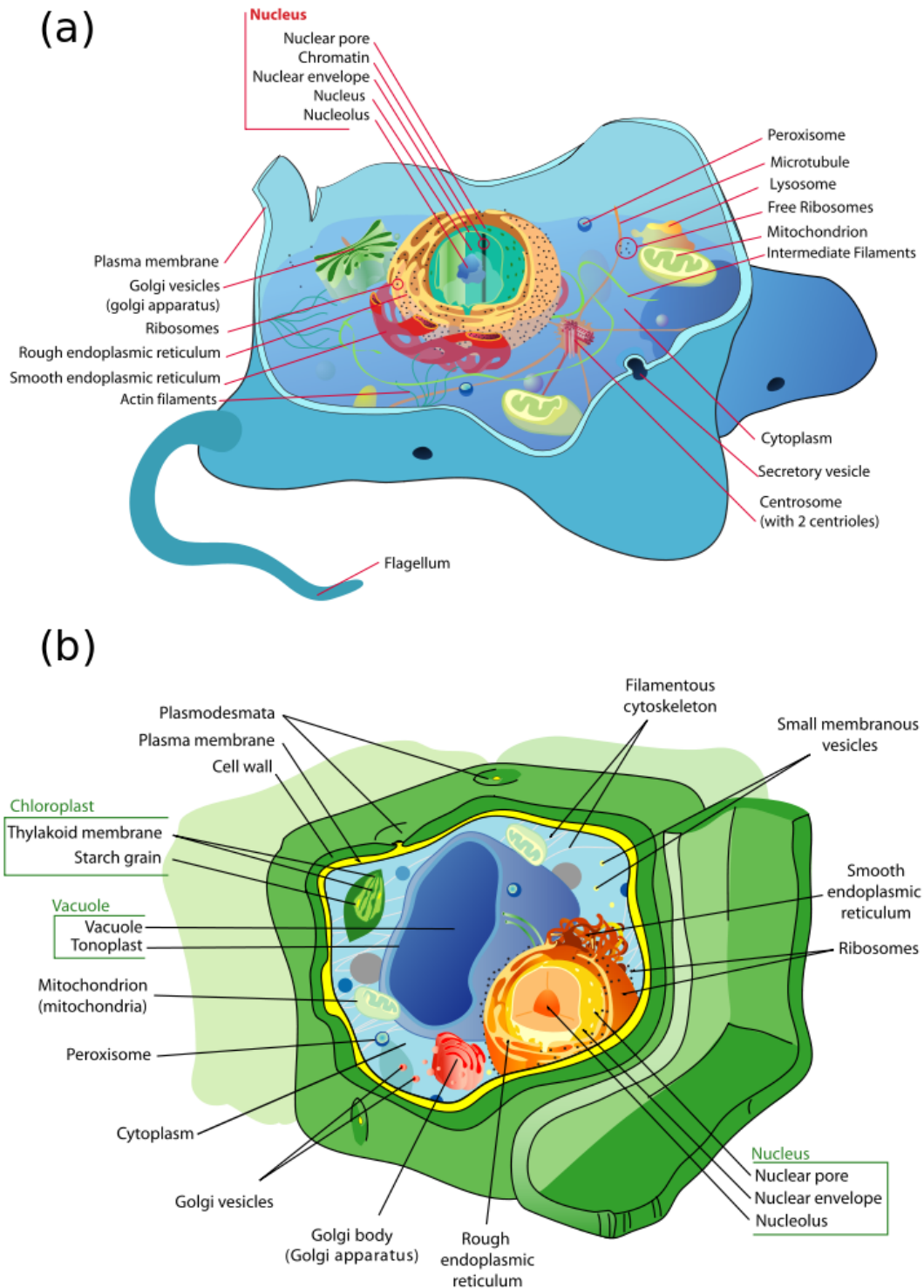


Figure 2.2: Eukaryotic Cell: Eukaryotic cell consists of different organelles with specific functions. Unlike prokaryotes, DNA is stored in the nucleus (a) Animal cell structure (b) Plant cell structure. Source: wikipedia:animal cell structure, plant cell structure. This picture is available under the Creative Commons License.

The eukaryotic cell isolates the genome from the rest of the cell in the nucleus [41]. The nucleus has a diameter of 5-10  $\mu\text{m}$ . The content of the nucleus is enclosed in a nuclear envelope, which supports the structure of the nucleus and acts as a barrier against the contents of cytoplasm. The nucleus not only stores the genome, but also provides an environment for selective access to it. The prokaryotic cell lacks a nucleus. Its chromosome is dissolved in the cytoplasm and is located in the central part of the cell.

### 2.1.2 Plasma Membrane

Membranes play an important role in numerous biological processes. They define intracellular compartments, isolate cell contents from the extracellular environment and provide pathways for transporting molecules in and out of the compartments or cell. The plasma membrane participates in cell-cell signalling [44] and in processes involving cell shape changes, such as cell movements and cell divisions [14, 45].

Lipids are the major components of membranes. The amount and type of lipids in a membranes varies, depending on the type of membrane. Most cell membranes, the plasma membrane in particular, consist of approximately 50% lipids and the remaining 50% are proteins [41].

Lipids are amphiphilic. They consist of hydrophobic hydrocarbon chains and a polar head group. In aqueous solution, hydrophobic groups tend to minimize their unfavourable contacts with water. Hydrophilic head groups, on the contrary, favour interactions with water. As a result, when lipids are dissolved in water, they spontaneously aggregate into complexes, where polar head groups are exposed to water, while hydrophobic chains are buried inside. These complexes are stabilized by hydrophobic interactions, driving the aggregation of hydrophobic chains, Additional stabilization is provided by hydrogen bonds, formed between polar head groups and surrounding water molecules. The shape of lipid aggregates in aqueous solution depends on the geometrical shapes of lipids. Lipids are assigned geometrical classes, based on the ratio of surface area of head groups and cross-sectional area of hydrocarbon chains [44]. If the ratio of head to tail is high, lipids are classified as cones. In water-like solutions, such lipids tend to form spherical micelles. Lipids with approximately the same sizes of heads and tails are cylindrical and form a bilayers in aqueous solution.

Lipids found in biomembranes have a cylindrical form [44]. When dissolved in water, they aggregate into a bilayer with a thickness of 4 – 5 nm (Fig. 2.3). Lipid tails

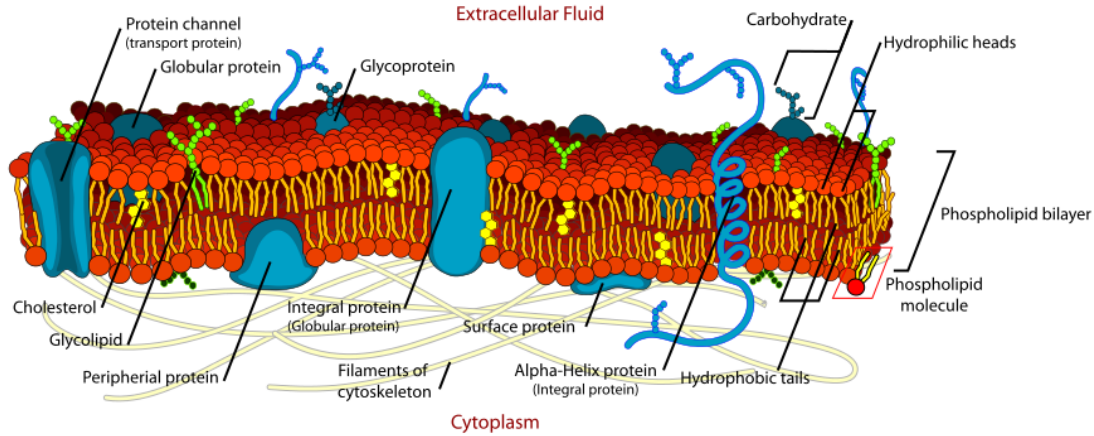


Figure 2.3: The cell membrane consists of a lipid bilayer with embedded proteins. Head groups of lipids are exposed to the aqueous solution, while tails are buried inside, forming the hydrophobic core of the bilayer. Beneath the plasma membrane is the cytoskeleton, a protein meshwork that supports cell structure and defines its shape. Source: wikipedia:cell membrane detailed diagram. This picture is available under the Creative Commons License.

are buried inside the bilayer. They assume directions perpendicular to the surface of bilayer, and form a so-called hydrophobic core. The hydrophobic core acts as a barrier against the diffusion of hydrophilic molecules across the membrane. Hydrophilic head groups are exposed to the water.

Proteins are another major component of membranes. Their concentrations vary from 20% to 80%, depending on the membrane type. Proteins either span the membrane (transmembrane proteins), anchor the membrane by bonding covalently with the lipid (lipid-anchored proteins), or form associations with the membrane through interactions with the lipid head groups or transmembrane proteins (peripheral proteins) as seen in Figure 2.3. While lipids provide the membrane with its sheet-like structure, proteins are responsible for the functionality of membranes, including transport through the membrane or cell-cell communication [44].

In a pure phospholipid bilayer, lipids can rotate around their long axes and diffuse in lateral directions with a  $10^{-8}$  cm<sup>2</sup>/sec diffusion rate [2]; hence lipid bilayers behave like a two-dimensional fluid. Similar diffusions in the lateral direction, but with smaller rates, are observed for lipids and embedded proteins in biomembranes [44]. Based on this observation, Singer *et al.* [46] proposed a fluid mosaic model for biomembranes, where the membrane is presented as a fluid-like phospholipid bilayer with diffusing proteins embedded in it. The fluid mosaic model predicts unrestricted diffusion and

a random distribution of membrane components. However, recent data show that the membranes have a dynamic, yet compartmentalized structure [47, 48], and the fluid mosaic model should be refined. Veréb *et al.* [49] proposed a modified version of the fluid mosaic model. In this model, known as the dynamically structured mosaic model, non-randomly distributed components of the membrane form mosaic-like clusters, and fluidity is interpreted as a continuous dynamic restructuring of clusters.

### 2.1.3 Cytoskeleton

Throughout its lifetime, the cell and its components are in constant motion. The development of the organism is accompanied by collective cell migrations; migrations of leukocytes participate in the immune response [40]. Small vesicles and even organelles, such as mitochondria, are transported from one part of the cell to the other. During cell division, duplicated chromosomes separate and move to the opposite poles of the cell [50]. All these motions are regulated by the cytoskeleton, a protein network that extends throughout the whole cell. The cytoskeleton not only governs cellular motions, but also supports cell structure and defines its shape.

It was initially thought that only eukaryotic cells have a cytoskeleton, but recent studies have found cytoskeletal structures in prokaryotic cells as well [51].

The eukaryotic cytoskeleton consists of three types of protein filaments: microfilaments, intermediate filaments and microtubules [2].

1. *Microfilaments or actin filaments:* Actin filaments support the cell membrane, define cell shape and participate in cellular movements. The monomer of microfilaments is a globular protein, actin, which under physiological conditions, polymerizes into a linear chain called the actin filament. The actin filament has a diameter of 7 nm. Its contour length can achieve up to 30 – 100  $\mu\text{m}$  *in vitro* and several micrometers *in vivo* [52]. They are relatively stiff and have a persistence length  $l_p$  ranging from 3 – 17  $\mu\text{m}$ , which is comparable to their length *in vivo*. Thus, actin filaments are semiflexible polymers [53].

Actin filaments can further link into more complex structures stabilized by actin cross-linking proteins. There are two types of structures that actin filaments can form, namely bundles and networks [2]. Bundles (Fig. 2.4 (*Left*)) are formed when actin filaments tightly pack parallel to each other. In particular, actin filaments along with myosin filaments may form contractile bundles, which participate in cell division (actomyosin contractile ring), cell adhesion and locomotion (stress fibres) [54]. Actin fila-

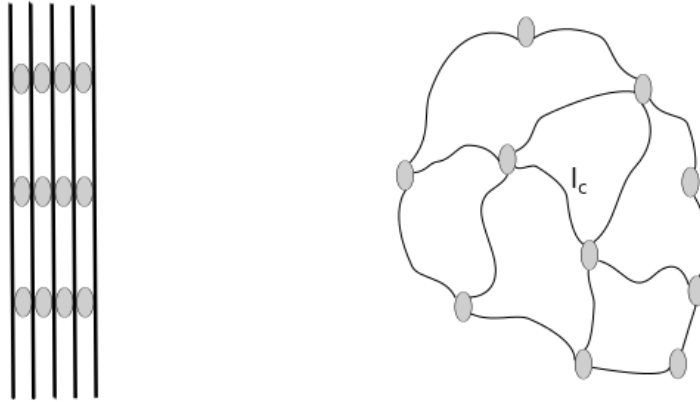


Figure 2.4: Structures formed by actin filaments. (*Left*) Tightly packed actin filaments (black lines) form bundles. (*Right*) Orthogonally cross-linked actin filaments (black lines) form loose semiflexible networks with an average distance  $l_c$  between the cross-linking proteins (gray circles).

ments also form networks (Fig. 2.4 (*Right*)), where they are cross-linked orthogonally, forming isotropic meshworks [53]. A variety of actin binding proteins may participate in the formation of the network, so the mean distance between cross-links can be as small as  $0.1 \mu\text{m}$  [55]. Actin filament networks display properties of viscoelastic materials under physiological conditions [56, 57]. An example of an actin network is a layer beneath the plasma membrane known as the cell cortex (the network of filaments in Fig. 2.3). The cell cortex is a relatively thin (100 nm) dynamic layer coupled to the plasma membrane through a variety of linker proteins, in particular, the motor protein myosins. Myosins are capable to exert contractile forces on actin filaments leading to the contraction of the cortex. This attachment of the plasma membrane to the actin cytoskeleton, known as membrane-to-cortex attachment (MCA), provides mechanical support to the membrane and plays an important role in processes involving cell shape changes [58].

2. *Intermediate Filaments*: Intermediate filaments exist in almost all animal cells, but they are absent in plant and fungi cells [2]. In the absence of cell walls in animal cells, these filaments are responsible for the mechanical strength of the cell [59]. Unlike other filaments, various proteins can serve as subunits during intermediate filament assembly [59]. At the initial stage of filament formation, subunit proteins form dimers. Dimers can be both homopolymeric and heteropolymeric. After dimers are

formed, they associate into tetramers, which, in turn, associate into long protofilament chains. The next stage includes lateral association of protofilaments into loose rope-like protofibril. At the final stage the protofibril undergoes compaction and forms 10 nm thick intermediate filaments. Intermediate filaments are an order of magnitude more flexible than actin filaments, with a persistence length ranging from 200 nm to 1  $\mu\text{m}$  [53].

Like actin filaments, intermediate filaments can form bundles or networks with the help of intermediate filament-associated proteins. These proteins also link intermediate filament structures to microfilaments, microtubules, plasma and nuclear membranes. Similar to actin filament networks, networks of intermediate filaments exhibit viscoelastic properties [60].

3. *Microtubules*: Microtubules are polymerized from tubulins. Tubulin is a heterodimer that binds to other tubulins, forming 5 nm thick linear chains of protofilaments. 13 protofilaments are then arranged side by side and form a hollow tube, the microtubule, with a thickness of 25 nm and a length up to 100  $\mu\text{m}$  [56].

There is a continuous association and dissociation of tubulins in existing microtubules, which makes them dynamic structures [61]. If the association rate is higher than the dissociation rate, the microtubule grows, otherwise it shortens. In cells, rates of association and dissociation are controlled by microtubule-associated proteins, which can stabilize or destabilize microtubules. This dynamic nature of microtubules plays an important role in cells, where, for example, during cell divisions 100  $\mu\text{m}$  long microtubules should depolymerize and reorganize themselves in just several minutes [42]. In contrast to microfilaments and intermediate filaments, microtubules do not form bundles or networks. They behave like viscoelastic materials, but are much stiffer than microfilaments, with a persistence length  $> 1$  mm [62, 63, 53].

All eukaryotic cells have microtubule-organizing centers (MTOC) [2]. They serve as nucleation sites for microtubule growth. In animal cells organelles called centrosomes serve as MTOC. The centrosome is localized at the central part of the cell, close to the nucleus. One end of the microtubule is bound to the centrosome, and the other end is directed towards the cell periphery.

## 2.2 Cell Cycle

One of the most fundamental properties of cells is their ability to self-reproduce. All cells reproduce through divisions during which parental cells divide into two daughter

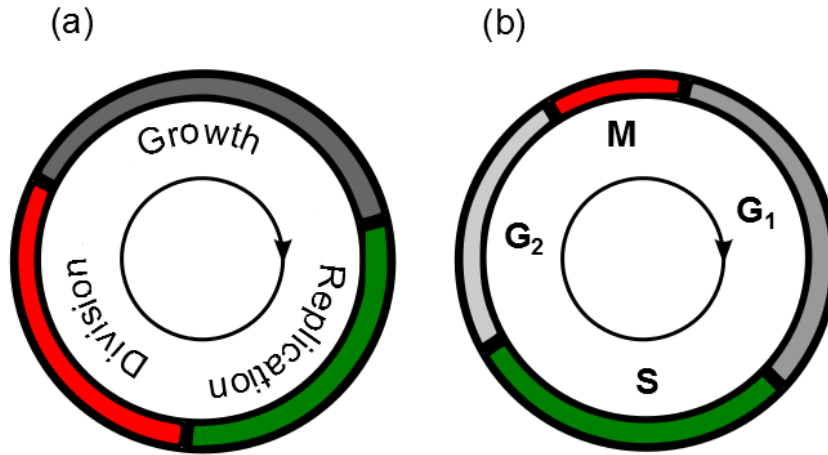


Figure 2.5: Cell cycle diagrams: (a) The cell cycle of a bacterium consists of three stages: growth (B), replication (C) and division (D) (b) The cell cycle of an eukaryotic cell consists of interphase (G<sub>1</sub>, S and G<sub>2</sub>) and mitosis (M) stages.

cells. Daughter cells further grow and divide themselves. By repeating this cycle over and over again, a single fertilized egg cell develops into a multicellular organism during embryonic development, and unicellular organisms, like bacteria, create colonies. Cell divisions also take place when damaged or dead cells are replaced with new ones. The cell division cycle consists of various stages, during which cells grow, their DNA replicates and segregates, and finally, they split into two cells [5, 2].

Prokaryotes have a relatively simple cell cycle [5]. A typical prokaryotic cell cycle consists of three stages: the period between the cell birth and the initiation of chromosome replication, known as stage *B*, the period required for chromosome replication, known as stage *C*, and the time between completion of chromosome replication and completion of division, known as stage *D* (see Fig. 2.5(a)). In the growth stage, the cell grows and prepares for chromosome replication, which takes place at the replication stage [5]. For prokaryotes, the replication of chromosomes always starts at the site called the “origin of replication” (*oriC*), and ends at the “terminus of replication” (*ter*). Prokaryotic chromosomes segregate along with replication. Right after replication of *oriC*, copies of chromosome push apart and move to the opposite poles of the cell. Unlike eukaryotes, prokaryotes do not have special machinery to separate replicated chromosomes, and the mechanisms of segregation are still unknown.

Initiation of the division stage usually occurs when the cell has doubled in mass. It is coordinated with completion of chromosome replication and segregation. At the initial stage of the cell division, protofilaments of the Filamenting Temperature-Sensitive Mutant Z (FtsZ) proteins assemble in the plasma membrane and form a ring-like structure, known as a Z-ring [5]. FtsZ proteins are homologs of eukaryotic tubulin [51]. Similar to tubulin, they polymerize into linear protofilaments in a head-to-toe manner, though do not form tube-like structures. For most bacteria, a Z-ring is assembled mid-cell [42]. Osawa *et al.* [64] have shown that the Z-ring is capable of producing membrane constriction by applying contractile forces on the membrane. Along with the FtsZ protein, other proteins are recruited to stabilize and anchor the Z-ring to the membrane, as well as control polymerization of FtsZ protofilaments. Together they form a bacterial division apparatus, a divisome. Bacterial cells are split by different mechanisms [42]. During division by constriction, the cell envelope layers contract, pinching the cell. By the end of the constriction, the cell envelope layers close, and the cell splits in two. The division mechanism by septation is accompanied by coordinated synthesis of the transverse cell wall (septum) at the site of Z-ring assembly and invagination of plasma membrane. Lastly, some bacteria, for instance *E. coli*, divide through coordinated constriction of membranes and septum formation [65].

The lengths of different division stages in bacteria depend on the rate of cell growth. For fast growth rates, the length of replication and division stages stay constant regardless of the cell doubling time. This may induce disappearance of the growth stage, when the cell doubling time is less than the time spent in replication and division stages combined [66]. In nutrient-poor environments, bacterial growth is slow, and one can observe distinct growth stages as well as prolonged times spent in chromosome replication and division [67].

The eukaryotic cell cycle is more complicated (Fig. 2.5 (b)). It consists of two major parts, interphase and mitosis. During interphase, the cell grows and its chromosomes replicate. Interphase is divided into three stages: *G1* (Gap 1), *S*, and *G2* (Gap 2). After division, the newborn cell enters the *G1* stage, where it grows and synthesises the necessary components for DNA replication. Once the cell is ready for replication, it enters the *S* stage. Each chromosome replicates, but both sister chromatids stay attached at the centromere, forming the famous 'X'-shaped chromosomes. Microtubule organizing organelles, the centrosomes, are also replicated at this stage. Once replication is over, the cell enters the *G2* stage, where it continues to grow and prepare for division.

Cell division takes place during mitosis (M stage in Fig. 2.5). At the initial stage of



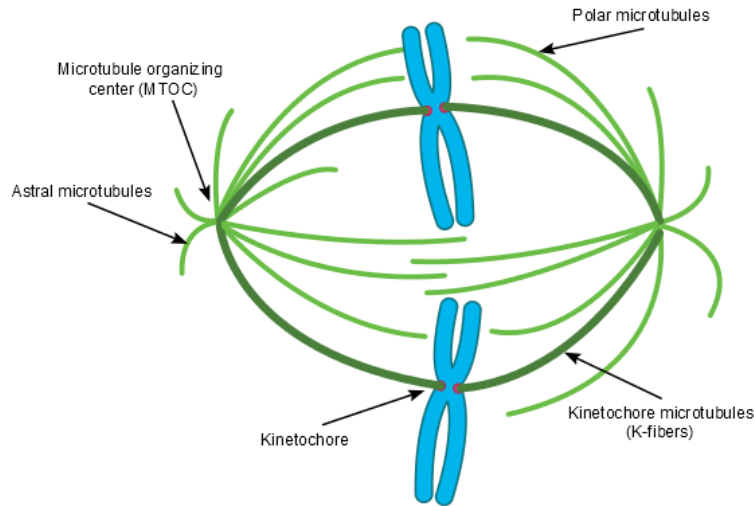


Figure 2.6: Mitotic spindle. Microtubules reorganize to form the mitotic spindle. Microtubules attach to chromosomes and pull them apart. Source: wikipedia:spindle apparatus. This picture is available under the Creative Commons License.

mitosis, chromosomes condense. In order to segregate chromosomes, eukaryotic cells assemble a mitotic spindle (Fig. 2.6).

In animal cells, the mitotic spindle starts to form when centrosomes separate and move to the opposite poles of the cell. Two centrosomes serve as poles of the spindle. At this stage microtubules undergo extensive reorganization: long microtubules which were extended throughout the whole cell in interphase, are now replaced by shorter ones. One end of the microtubules stays anchored to the centrosome, while the other end rapidly grows and shrinks, exploring its environment, until it finds a chromosome and attaches to it. Sister chromatids are attached to microtubules anchored to the opposite centrosomes, as shown in Figure 2.6. When the spindle formation is complete, microtubules apply forces on chromosomes, pulling and pushing them. Chromosomes move along the net force direction and align at the spindle equator, also known as the metaphase plate, which is perpendicular to the spindle. Once all chromosomes are aligned at the metaphase plate, chromatids are separated and pulled towards the spindle poles.

The final stage of division is cytokinesis, when the parent cell divides into two daughter cells. At the initial stage of cytokinesis, the contractile ring is formed beneath the plasma membrane, along the division plane (metaphase plate). It consists of actin filaments bundled together by the protein myosin. Interactions between actin and

myosin are capable of creating a contraction with the contractile force of  $10^3 - 10^5$  pN [4]. Contraction of the ring steadily decreases the opening between the two parts of the cell until it is completely sealed.

In plant cells, the existence of the rigid wall prevents division by contraction. Instead, plant cells build new cell walls along the division plane. In contrast to animal cells, the position of the new cell wall is not defined by the mitotic spindle in plant cells. It begins to form at the *G2* stage, during which cortical microtubules align in the ring-like structure beneath the plasma membrane, called the preprophase band. A set of microtubule and actin filaments extend from the band towards the nucleus, forming a wheel-like structure in the place of the future cell wall. After the chromosomes are separated, a cell plate is formed in the center of the cell, at the location of the preprophase band, by adding new plasma membrane and cell wall material. It continues to grow until it meets the parental cell walls.

As discussed above, the cell division plane is defined by the position of the mitotic spindle (or peripheral band in plant cells) to ensure proper distribution of chromosomes after division. Based on the position of the division plane, cells divide symmetrically, producing identical copies of themselves, or asymmetrically. The latter produces daughter cells with different sizes and fates. Symmetric division was first observed in the 19<sup>th</sup> century. Based on their observations of plant cells, Hofmeister and Errera defined simple geometrical rules by which cells divide symmetrically [68]. According to those rules, the choice of division plane depends on the geometrical shape of the cell. The new cell wall is built perpendicular to the parental cell walls. Moreover, the division plane is chosen such that it is oriented along the shortest path that divides cell volume in half. A similar division mechanism was observed in animal cells. Known as the “long axis rule” or Hertwig’s rule, it defines the division plane as the one which passes through the cell’s center of mass, perpendicular to its long axis [12]. To explain such precise positioning of the division plane, it was proposed that microtubules responsible for positioning mitotic spindle exert length-dependent forces on the spindle [69, 12]. Thus, long microtubules pull the spindle more strongly than short microtubules do, which drives the spindle towards the positions where forces from opposite poles of cell are balanced.

The aforementioned mechanism of symmetric positioning of mitotic spindle assumes that pulling forces are the same for microtubules of the same length, regardless of their position in the cell. Some cells may exhibit spatial differences in structure. Such cells, known as polarized cells, might have an asymmetric distribution of pulling

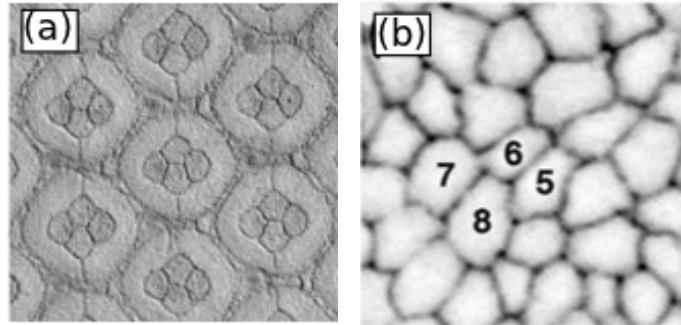


Figure 2.7: Cell packing topologies. (a) Hexagonally packed *Drosophila* ommatidium. Adapted by permission from Macmillan Publishers Ltd: Nature ([73]), copyright (2004). (b) Irregularly packed cells in *Drosophila* wing. Adapted by permission from Macmillan Publishers Ltd: Nature ([19]), copyright (2006).

forces [70]. As a result, the net force positions the spindle off the cell's center. Consequently, the division plane is formed off-center, such that it bisects the mitotic spindle at its current position and divides the cell asymmetrically. Recently, the spindle-independent mechanism of asymmetric division plane selection in *Drosophila* neuroblasts was observed as well [71]. Asymmetric cell division is an essential mechanism for creating different cell types during the development of multicellular organisms. During the asymmetric division, proteins are differentially segregated into daughter cells, defining their different fates [72].

### 2.3 Structure and Development of Epithelial Tissue

In multicellular organisms, cells with similar functionality are assembled into tissues. Several tissues are combined into organs, the functional units of organisms. Having precise shape, size and topology is essential for proper functioning of tissue. For example, hexagonal packing of *Drosophila* retina ommatidium aids the insect's vision (Fig. 2.7)

All tissues originate from single fertilized eggs during embryonic development. Mechanisms that govern formation of tissues starting from a single cell and drive them to their final size and shape are still not completely understood [18].

A commonly used model system for studies on tissue development is the epithelium. Epithelial tissue consists of epithelial cell layers, forming sheet-like structures [2]. In adult organisms, epithelial sheets line surfaces of organs and serve as protective surfaces (e.g., skin) or barriers with selective permeability (e.g., epithelium lining in-

testines). A simple epithelium consists of a single layer of epithelial cells. It is an attractive model system due to its simplicity. Multilayer epithelia are called stratified and have more complex structure [2].

One of the better characterized epithelial tissues is *Drosophila* fruit fly simple epithelium [74]. The plasma membrane of an epithelial cell is subdivided into structurally and functionally different apical and basolateral domains, meaning the cell is polarized. Neighboring cells align their domains throughout the tissue, therefore epithelium displays global polarization in the direction perpendicular to the epithelial plane [75]. In addition, epithelial cells have a secondary polarization in the plane of the epithelium, known as planar cell polarity [76]. This planar cell polarity is an important feature of cells that coordinates cellular events along the tissue [77, 78, 79].

Cells have the ability to adhere to substrates including other cells and the extracellular matrix with the help of special molecules, called cell adhesion molecules (CAMs) [2]. Adhesion is accompanied by remodelling of the cytoskeleton and the establishment of localized sites of adhesion [54]. Remodelling of the cytoskeleton involves the formation of actin assemblies capable of the generation of mechanical forces at the cell-material interface [54]. Epithelial cells in tissues are held together with the help of cell adhesion molecules of the cadherin family [80]. Cadherins are transmembrane proteins. Their cytoplasmic domain binds to the actin cytoskeleton, while extracellular domains interlock with cadherins emerging from the neighbor cell surface [79]. In epithelium, cadherins are the main adhesive molecules in adhesion junctions, which are believed to represent the stronger interaction regions between neighboring cells [80]. During tissue development, these junctions are constantly remodelled as a response to various cellular events such as cell divisions, rearrangements, migrations and death. Adhesive junctions are considered to be a two-dimensional network that defines cell packing geometries in tissue. Indeed, cells in a cross-section of a *Drosophila* wing resemble polygons defined by adhesive junctions (Fig. 2.7). This resemblance serves as a basis for several models, where each cell is assumed to be a polygon in junctional network, formed by adhesive junctions [28, 27].

Epithelial tissue growth is particularly well characterized in the *Drosophila* wing. Here we briefly discuss tissue growth based on growth of the *Drosophila* wing. Similar principles of growth, however, seem to be applicable to other systems as well [81].

The fruit fly *Drosophila* starts its developments from a single egg, which within 24 hours of being laid at 25 °C hatches into larva. After about 4 days of development, the larva becomes a pupa, after which it undergoes metamorphosis and turns into an adult

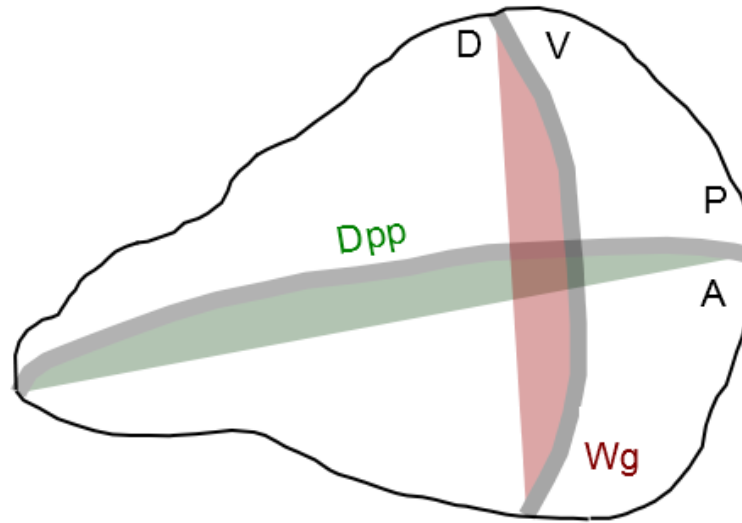


Figure 2.8: The *Drosophila* wings disc is divided into anterior (A)-posterior (P) and dorsal (D)-ventral (V) compartments. Two morphogens Dpp and Wg form morphogen gradients along anterior-posterior and dorsal-ventral axes of wing disc.

fly [82]. At the larval stage, *Drosophila* does not have wings, however structures that eventually turn into wings can be identified. These structures, known as wing imaginal discs, are epithelial sheets of about 30-40 cells [82]. During larval development, these patches of cells undergo rapid proliferation (cell divisions). The number of cells in wing discs increase up to 50,000 by the end of the fourth day of larval development. At the initial stage of development proliferation is faster, indicating faster growth of tissue. As time progresses, the proliferation rate decreases [18]. Cells in the proliferating wing disc have asynchronous yet homogeneous growth rates, with about 8.5 hours of average cell doubling time, regardless of their relative position in the disc. Mitotic cells compose, on average, 1.7% of all the cell population and can be found throughout the entire disc [24].

During development, the *Drosophila* wing disc is subdivided into anterior (A)-posterior (P) and dorsal (D)-ventral (V) compartments by two compartment boundaries (Fig. 2.8) [2]. Cells that belong to different compartments express different genes. *Drosophila* wing disc growth and patterning is controlled by morphogens. The morphogen Decapentaplegic (Dpp) is expressed in the central stripe of the disc, along the axis that divides the wing into anterior and posterior compartments (Fig. 2.8). Concentration gradually decreases towards the periphery [83]. Another morphogen, Wingless (Wg), is expressed along the dorsal-ventral axis of the wing, perpendicu-

lar to the anterior-posterior morphogen gradient [84, 85]. Several other proteins are linked to the growth and patterning in the wing as well [84]. It has been shown that the concentration gradient of Dpp induces and regulates wing growth [83]. How exactly morphogen gradients generate homogeneous growth is still unknown. Several models have been proposed to explain growth control by morphogen gradient, including mechanical feedback models [86, 87]. In the model proposed by Aegerter-Wilmsen *et al.* [87], it is assumed that growth is not only controlled by growth factor morphogens, but by mechanical forces as well. Two growth factors that are expressed along the perpendicular directions create a net growth factor that has highest activity at the center of the wing disc. Closer to the periphery, the activities of growth factors decrease. Such gradients of net growth factor may lead to homogeneous growth with the assumption that compression inhibits growth. Cells in the central part of the wing disc are subject to compression from proliferating cells in the periphery. They require a higher level of morphogen activity to initiate growth, whereas cells in the periphery are under less stress and can grow even at low levels of growth factors. Compression inside the disc increases along with the growth of the disc, and once the stimulatory effects of growth factors are inhibited by compression, growth is terminated. Experimentally observed distributions of stresses in wing discs support this model [88]. Compression is found to have a maximum in the central part of the disc and to grow along with the wing's growth. It is unclear, however, whether compression forces are big enough to halt growth [18].

## 2.4 Cell Packing in Proliferating Epithelia

Predominantly hexagonal packing of simple epithelial tissues was observed as early as the 1800s [89]. This packing was believed to reflect the tendency of cells to form optimal space-filling structures and minimize their surface energy [90]. However, while hexagonal cells prevail in non-proliferation tissues, the packing topology of proliferating epithelia is significantly different. In 1926, Lewis [91] studied cell packing topologies and geometries in proliferating cucumber epidermis and found that a large amount of non-hexagonal cells also exist in the proliferating epithelium with frequencies that are highly reproducible. The distribution of cell polygon types in proliferating epithelium has a peak at hexagonal cells and an asymmetric distribution of pentagons and heptagons. Four-sided as well as eight- and more sided cells were observed as well, but they are relatively rare (they compose less than 5% of total cells). Interestingly,

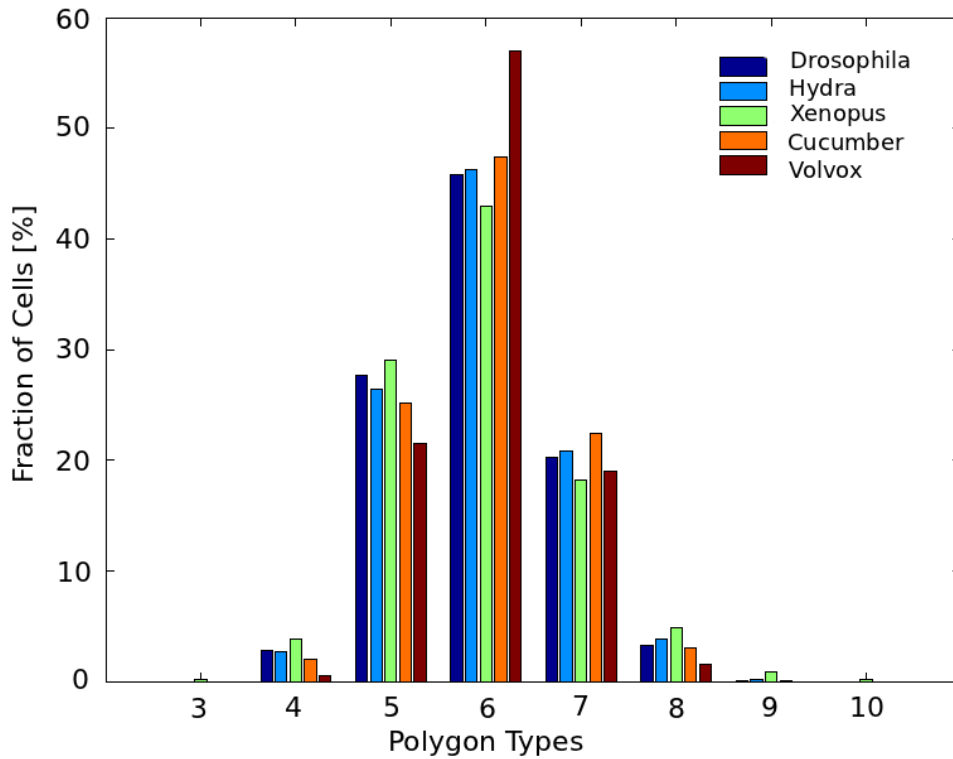


Figure 2.9: Distribution of cell polygon types in animal and plant proliferating epithelial tissues. Various species have similar characteristic distribution with peak at hexagons and asymmetric distribution of pentagons and heptagons. Data for *Drosophila*, *Hydra*, *Xenopus* is taken from Gibson *et al.* [19], data for *Cucumber* is taken from Lewis [92] and data for *Volvox* is taken from Korn *et al.* [93]

this topology is conserved among species [19]. Figure 2.9 displays the frequencies of cell polygon types for proliferating epithelia taken from various species of animal and plant kingdoms. As Figure 2.9 shows, for a majority of epithelial tissues, around 45% of cells have hexagonal shapes, and the frequencies of heptagons and pentagons are around 30% and 20% correspondingly.

Recently, Gibson *et al.* [19] showed that this “default” packing topology is a direct consequence of uniform proliferation in the absence of cell rearrangements. In the model suggested by Gibson and colleagues, each cell is presented as a polygon with  $s$  sides in a two-dimensional planar network. Since no three sided-cells were observed in epithelial proliferation,  $s \geq 4$ . The state of tissue at a given generation  $t$  is described by a vector  $\mathbf{p}^t = [p_4 p_5 p_6 \dots]$ , where  $p_i$  is the frequency of  $i$ -sided cells. The evolution of the system is described as a Markov process, so that  $\mathbf{p}^t = \mathbf{p}^{t+1} P S$ , where  $P_{ij}$  and

$S_{ij}$  define the probability of an  $i$ -sided cell to become  $j$ -sided at the next generation.

The matrix  $P_{ij}$  defines the probability of an  $i$ -sided parental cell to divide into a  $j$ -sided daughter cell. To calculate the probability, one needs to consider the way an  $i$ -sided cell distributes its vertices to two daughter cells. Since no three-sided cells were observed, each daughter cell has to receive at least 2 junctions from parental cells, leaving  $i - 4$  parental junctions to be distributed. A daughter cell that ends up with  $j$  sides after division receives a minimum of 4 junctions (minimum 2 from parent and 2 from the cleavage plane), thus the probability  $P_{ij}$  is equal to the number of ways an  $i - 4$ -sided cell can pass  $j - 4$  sides to one of the daughters. For a division line that is chosen uniformly at random, the probability is binomial, with  $n = i - 4$ ,  $k = j - 4$  and  $p = 1/2$ . The probability matrix is then given as

$$P_{ij} = \begin{pmatrix} 1 & & & & & & \\ 1/2 & 1/2 & & & & & \\ 1/4 & 1/2 & 1/4 & & & & \\ 1/8 & 3/8 & 3/8 & 1/8 & & & \\ 1/16 & 1/4 & 3/8 & 1/4 & 1/16 & & \\ & & \dots & & & & \end{pmatrix}. \quad (2.1)$$

The matrix  $S_{ij}$  defines the probability of an  $i$ -sided cell to become  $j$ -sided solely due to divisions on neighbor cells. The matrix can be derived from the following considerations. During mitosis a new side is added. This newly generated side adds a junction to each of its two neighbor cells. A round of divisions generates  $2N$  cells from  $N$  previously existing cells adding, on average,  $2N$  junctions. Hence, on average, the number of sides gained during one round of division is 1 per cell. The matrix  $S_{ij}$  now can be presented as

$$S_{ij} = \begin{pmatrix} 0 & 1 & & & \\ & 0 & 1 & & \\ & & 0 & 1 & \\ & & & \dots & \end{pmatrix}. \quad (2.2)$$

The transition matrix  $T = PS$  in the time evolution of the system is now defined, and the equilibrium state of the system can be calculated. It is found to be approximately 28.9% pentagons, 46.6% hexagons and 20.8% heptagons [19].

Although most of the tissues presented in Figure 2.9 exhibit packing topologies similar to the one obtained by Gibson *et al.*, there are exceptions. For example, the



number of hexagons in *Volvox* reaches up to 60%, which is a significant difference compared to other cases (Fig. 2.9). The model described above considers the case of uniform proliferation with no cell rearrangements. Mechanical properties of cells, which are known to affect cell shapes and packing topologies [73, 26] are not taken into account. The example of *Volvox* indicates that biological physical mechanisms may generate variations in proliferation and, consequently, in cell packing topologies [74].

## 2.5 Models For Tissue Growth and Morphology

The simplest models for studying cell packing topologies and geometries in tissues are the so-called topological models [74]. Topological models reconstruct a network of cellular connectivity. In growing tissue, this network might be altered by various cellular processes such as cell divisions, rearrangements and death. An example of a topological model for epithelial tissue is the one presented by Gibson *et al.* [19], where tissue is modelled as a two-dimensional planar network of epithelial junctions. Mathematically, such a network is described through faces, edges and vertices representing cells, their sides and junctions correspondingly. The model proposed by Gibson *et al.* incorporates one of the basic cellular processes, proliferation, as a Markov chain of system state transitions through adding randomly distributed junctions to an already existing network (see Sect. 2.4 for a detailed description of the model). The extension of this model, known as the cleavage plane regulation model [94], allows variations in the orientation of the division plane. Topological models have been used to study the effects of proliferation and the division plane orientation on tissue topology. These models, however, have their limitations. In particular, they do not account for cell mechanics, which may alter cell geometries and cell packing topologies [95].

Physical properties of cells and inter-cellular interactions are incorporated in several models [25, 26, 27, 28, 29, 30, 31, 32]. We discuss a few of them in detail below. Extensive reviews can be found in Refs. [74, 96].

In the model proposed by Farhadifar *et al.* [27], epithelium-like tissue is characterized by a network of cell adhesive junctions. Cells are presented as polygons with sides (cell edges) as straight lines connecting vertices (Fig. 2.10). This choice of model is inspired by the fact that cell shapes in a cross-section of epithelial tissue resemble polygons, and that cells have little or no rearrangements during tissue growth. To account for cell mechanics, the network at the given configuration  $\{\mathbf{R}_i\}$  is assigned an energy

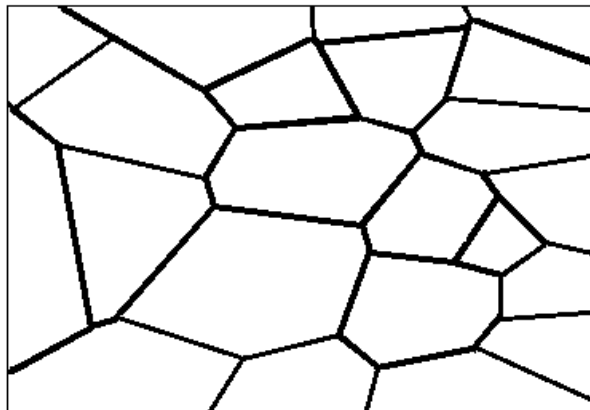


Figure 2.10: In vertex models (see eg. [27, 28, 33]), each cell is presented as a polygon inside the junctional network. Proliferation introduces new edges and vertices, thus cell packings remodel throughout development.

functional of the form

$$E(\mathbf{R}_i) = \sum_{\alpha} \frac{K_{\alpha}}{2} (A_{\alpha} - A_{\alpha}^{(0)})^2 + \sum_{ij} \Lambda_{ij} l_{ij} + \sum_{\alpha} \frac{\Gamma_{\alpha}}{2} L_{\alpha}^2. \quad (2.3)$$

The first term describes cell area elasticity.  $K_{\alpha}$  is the elastic coefficient and  $A_{\alpha}^{(0)}$  is cell's preferred area. The second term accounts for cell-cell interaction. Here  $\Lambda_{ij}$  is the line tension between  $i$  and  $j$  vertices and  $l_{ij}$  is the length of corresponding edge (cell boundary). It reflects both cell-cell adhesion and the contractile nature of cell's cortex. Finally, the third term represents contractility of the cell perimeter  $L_{\alpha}$  with the coefficient  $\Gamma_{\alpha}$ . Stable configurations of epithelial tissues correspond to minima of an energy functional. Vertex-like models were used to explore the impact of cell mechanics, rearrangements and growth rate on proliferating epithelium topology [28, 27, 33, 34]. They do not account for cell migration.

Collective cell migration is common in various biological processes [40, 9] and is an essential part of embryonic morphogenesis [97, 98]. Directed cell migration involves coordinated cycles of protrusion, contraction and adhesion regulated by the actomyosin cortex [14, 99]. As in the case of cell division, migration also depends on the mechanics of the cell [100] and, in fact, cell motility can be achieved by cortical contraction alone [101, 102]. Moreover, comparison between cell morphogenesis and the associated mechanical properties for cell division and migrations suggests common

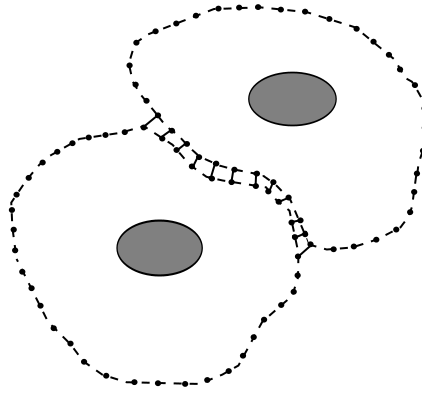


Figure 2.11: In the viscoelastic cell model proposed by Rejniak *et al.* [32], the cell is treated as an elastic membrane surrounding cytoplasm and a nucleus. Elastic boundaries consist of adjacent springs. Adhesive interactions between neighbor cells are modelled through attractive-repulsive forces.

regulatory mechanisms that govern cortex remodelling in both cases [15].

A more realistic way to model cell shapes and their mechanical properties requires an individual treatment of cells. Individually modelled cells do not carry pre-existing shape and topology and respond to mechanical forces in more natural ways. In the model suggested by Rejniak *et al.* [32], each cell is modelled as an elastic membrane that surrounds a viscoelastic cytoplasm and a point nucleus. (Fig. 2.11). Membranes form a closed elastic boundary immersed in an incompressible viscous fluid [103]. Time evolution of the system is defined by fluid motion with the boundary that moves along with the fluid. Mathematically, the boundary is modelled as a collection of points  $\mathbf{X}_i(l, t)$ , where  $l$  is the position of points along the boundary of  $i$ -th cell. To reflect the elastic properties of the membrane, boundary points  $X_i$  are connected through adjacent linear springs. Adhesive interactions between two neighbor cells in the tissue are mimicked through adhesive-repulsive springs, connecting boundary points of different cells. In addition to cellular forces along the boundary, sinks and sources are embedded into fluid. They are used to model cellular processes. An example is the process of cell growth. Cell growth is initiated by coupled source-sink pairs. Sources are located inside the cells and sinks are placed at the boundary. Such a distribution of sources and sinks creates fluid flow that pushes the boundary outwards and increases cell area. Thus, with the help of external cellular forces and the distribution of sources and sinks, one can extend the model to account for various cellular events. The growth of trophoblast bilayers, tumor development and the development of epithelial acini were among the

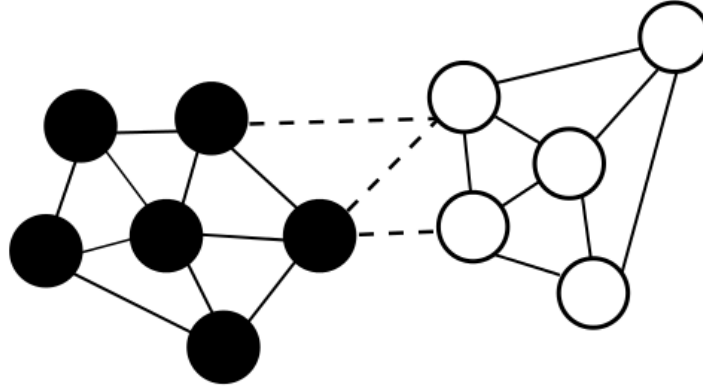


Figure 2.12: The model of Newman [31] treats each cell as a cloud of mass points. Here, black and white circles belong to two separate cells. Strong intra-cellular interaction potentials (solid lines) hold mass points of same cell together, while weak inter-cellular interaction potentials (dashed lines) model cell-cell adhesion in tissue.

applications of the model [32, 35, 36].

Another sub-cellular element model is the model developed by Newman [31]. In this model each cell is considered as a cloud of mass points (Fig. 2.12). Strong intra-cellular potentials bind mass points of the same cell to each other. Additional weak inter-cellular potentials are used to model cell-cell adhesion in tissue. Generalized Morse potentials are good candidates for both intra- and inter-cellular interactions. When the distance between two interacting particles is  $r$  they have the form:  $V(r) = V_0 \exp(-r^2/\zeta_1^2) - U_0 \exp(-r^2/\zeta_2^2)$  where parameters  $V_0$ ,  $U_0$ ,  $\zeta_1$  and  $\zeta_2$  are chosen such that the adhesion defined by the intra-cellular potential is stronger than the one defined by inter-cellular potential. Such a system evolves according to the overdamped Langevin equations

$$\dot{\mathbf{r}}_{\alpha_i} = \sum_{\alpha_i \neq \beta_i} F_{intra}(\alpha_i, \beta_j) + \sum_{\alpha_i} \sum_{\beta_j} F_{inter}(\alpha_i, \beta_j) + \eta_{\alpha_i}, \quad (2.4)$$

where  $\alpha_i$  is the  $\alpha$ -th mass point of  $i$ -th cell,  $\beta_j$  is the  $\beta$ -th mass point of  $j$ -th cell,  $F_{inter}$  and  $F_{intra}$  represent inter- and intracellular interaction forces correspondingly, and  $\eta_{\alpha_i}$  is the noise term which has a Gaussian distribution with zero mean and correlator

$$\langle \eta_{\alpha_i}^m(t) \eta_{\beta_j}^n(t') \rangle = 2D \delta_{i,j} \delta_{\alpha_i, \beta_j} \delta^{mn} \delta(t - t'). \quad (2.5)$$

Here  $D$  is the diffusion coefficient and  $\delta$  is the Dirac delta function. This model was used to simulate cell growth and division in two- and three-dimensional systems in order to study the dynamics of multicellular systems [37, 38, 39].

# Chapter 3

## Physical and Numerical Background

### 3.1 Physical Background

Cell shapes and packing topologies are tightly controlled by the mechanics of the cell cortex. The mechanical properties of the cell cortex influence processes that require changes of cell shape, such as divisions or migrations. Indeed, Stewart *et al.* [11] showed that the rounding of a mitotic cell is determined by the interplay between the hydrostatic pressure inside the cell and its cortex's contractility. Another example is the contractile ring, which assembles at the cortex along the perimeter of the cell's division plane. The mechanical forces created by the contractile ring pinch the cell and ultimately lead to the division of the cell. Cell packing topologies are also influenced by its cortex. For example, Käfer *et al.* [26] showed that cortex contractility has a contribution to observed cell packing topologies in *Drosophila* retina ommatidium. It balances cell-cell adhesion and is necessary to achieve correct packing topologies and geometries of cells in the retina. As we discussed in Chapter 2, the cell cortex is formed by elastic actin filaments that are cross-linked into network-like structures. The cell cortex itself behaves as an elastic material [11, 104].

When considering the motion of a cell and its sub-cellular components, one needs to take into account the cellular environment. The intracellular space is filled with the cytoplasm, which displays properties of an incompressible viscous fluid [104].

In this section we give a brief background on elastic materials and viscous fluids (Sect. 3.1.1 and Sect. 3.1.2). A more detailed background on these topics can be found in references [105, 106, 107, 108]. Inter-cellular interactions are discussed in Section 3.1.3.

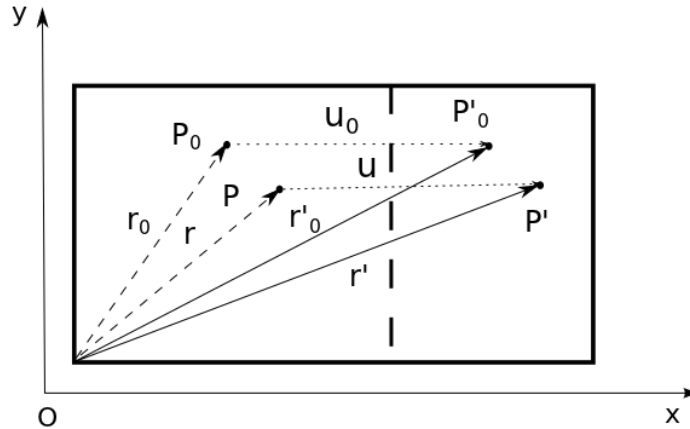


Figure 3.1: During deformation, two body points  $P_0$  and  $P$  with the radius-vectors  $\mathbf{r}_0$  and  $\mathbf{r}$  are displaced to new positions  $P'_0$  and  $P'$  with radius-vectors  $\mathbf{r}'_0$  and  $\mathbf{r}'$ . The displacement vectors  $\mathbf{u}_0$  and  $\mathbf{u}$  are defined as the difference of the radius-vectors before and after deformation.

### 3.1.1 Elasticity

Let us consider points  $P_0$  and  $P$  in the body, with radius-vectors  $\mathbf{r}_0$  and  $\mathbf{r}$  correspondingly (Fig. 3.1). During deformation of the body, points are displaced to new positions  $P'_0$  and  $P'$  with radius-vectors  $\mathbf{r}'_0$  and  $\mathbf{r}'$ . Displacement vectors are defined as  $\mathbf{u}_0 = \mathbf{r}'_0 - \mathbf{r}_0$  and  $\mathbf{u} = \mathbf{r}' - \mathbf{r}$ . For a small deformation and infinitesimally close points  $P_0$  and  $P$ ,

$$d\mathbf{r}' = d\mathbf{r} + d\mathbf{u} \approx d\mathbf{r} + \frac{\partial \mathbf{u}}{\partial \mathbf{r}} d\mathbf{r}. \quad (3.1)$$

The tensor  $\frac{\partial \mathbf{u}}{\partial \mathbf{r}}$  is called the displacement gradient tensor.

For small deformations, the distance between two points changes according to

$$|d\mathbf{r}'|^2 = |d\mathbf{r}|^2 + 2 \sum_{ij} \epsilon_{ij} dr_i dr_j, \quad (3.2)$$

where  $\epsilon_{ij} = \frac{1}{2}(\frac{\partial u_i}{\partial r_j} + \frac{\partial u_j}{\partial r_i})$  is the symmetric strain tensor.

In the two-dimensional case, the strain tensor has the form

$$\epsilon_{ij} = \begin{pmatrix} \epsilon_x & \epsilon_{xy} \\ \epsilon_{yx} & \epsilon_y \end{pmatrix}.$$

$\epsilon_x$  and  $\epsilon_y$  are known as the normal strains, and  $\epsilon_{xy}$  and  $\epsilon_{yx}$  are called shear strains. Geometrical interpretations of the normal and shear strains for the two-dimensional

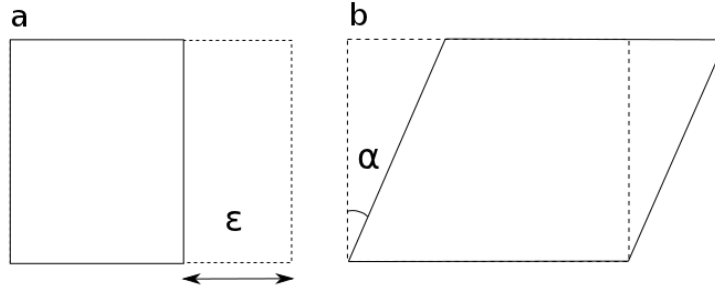


Figure 3.2: Two-dimensional normal and shear strains. (a) The normal strain in the direction  $n$  is characterized by the extension  $\epsilon$  of the body in that direction. (b) The shear strain is defined as the change in the angle  $\alpha$  between two initially orthogonal lines.

case are shown in Figure 3.2.

When a body is subjected to an external force, it deforms, which gives rise to internal forces. For a given surface with an area  $A$ , the ratio of the internal force to area,  $\mathbf{T}(\mathbf{r}, \mathbf{n}) = \mathbf{F}/A$ , is called the stress. Stress depends not only on the applied force and surface area, but also on the orientation of the surface. If  $\mathbf{n}$  is a vector normal to the surface area, then stress is related to  $\mathbf{n}$  as

$$\mathbf{T} = \sigma \mathbf{n}, \quad (3.3)$$

where  $\sigma$  is the stress tensor [105].

The two-dimensional stress tensor has the form

$$\sigma = \begin{pmatrix} \sigma_x & \sigma_{xy} \\ \sigma_{yx} & \sigma_y \end{pmatrix}.$$

The diagonal elements of the stress tensor are called normal stresses. Normal stress is directed along the normal vector of the surface. Off-diagonal elements of the stress tensor are called shear stresses and lie in the plane perpendicular to the surface normal.

Materials are characterized by their stress-strain relations. In this work, we deal with elastic materials. They resist applied external forces by finite strains and restore their original state after forces are removed. Under low stresses most elastic materials have a linear stress-strain relation, which is given by

$$\sigma_{ij} = \sum_{kl} C_{ijkl} \epsilon_{kl}. \quad (3.4)$$

The coefficients  $C_{ijkl}$  are called elastic moduli. For homogeneous isotropic materials,



the elastic moduli satisfy

$$C_{ijkl} = \alpha \delta_{ij} \delta_{kl} + \beta \delta_{ik} \delta_{jl} + \gamma \delta_{il} \delta_{jk}, \quad (3.5)$$

where  $\alpha$ ,  $\beta$  and  $\gamma$  are constants, and  $\delta_{ij}$  is the Dirac delta function [109]. Equation 3.5 along with Equation 3.4 gives

$$\sigma_{ij} = \lambda \delta_{ij} \sum_k \epsilon_k + 2\mu \epsilon_{ij}. \quad (3.6)$$

The constant  $\lambda$  is *Lamé's coefficient*, and  $\mu$  is called the shear modulus or modulus of rigidity. Relation 3.6 is the generalized *Hooke's law*. Hence, the behaviour of a homogeneous isotropic elastic material is characterized by two independent elastic constants.

Alternatively, strain can be expressed through stress from 3.4 as

$$\epsilon_{ij} = \frac{1}{2\mu} \left( \sigma_{ij} - \frac{\lambda}{3\lambda + 2\mu} \delta_{ij} \sum_k \sigma_k \right). \quad (3.7)$$

or, equivalently

$$\epsilon_{ij} = \frac{1 + \nu}{Y} \left( \sigma_{ij} - \frac{\nu}{Y} \delta_{ij} \sum_k \sigma_k \right). \quad (3.8)$$

Here,  $Y = \mu \frac{3\lambda + 2\mu}{\lambda + \mu}$  is called the modulus of elasticity or Young's modulus and  $\nu = \frac{\lambda}{2(\mu + \lambda)}$  is called Poisson's ratio.

To understand the physical meaning of the elastic moduli, one can look at stress-strain relations for simple cases. Suppose tension is applied to a two-dimensional body along the  $x$  direction. Then the stress tensor can be written as

$$\sigma = \begin{pmatrix} \sigma & 0 \\ 0 & 0 \end{pmatrix}$$

and the corresponding strain tensor will be

$$\epsilon = \begin{pmatrix} \frac{\sigma}{Y} & 0 \\ 0 & -\frac{\nu}{Y} \sigma \end{pmatrix}.$$

Therefore, Young's modulus characterizes the ratio of stress along the axes to the strain along the same axes. For the one-dimensional case, Equation 3.8 is reduced to Hooke's law for springs  $\epsilon_x = \frac{1}{Y} \sigma_x$ , and Young's modulus coincides with the spring constant. This example also shows that tension, along with the stretching of the material

in the applied direction, also results in the compression of the material in the transverse direction. Poisson's ratio defines the ratio of transverse strain to axial strain.

Next, suppose a two-dimensional body is subjected to a shearing stress with stress tensor

$$\sigma = \begin{pmatrix} 0 & \tau \\ \tau & 0 \end{pmatrix}.$$

Then, from Equation 3.6,

$$\epsilon = \begin{pmatrix} 0 & \frac{\tau}{2\mu} \\ \frac{\tau}{2\mu} & 0 \end{pmatrix}.$$

The shear modulus shows the ratio of the shear stress to shear strain.

Finally, consider a two-dimensional body subjected to an external pressure  $p$ , resulting in hydrostatic compression. The stress tensor has the form

$$\sigma = \begin{pmatrix} -p & 0 \\ 0 & -p \end{pmatrix}$$

with the corresponding strain tensor

$$\epsilon = \begin{pmatrix} -\frac{1-2\nu}{Y}p & 0 \\ 0 & -\frac{1-2\nu}{Y}p \end{pmatrix}.$$

Compression results in a volume change  $\Delta V = Tr(\epsilon) = -2(1 - 2\nu)p/E$  [105], so the relation between the applied pressure and the volume change can be written as  $p = -k\Delta V$ , where  $k = \frac{Y}{2(1-2\nu)}$  is called the bulk modulus of elasticity.

### 3.1.2 Viscosity

Based on the response to stress, materials are categorized as solids or fluids. If shear stresses are induced in a solid material, it undergoes a finite shear deformation. On the contrary, under a shear stress, fluids display continuous shear deformation, or flow. Examples of fluids are liquids and gases. In this work we consider incompressible liquids, meaning that the density of the fluid stays constant.

Suppose a fluid is placed between two plates (Fig.3.3). The bottom plate is kept motionless, and the top plate is pulled with a low velocity  $v$ . The resulting motion can be described as a flow of adjacent fluid layers, with the velocity gradient shown in Figure 3.3 [107]. Each layer moves along the neighboring layer with non-zero relative

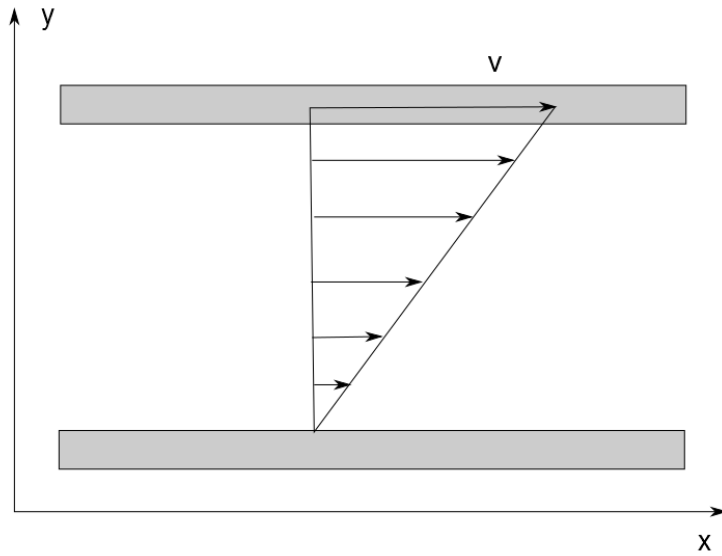


Figure 3.3: Velocity gradient in a fluid under shear flow. The bottom plate (shown in gray) is kept motionless and the top plate is pulled with the velocity  $v$ . The fluid between the plates moves with the velocity gradient (shown as arrows).

velocity, and experiences internal friction forces resisting the flow. The amount of the resistance depends on the type of fluid, and is called viscosity.

Let the displacement of the layer at height  $y$  during the flow be  $x(y, t)$ . Then the shear strain in the fluid is defined as

$$\gamma(y, t) = \frac{\partial x}{\partial y} \quad (3.9)$$

and shear strain rate is defined as

$$\dot{\gamma}(y, t) = \frac{\partial v}{\partial y}, \quad (3.10)$$

In the general case, for incompressible fluids [107]

$$\dot{\gamma}_{ik} = \frac{\partial v_i}{\partial x_k} + \frac{\partial v_k}{\partial x_i}. \quad (3.11)$$

Shear stress due to internal friction forces depends on the shear strain rate. For Newtonian fluids, the relation is linear

$$\tau = \mu \frac{\partial v}{\partial y}. \quad (3.12)$$

In a general case, for Newtonian fluids,

$$\tau_{ik} = \mu \left( \frac{\partial v_i}{\partial x_k} + \frac{\partial v_k}{\partial x_i} \right) \quad (3.13)$$

where  $\mu$  is the dynamic viscosity. For the fluids with the density  $\rho$ , the kinematic viscosity is defined as

$$\nu = \frac{\mu}{\rho}. \quad (3.14)$$

Consider a solid body moving with velocity  $v$  in a viscous fluid. While moving, the body experiences a drag force which opposes the motion and depends on the velocity of the body, as well as on the properties of the fluid. For such motion, one can define a dimensionless quantity called the *Reynold's number*

$$R = \frac{v\lambda}{\nu}, \quad (3.15)$$

where  $v$  and  $\lambda$  are the speed and length of the body, and  $\nu$  is the kinematic viscosity of fluid. The Reynold's number shows an interplay between inertia and viscous forces. Depending on the Reynold's number, the drag force has different dependence on the velocity of the body. Small  $R$  (low velocities) shows that viscosity dominates, and the drag force is defined by *Stoke's law*

$$\mathbf{F}^{drag} = -b\mathbf{v}, \quad (3.16)$$

where  $b$  is a constant, which depends on fluid viscosity and the geometry of the body. For high  $R$  (high velocities), inertia dominates, and the drag force is proportional to the square of velocity

$$\mathbf{F}^{drag} = -c\mathbf{v}^2, \quad (3.17)$$

where  $c$  is a constant depending on fluid density and the geometry of the body. Typically, Reynold's number is small for the cellular environment, thus the drag force is defined by Stoke's law.

### 3.1.3 Inter-membrane adhesion

The adhesive interactions between two cells in contact are mediated by their plasma membranes. Interaction forces between biomembranes are non-trivial due to the complex structure of the latter. Lipid composition of the plasma membrane, types of em-

bedded proteins, the extracellular matrix and the aqueous solution surrounding cells, all have their contributions. At large separations, inter-membrane forces include van der Waals attractive forces and, if membranes consist of lipids with charged head groups, electrostatic forces. At shorter distances, steric effects of extracellular matrices and thermal undulations of membranes lead to a repulsive interaction between two cells. In addition to non-specific interactions mentioned above, two membranes in contact may adhere with the help of specific, protein mediated interactions. Here, we briefly review just a few of all possible membrane-membrane interactions relevant to our work. Extensive reviews can be found in references [110, 111].

*1. Van der Waals interactions.* Attractive van der Waals (VDW) interactions are non-specific interactions that exist between all atoms and molecules. These forces have a quantum mechanical origin and arise from the interactions between permanent dipole moments of atoms, permanent induced dipole moments and two induced dipole moments defined by the instantaneous positions of electrons in atoms. The aforementioned interactions are attractive with a potential energy proportional to  $1/r_{ij}^6$  [111], where  $r_{ij}$  is the distance between  $i$  and  $j$  interacting atoms. The complete potential that describes the interaction between two atoms should include the Pauli exclusion principle at short distances, hence a short-range repulsive force should be added to the attractive VDW potential. Typically, a positive term proportional to  $1/r_{ij}^{12}$  is added to complete the VDW interaction potential. The potential (see Fig. 3.4), known as the Lennard-Jones potential (LJ), describes the VDW interactions between two atoms  $i$  and  $j$  and has the form

$$V_{LJ}(r_{ij}) = 4\epsilon \left[ \left( \frac{\sigma}{r_{ij}} \right)^{12} - \left( \frac{\sigma}{r_{ij}} \right)^6 \right]. \quad (3.18)$$

Here,  $\epsilon$  is the depth of the potential well and  $\sigma$  is the the diameter of the interacting particles. The VDW forces between two macroscopic bodies of various geometries are derived from atomistic interactions based on the Lifshitz theory [112]. Geometrically, two membranes separated by distance smaller than their thickness  $d$  can be thought of as two slabs. If the distance between the slabs is  $D_s$  [110], then the VDW potential energy per unit area is

$$V_{VDW}(D_s) = -\frac{A}{12\pi D_s^2}. \quad (3.19)$$

The constant  $A$  is called the Hamaker constant which depends on the properties of the interacting substances as well as the surrounding medium. Two lipid bilayers interacting in liquid medium, such as water, have a Hamaker constant of  $A \sim 10^{-20}$  J [111].

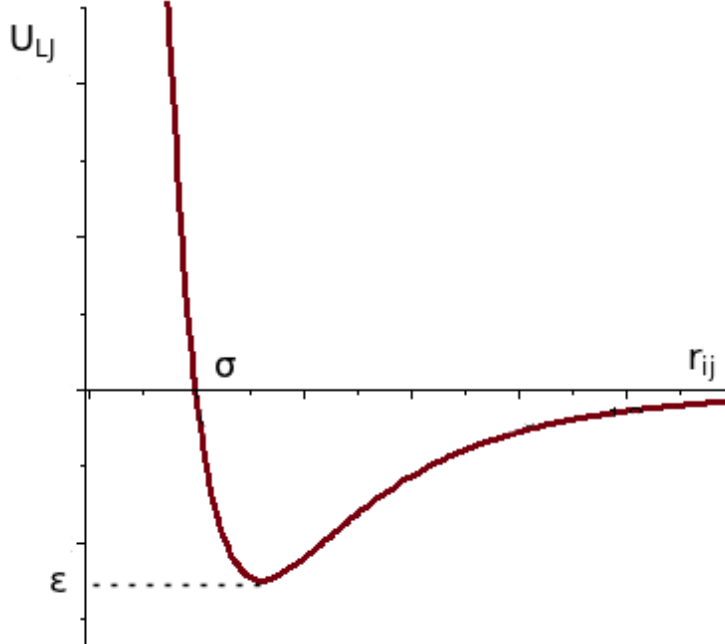


Figure 3.4: The dependence of the Lennard-Jones potential  $V_{L,J}$  on the distance  $r_{ij}$  between interacting particles  $i$  and  $j$ .  $\epsilon$  is the depth of potential well and  $\sigma$  is the diameter of interacting particles.

Equation 3.19 holds only if the thicknesses of the slabs exceed the distance between them. When  $D_s$  is larger than  $d$ , i.e., for the case of interacting thin sheets, the potential energy density decreases much faster, proportional to  $\sim 1/D_s^4$  [113].

The Lifshitz theory considers interacting objects to be macroscopic. Strictly speaking, the formulas for VDW interactions and the Hamaker constants, calculated with the help of the Lifshitz theory, should be used only for macroscopic bodies at separations exceeding molecular dimensions. Still, even applied to small molecules in contact, they give a sufficiently accurate approximation for the VDW energies [110]. Thus, the Lifshitz theory can be applied to estimate the binding energies and adhesion forces between two particles in contact. To do so, one needs to identify the contact distance for the interacting substances. Commonly, the contact distance  $D_0$  is taken to be within 0.2 – 0.4 nm. It can, however, exceed the typical range depending on the nature of the short-range repulsive forces [110]. Adhesion energies for several pure lipid bilayers have been measured under various experimental conditions. They range from  $10^{-5}$  J/m<sup>2</sup> to  $10^{-4}$  J/m<sup>2</sup> [114].

2. *Site-specific adhesion.* When the plasma membranes of two cells are in contact, non-covalent bonds may form between proteins embedded into membranes. Interac-

tions between these proteins, known as cell adhesion molecules (CAMs) are specific. They are sensitive to the type and geometric configuration of CAMs. Therefore, these specific interactions are sometimes referred to as ‘lock and key’ or ‘ligand-receptor’ interactions [110].

CAMs mediate adhesive interactions between two cells through their extracellular domains [2]. The CAM of one cell can bind to the CAM of another, forming a homophilic bond. For instance, the CAMs of the cadherin family, discussed in Section 2.3, form mainly homophilic bonds [115]. Another type of binding that CAMs form is called heterophilic, where the two bound CAMs have different types [116]. Finally, cells may adhere to each other indirectly by interactions between cell surface receptors and the extracellular matrix [114]. The binding energies for different protein-ligand pairs vary, but on average, they are at the order of  $\sim 10k_B T$  per bond [114]. For comparison, the covalent energy between two carbon atoms is of order  $\sim 100k_B T$ .

CAMs can be found spread over cell surfaces or concentrated in special spots, called cell junctions. The strength of adhesion depends on the distribution and the number density of adhesive receptors on the cell surface [117, 118]. The contribution of specific adhesion to the total cell adhesion energy is estimated to be  $10^{-17}$  J energy per  $\mu\text{m}^2$  [114]. It is comparable to the non-specific interaction contribution. Thus, both non-specific and specific adhesion mechanisms contribute to cell-cell adhesion with adhesion energy density of order  $10^{-17}$  J/ $\mu\text{m}^2$  [114].

## 3.2 Numerical Methods

### 3.2.1 Introduction

An analytical approach which characterizes the time evolution of complex molecular systems is often impossible. In such cases computer simulations may help to gain insight into the behaviour of the system. Molecular Dynamics (MD) is a computational technique aimed at numerically studying both equilibrium properties and dynamical processes. The idea behind MD is to follow the system’s dynamics by following the time evolution of each particle in the system. To do that, one needs to model individual particles of the system, define the interactions between them, and finally find the trajectories of all particles by solving their equations of motions. In this section we give a brief overview of classical and coarse-grained MD methods. The latter is used to solve the equations of motion in our model in Section 4.2.

Perhaps the most challenging part in MD is the proper modelling of the individual particles of the system and their interactions. Well-defined models omit unnecessary structural details, saving computational time, yet are sufficient to describe the phenomena of interest [21]. The choice of the model depends on the type of the problem, its time and length scales.

In classical MD, the internal structure of the atoms is ignored. Atoms are modelled as spheres, placed at the positions corresponding to their nuclei. Although the electronic structure of an atom is not modelled explicitly, its existence is incorporated into effective atom-atom interactions. Negligence of the structural details of atoms in classical MD makes it suitable for nano-scale problems, with typical time and length scales of 1-100 ns and 10 nm correspondingly.

Most biological processes have time and length scales that far exceed the nano-scale. Sizes of biological membranes or polymer filaments reach micrometers, and time scales can reach hours or even days. Moreover, biological processes often occur at different time scales. For example, the dynamics of *Drosophila* wing growth has three different time scales: The relaxation time due to local perturbations takes several seconds, cell divisions take several hours and the formation and morphogenesis of the wing lasts several days [24]. Such length and time scales are beyond the accessibility of classical MD. To extend the simulation times and lengths, atomistic models can be ‘coarse-grained’. The discussion of coarse-graining below is based on Ref. [21]. In the process of coarse-graining, variables that have dynamics faster than the time scales of interest are eliminated, which reduces the system’s degrees of freedom, and consequently reduces time required for simulation. The dynamics of the system are defined by the time evolution of the slow, coarse-grained variables. Eliminated degrees of freedom are incorporated into effective interactions between the coarse-grained variables. These effective interactions should be carefully calibrated to match atomistic simulations or experimental data. The dynamics of the coarse-grained system is followed by means of coarse-grained MD, where interacting particles are no longer atoms or molecules. Different levels of coarse-graining may be applied to the system, depending on the time and length scale of the phenomenon of interest.

Once the model is established and the effective interactions defined, one can find the trajectories of all particles by solving their equations of motion numerically. A typical numerical integration algorithms consist of the following steps: The integrator breaks down continuous time  $t$  into discrete time steps  $t_n$  with time interval  $\Delta t$ . At each time step, interaction forces are calculated based on the positions of the particles



at the previous time step. These forces are then used to calculate the positions for the next time step based on the equations of motion. As a result, one obtains trajectories for all particles as a set of positions at the consecutive time steps.

In the following sections, we describe the equations of motions for all-atom and coarse-grained systems, as well as describe several numerical integrators.

### 3.2.2 Equations of Motion

*Newton's Equations of Motion:* In classical all-atom MD, the equations of motion are Newton's laws. For a system of  $N$  atoms, the set of equations can be written as

$$m_i \frac{d^2 \mathbf{r}_i}{dt^2} = \mathbf{F}_i, \quad i = 1 \cdots N, \quad (3.20)$$

where  $m_i$  is the mass of  $i$ -th atom,  $\mathbf{r}_i$  is its position and  $\mathbf{F}_i$  is the net force acting on it. A three dimensional system of  $N$  particles with no constraints has  $3N$  degrees of freedom (3 degrees of freedom per particle). Hence, Equation 3.20 is equivalent to a system of  $3N$  second order differential equations.

In order to solve Equation 3.20, one should identify the net force acting on each particle. For a system of  $N$  particles interacting through a potential  $U(\mathbf{r}_1, \mathbf{r}_2, \cdots, \mathbf{r}_N)$ , the force acting on the  $i$ -th particle is given by

$$\mathbf{F}_i = -\frac{\partial U}{\partial \mathbf{r}_i}. \quad (3.21)$$

It can be written as

$$\mathbf{F}_i = \mathbf{F}_i^{ext} + \sum_{i \neq j} \mathbf{F}_{ij}(\mathbf{r}_i, \mathbf{r}_j) + \sum_{i \neq j \neq k} \mathbf{F}_{ijk}(\mathbf{r}_i, \mathbf{r}_j, \mathbf{r}_k) + \cdots \quad (3.22)$$

The first term is the force due to external fields. The second term is the interaction between particle pairs. The third term is the three-body interaction force, etc. Many-body interaction effects should be taken into account when dealing with lattice systems or interactions between large particles and surfaces [111]. The pairwise interaction approximation is sufficient for the purposes of this work. In a closed system,  $\mathbf{F}_i^{ext} = 0$ , and the force in Equation 3.22 is approximated with the sum of pairwise interaction forces,

$$\mathbf{F}_i = \sum_{i \neq j} \mathbf{F}_{ij}(\mathbf{r}_i, \mathbf{r}_j). \quad (3.23)$$

*Langevin Dynamics:* In 1908 Langevin presented a coarse-graining approach to Brownian motion, where large heavy particles are suspended in the liquid of lighter fast moving particles. In the coarse-grained description, the molecules in the liquid are eliminated. The omitted degrees of freedom are replaced by friction and noise terms [119]. The friction term presents the effect of motion in a viscous medium and the noise term replaces the random collisions of the particle with the solvent molecules. This approach has been widely used in biophysical models as a way to eliminate explicit solvent molecules [120], or to sample the system [121, 122].

The Langevin's equation of motion is given as

$$m_i \frac{d^2 \mathbf{r}_i}{dt^2} = \mathbf{F}_i + \mathbf{F}_i^{fric} + \mathbf{R}_i(t). \quad (3.24)$$

Here,

$$\mathbf{F}_i^{fric} = -\gamma_i \frac{d\mathbf{r}_i}{dt} \quad (3.25)$$

is the friction force with friction coefficient  $\gamma_i$  and  $\mathbf{R}_i(t)$  is the stochastic noise term. For Brownian particles that are much heavier than the solvent particles,  $\mathbf{R}_i(t)$  is Gaussian noise, uncorrelated in time and space. Therefore,  $\langle \mathbf{R}_i \rangle = 0$  and  $\langle \mathbf{R}_i(t_1) \mathbf{R}_j(t_2) \rangle \sim \delta_{ij} \delta(t_1 - t_2)$ .

The friction and random terms are related according to the fluctuation-dissipation theorem [123].

$$\langle \mathbf{R}_i(t_1) \mathbf{R}_j(t_2) \rangle = 2k_B T \gamma_i \delta_{ij} \delta(t_1 - t_2), \quad (3.26)$$

where  $T$  is the temperature of the system.

For an overdamped system  $|\gamma_i \dot{\mathbf{r}}| \gg |m_i \ddot{\mathbf{r}}|$ , and the acceleration term can be neglected. This non-inertia regime of Langevin dynamics is known as Brownian dynamics [119] with the equation of motion

$$\begin{aligned} 0 &\approx \mathbf{F}_i - \gamma_i \dot{\mathbf{r}} + \mathbf{R}_i(t) \\ \gamma_i \dot{\mathbf{r}} &= \mathbf{F}_i + \mathbf{R}_i(t) \end{aligned} \quad (3.27)$$

with  $\mathbf{R}_i(t)$  satisfying relation 3.26.

### 3.2.3 Numerical Integration

Equations 3.20 and 3.24 are second order ordinary differential equations. Various integrators have been designed to solve them numerically [124]. From the numerical point

of view, a good algorithm should be accurate and efficient. Numerical integration is always an approximate method. Typically, the analytical solution is approximated with a finite sum during the numerical integration. The difference between the infinite sum and the finite approximation is called truncation error. Numerical integrators with smaller truncation errors have better accuracy. Truncation errors scale as  $\sim \mathcal{O}(\Delta t^n)$  [124], so smaller time steps increase the accuracy of the method. Additionally, smaller time steps lead to numerically more stable algorithms.

Efficiency is another property to consider. The most time consuming part in solving the equations of motion is the calculation of forces. For a system of  $N$  particles with pairwise additive interactions, the algorithm needs to evaluate  $N(N - 1)/2$  distances. Hence, the force calculation time scales as  $N^2$  [20]. Therefore, more efficient algorithms have less force calculations. One can achieve efficiency by increasing the integration time step, which on the other hand decreases accuracy. Well-designed algorithms have higher accuracy for the larger time steps, which allows one to increase efficiency without sacrificing accuracy.

There are also other requirements that should be taken into account. First, Newton's equations of motion are time reversible, so they are invariant under  $t \rightarrow -t$  transformation. Therefore, the integration algorithm should be time reversible as well. Next, Newton's equations of motion are symplectic, so the algorithm should be symplectic as well [125]. Suppose a system with energy  $E$  occupies volume  $V$  in the phase space  $(\mathbf{r}, \dot{\mathbf{r}})$ . Newton's equations of motion transform any given point from  $V$  to another point of phase space. Symplecticity of Newton's equations of motion implies that the transformation preserves the volume of phase space. If volume is not preserved, the transformation violates energy conservation. Time reversibility and symplecticity requirements preclude some common algorithms such as the original Euler or Runge-Kutta methods.

Below we describe the Verlet algorithm, which is used as an integrator in our simulations. They are time reversible, symplectic and show little long-time energy drifts.

*Verlet algorithm:* The Verlet algorithm [126] is derived from Taylor's expansion for the position of the particle. Let the position of the  $i$ -th particle at time  $t$  be  $\mathbf{r}_i(t)$ . Taylor's expansion around time  $t$  will be

$$\mathbf{r}_i(t + \Delta t) = \mathbf{r}_i(t) + \frac{d\mathbf{r}_i}{dt} \cdot \Delta t + \frac{1}{2} \frac{d^2\mathbf{r}_i}{dt^2} \cdot \Delta t^2 + \mathcal{O}(\Delta t^3). \quad (3.28)$$

Similarly,

$$\mathbf{r}_i(t - \Delta t) = \mathbf{r}_i(t) - \frac{d\mathbf{r}_i}{dt} \cdot \Delta t + \frac{1}{2} \frac{d^2\mathbf{r}_i}{dt^2} \cdot \Delta t^2 - \mathcal{O}(\Delta t^3). \quad (3.29)$$

Adding Equations 3.28 and 3.29 gives

$$\mathbf{r}_i(t + \Delta t) + \mathbf{r}_i(t - \Delta t) = 2\mathbf{r}_i(t) + \frac{d^2\mathbf{r}_i}{dt^2} \cdot \Delta t^2 + \mathcal{O}(\Delta t^4). \quad (3.30)$$

From Equation 3.20  $\frac{d^2\mathbf{r}_i}{dt^2} = \frac{\mathbf{F}_i(t)}{m_i}$ , hence

$$\mathbf{r}_i(t + \Delta t) = 2\mathbf{r}_i(t) - \mathbf{r}_i(t - \Delta t) + \frac{\mathbf{F}_i(t)}{m_i} \cdot \Delta t^2 + \mathcal{O}(\Delta t^4). \quad (3.31)$$

The algorithm relies on the positions from the previous two time steps for evaluation of the new positions.

In the Verlet algorithm, velocities are not calculated explicitly, but they can be obtained by subtracting Equation 3.28 from Equation 3.29:

$$\mathbf{r}_i(t + \Delta t) - \mathbf{r}_i(t - \Delta t) = 2\frac{d\mathbf{r}_i}{dt} \cdot \Delta t + \mathcal{O}(\Delta t^3), \quad (3.32)$$

leading to

$$\mathbf{v}(t) = \frac{\mathbf{r}_i(t + \Delta t) - \mathbf{r}_i(t - \Delta t)}{2\Delta t} + \mathcal{O}(\Delta t^2). \quad (3.33)$$

Truncation error in the calculation of positions during one integration step has the order  $\Delta t^4$ . Velocities are less accurate, with truncation error of order  $\Delta t^2$ .

Modifications of the Verlet algorithm evaluate both positions and velocities and are used to calculate the new positions [127, 128]. If better velocity accuracy is needed, one can use the Beeman or velocity-corrected Verlet algorithms (described in [20]).

### 3.2.4 Initial and Boundary Conditions

*Initial Conditions:* In order to solve the system of second order ordinary differential Equations 3.20, one needs to specify initial positions and velocities for each particle.

The initial positions are usually chosen based on the compatibility with the structure of the system. Particles can be placed at the sites of various lattices or they can be randomly distributed throughout the system [127]. Initial positions should be chosen carefully, so particles do not overlap. This is especially true for randomly generated

initial positions. Overlapping will generate strong repulsive forces, which, in turn, will destabilize the system.

The initial velocities can be taken randomly from the velocity distribution function of the system equilibrated at temperature  $T$ , The Maxwell-Boltzmann distribution [129]

$$p(v_i) = \sqrt{\frac{m_i}{2\pi k_B T}} \exp\left(-\frac{m_i v_i^2}{2k_B T}\right). \quad (3.34)$$

Since the properties of the system in equilibrium do not depend on the initial conditions, the precise choice of the initial conditions is not necessary. The positions of the particles and their velocity distributions will readjust during the equilibration process. However, a reasonable choice of initial conditions speeds up equilibration.

*Boundary Conditions:* When simulating a system, one should take care of its boundaries. In this section we give a brief overview of commonly used boundary conditions.

Free boundary conditions do not assume any boundaries, and particles are not restricted to occupy a specific region in space. This type of the boundary is suitable for studying isolated molecules or clusters in the vacuum [129].

To mimic the motion of particles within a limited volume, one can use rigid boundaries as the walls. Rigid boundaries in an MD simulation introduce particle distribution artifacts near the walls. In a system of  $N$  particles, approximately  $\sim N^{2/3}$  are located at the surface. For a macroscopic system of  $10^{23}$  particles only a small fraction of about  $10^{15}$  molecules are adjacent to the surface, However, in an MD simulation, which is typically run for a few hundred to a few thousand molecules, a large portion of particles is adjacent to the walls and their contribution to the state of the system cannot be neglected [20]. Thus, rigid boundaries should be avoided when the bulk properties of the system are examined.

The most common boundary conditions, periodic boundary conditions (PBC), are used to study system properties in the bulk, away from any surfaces. PBC eliminate surfaces by surrounding the system with its identical copies (Fig. 3.5). This way, PBC mimic an infinite bulk around the system. In a system with PBC, each particle  $i$  in the central computational box has its images  $i'$  in surrounding boxes. Once a particle leaves the simulation box from one side, it enters the same box from the opposite side with identical velocity, as shown in Figure 3.5.

Due to its simplicity, rectangular boxes are often used; however, that is not a requirement. The computational box can have a shape of any space-filling polyhedra.

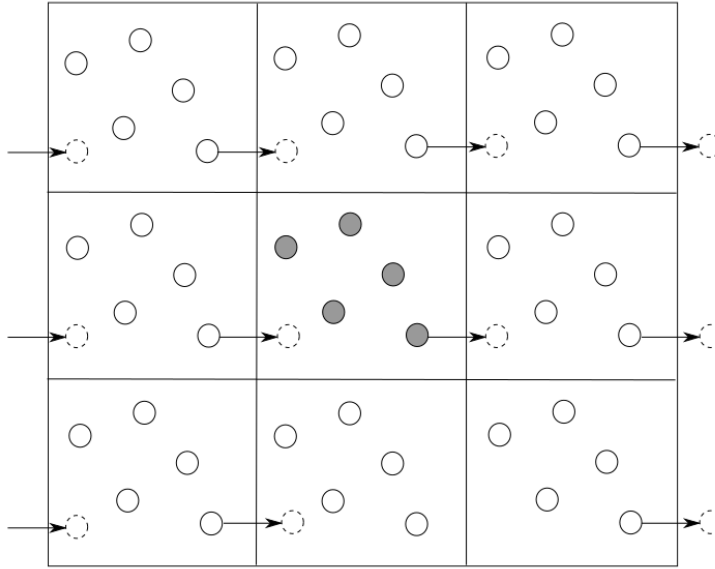


Figure 3.5: Periodic Boundary Condition. Simulation box is surrounded by infinite copies of itself. As a result, when particle leaves the box from one face, an identical particle with the same velocity enters the box from the opposite cell.

Examples are rhombic dodecahedron [130] or truncated octahedron. Usage of alternative simulation boxes can reduce the size of the system.

PBCs bring periodicity into the system, which is characteristic to only crystal-like structures. When liquid or gaseous systems are simulated, one needs to make sure that artefacts due to periodicity are minimized. This can be achieved by applying the minimum image convention [20]. In a system that satisfies the minimum image criterion, every particle interacts with only the nearest image of each of the other particles (Fig. 3.6). This condition holds if the size of the simulation box is no less than twice the cutoff distance of interaction forces. Another limitation of PBC is the absence of fluctuations with long wavelengths. Since artificial periodicity is introduced to the system, fluctuations are limited to the ones whose wavelengths are multiples of the simulation box size. Any fluctuations with wavelength longer than the length of the box are not present.

Boundary conditions mentioned above are just a few of the available boundary conditions. More sophisticated boundary conditions or a combination of boundary conditions can be applied to treat boundaries when needed.

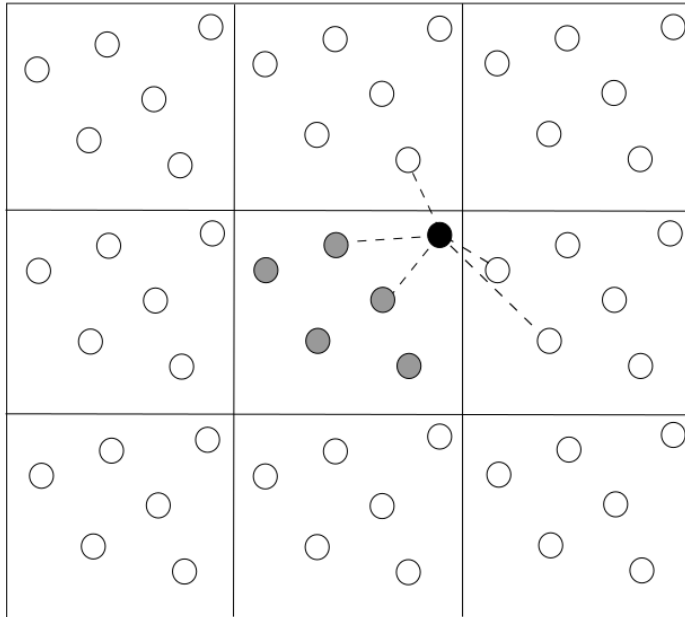


Figure 3.6: Minimum image convention. To minimize artificial periodicity, each particle interacts only with the nearest image of the other particle.

### 3.2.5 Packing of particles: Voronoi Diagram

The topology of cells in tissue is characterised by the number of nearest cells. One can characterize the position of each cell in the space by the position of its center of mass. Thus cells in tissue can be characterized by the set of points corresponding to the cells' centers of mass. The identification of the nearest cells to the given cell is then equivalent to the finding of the set of points closest to the given point. To solve this problem, one might consider construct called the Voronoi diagrams. The concept of a Voronoi diagram or Dirichlet tessellation was introduced and studied by Dirichlet in 1850 and Voronoi in 1908 [131]. For a given set of distinct points in space, called sites, the Voronoi diagram divides the space into as many regions as there are sites. Each site is assigned a region such that all the points inside that region are closer to the associated site than to any other site. An illustration of a Voronoi diagram for a random set of points in two dimensions is shown in Figure 3.7. This construct is used in various disciplines and often has different names: *Wigner-Seitz zones* in condensed matter physics [132], *domains of action* in crystallography [131] and *Thiessen polygons* in geography [133] are built based on the same principle.

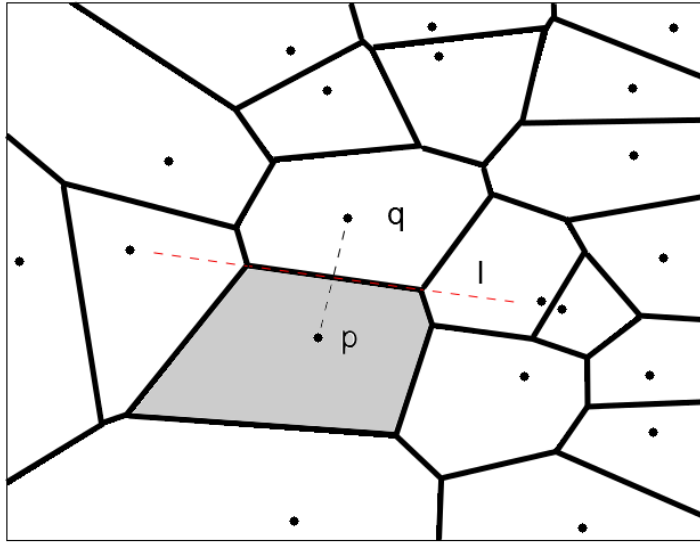


Figure 3.7: A two dimensional Voronoi diagram for a random set of points. The Voronoi cell (shown in grey) associated with the site  $p$  is the region which is closest to the site. It is defined by the intersection of bisectors (red dashed line) of  $p$  and any other site  $q$ .

A mathematical definition of the Voronoi diagram is given as follows [131]: Let  $S$  be the set of  $n$  points (sites) in Euclidean plane  $\mathbb{R}^2$ , and let  $p$  and  $q$  be two distinct sites from set  $S$  (Fig. 3.7). A portion of the plane  $\mathbb{R}^2$  in which all the plane points are closer to  $p$  than to  $q$  is called the dominance of  $p$  over  $q$ .

$$\text{dom}(p, q) = \{x \in \mathbb{R}^2, \text{ if } d(x, p) \leq d(x, q)\},$$

where  $d(x_1, x_2)$  is the Euclidean distance between points  $x_1$  and  $x_2$ . The Voronoi region or Voronoi cell of the site  $p$  is the intersection of dominances of  $p$  over all other sites in the set  $S$  (grey region in Fig. 3.7).

$$\text{Voronoi region}(p) = \bigcap_{q \in S, q \neq p} \text{dom}(p, q).$$

In order to find the dominance of  $p$  over  $q$ , one should construct a perpendicular bisector of  $p$  and  $q$  (dashed red line in Fig. 3.7). The perpendicular bisector divides the plane  $\mathbb{R}^2$  into two half planes. All the points of the half plane that contains  $p$  are closer to  $p$  than to  $q$ . Thus, the half plane that contains  $p$  is the dominance of  $p$  over  $q$ . The intersection of all dominance half planes that arise from constructing bisectors of  $p$  and any other site is the Voronoi region of  $p$ . Collectively, the Voronoi regions for all



sites divide the plane into  $n$  parts. That partition is called the Voronoi diagram. In the two dimensional case, the Voronoi regions are polygons with maximum of  $n - 1$  edges and vertices. The Voronoi diagram can be generalized for  $n$ -dimensional spaces. The Voronoi diagram has its dual structure, called *Delaunay triangulation*. It is constructed by connecting two sites in a Voronoi diagram that share a common edge [131].

Physical systems consist of discrete particles. The spatial distribution of particles describes the state of the system and its equilibrium properties. One way to obtain information about the local organization of particles in the system is to consider each particle as a distinct site in three dimensional space and to construct a Voronoi diagram for the set of particles [127]. The Voronoi subdivision partitions space into polyhedra associated with the particles. Two particles are considered to be nearest neighbors if they share a common face. Thus, each polyhedron characterizes the local neighborhood of the associated particle, and all polyhedra combined provide information about the spatial structure of the system.

# Chapter 4

## Model and Methods

Having a precise topology is essential for the proper functioning of tissue. During tissue development, various cellular processes, such as cell division, rearrangement, migration and cell death alter tissue topology, and the cellular packing may significantly differ at the various stages of tissue development. For example, the *Drosophila* wing has an irregular topology throughout most of its growth and formation; however, at the last stage of development, cells are repacked into a mostly hexagonal structure [77]. Cell mechanics also affects topology, as changes in mechanical properties of the cell reflect on its shape and connectivity [73, 26, 27].

Recently, a lot of attention has been drawn towards understanding the mechanisms that drive cell packing in epithelium. In particular, mechanical vertex models [27] are widely used to investigate the impact of cell mechanics and cellular processes on epithelial tissue topology. However, vertex models have their limitations. Cells have a pre-existing shape and topology, and vertex models do not account for cell migration.

Individual treatment of cells allows a for more realistic and detailed description of cellular shapes and topology. In these models, cells respond to the changes in external environment in a more natural way. Single cell based models were extensively used to study the dynamics of multicellular structures (a brief review of selected single cell based models is presented in Chapter 2). However, only a few works have addressed cell packing topologies.

In this work, we present a new single-cell based model which accounts for cell-cell adhesion and the cell cortex's contractility. The processes of cell growth and divisions are included in the model, which makes it suitable for studies of tissue growth. We discuss the details of the model in Section 4.1. The parametrization and the algorithm of tissue growth are presented in Section 4.2.

## 4.1 Model

A model for an isolated cell is developed first. That cell is then embedded in a tissue where it interacts with its neighboring cells. These interactions are modelled through repulsion, adhesion, and viscous damping. Importantly, the cells are also able to grow, divide and migrate. All the quantities and their numerical values are presented in dimensionless units.

### 4.1.1 Isolated Cell

A single cell is modelled as a closed loop of mass points connected through springs. This model was proposed by Åström and Karttunen in their studies on cell aggregation in a confined space [134]. We use this model as the basis and extend it to include cell-cell interactions and cell division. Each mass point experiences tension forces from two neighbor springs as shown in Figure 4.1A. These tension forces define the cell actomyosin cortex's contractility that favours a rounded structure for an isolated cell [11, 95]. Each cell is also assigned an internal pressure  $P$  independent of cell area. This is motivated by experimental observations from dividing cells [11]. The force due to the internal pressure (in this work referred as pressure force) is opposed by the spring tension forces of the two nearest neighbor mass points. An increase in internal pressure results in an increase in the size of the cell. With the above, the net force acting on mass point  $i$  belonging to an isolated cell is given as

$$\mathbf{F}_i^{cell} = \sigma_i \eta_i - \sigma_{i+1} \eta_{i+1} + \frac{Pl}{2} (\nu_i + \nu_{i+1}), \quad (4.1)$$

where  $\eta_i$  and  $\nu_i$  are the tangential and normal vectors,  $\sigma_i$  is the tension force and  $Pl$  represents pressure force, as shown in Figure 4.1A. For a linear elastic spring, tension is given as  $\sigma_i = K_i^{spr} (l - l_0)$ , where  $l_0$  and  $l$  are equilibrium and instantaneous length of springs, respectively. For simplicity, we assume that all cells are identical and homogeneous: i.e., all springs have the same spring constant  $K_i^{spr} \equiv K^{spr}$ .

### 4.1.2 Cell in tissue

Next, we place the cell as described above in a tissue. Inside the tissue, each mass point is subject to additional forces that arise due to cell-cell interactions. We model them using three terms: 1) repulsion, 2) adhesion, and 3) viscous damping.

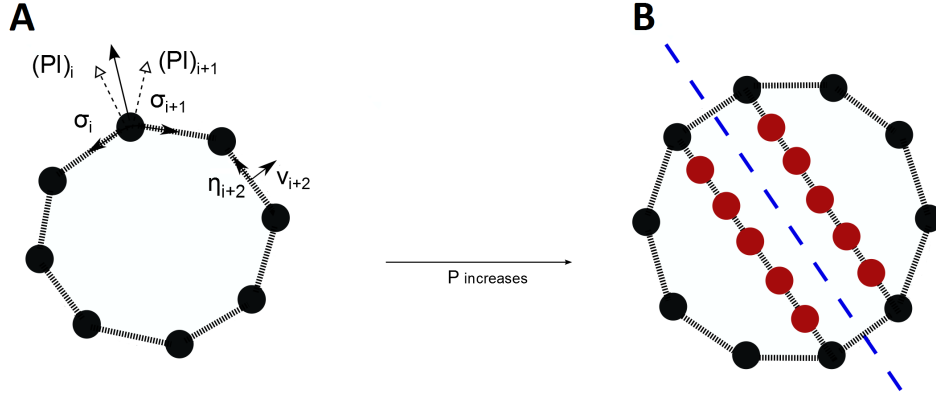


Figure 4.1: Mass-spring model of the cell. (A) Forces acting on mass point  $i$  in an isolated cell are spring tension forces ( $\sigma_i$  and  $\sigma_{i+1}$ ) and the pressure force ( $(Pl)_i$  and  $(Pl)_{i+1}$ ). The cell grows by gradually increasing the pressure force. (B) The cell divides through random division line (dashed blue line). During division, new mass points (red) are added along the division line.

1. *Repulsion:* In order to prevent the cells from penetrating into each other, we use spring-like repulsion forces

$$\mathbf{F}_{ij}^{rep} = \begin{cases} -K^{rep}(R_c^{rep} - R_{ij})\hat{R}_{ij} & \text{if } R_{ij} < R_c^{rep} \\ 0 & \text{otherwise.} \end{cases} \quad (4.2)$$

Here  $K^{rep}$  is the repulsion spring constant,  $R_{ij}$  is the length between two mass points  $i$  and  $j$ , and  $\hat{R}_{ij}$  is the unit vector. Two mass points are considered to be in contact if they are within a distance  $R_c^{rep}$  from each other.

The repulsion force should be strong enough to counteract the pressure force  $Pl$  pushing the mass points of one cell into the interior of one (or more) of its neighboring cells. In addition, cell rigidity needs to be taken into account for the estimation of the repulsion force. Rigidity may vary at different stages of the cell cycle [135], and since the displacement of the mass points depends on the strength of the spring forces, more rigid cells require stronger repulsion forces.

Taking the two above factors into account, we can estimate the numerical value for the repulsion force coefficient required to be

$$K^{rep} \sim K^{spr} Pl. \quad (4.3)$$

2. *Adhesion*: Tissue integrity is maintained by adhesion between the neighboring cells. Cells adhere to each other tightly through adhesive molecules, often located in specific areas known as cell junctions [80]. In our model, each mass point acts as a potential site for adhesive interaction. When two mass points  $i$  and  $j$  that belong to different cells are within the interaction distance  $R_c^{adh}$ , they attract each other through linear spring-like forces,

$$\mathbf{F}_{ij}^{adh} = \begin{cases} K_{ij}^{adh}(R_c^{adh} - R_{ij})\hat{R}_{ij} & \text{if } R_{ij} < R_c^{adh} \\ 0 & \text{otherwise.} \end{cases} \quad (4.4)$$

Cells adhere through several mechanisms with different associated binding free energies. A realistic treatment of cell-cell adhesion should consider the differences between the adhesion sites, and  $K_{ij}^{adh}$  should be different for different mass points pairs. For simplicity, however, in this work we assume that all adhesive sites are identical with the adhesion spring constant  $K_{ij}^{adh} \equiv K^{adh}$ .

Adhesion favours cell-cell contacts and tends to flatten the neighboring cell surfaces, whereas cell cortex contractility favours a rounded cell structure [95]. We can estimate the relation between the adhesion and contractility spring constants by using the preferred cell shapes inside a tissue. The majority of cells in a proliferating epithelium assume hexagonal shapes [19]. The change of shape from circular to hexagonal is accompanied by work done against the contractile springs. In the absence of internal pressure forces, this work is compensated by the energy stored in the adhesive springs  $W^{spr} \sim W^{adh}$ . To estimate the work  $W^{spr}$  required to deform the cell, we assume that the cell has the shape of a regular hexagon with an incircle of radius  $r$ . The total change in the perimeter can then be estimated as  $\Delta L = L_{hex} - L_{cir} = 12/\sqrt{3}r - 2\pi r$ . The total deformation is the result of the deformation of  $N$  springs. Hence, the deformation of each spring is equal to  $\Delta x = \Delta L/N$ . The total energy associated with the deformation of springs can be estimated as  $W^{spr} \sim NK^{spr} \cdot (\Delta L/N)^2 \sim 10^{-1}K^{spr}r^2/N$ . For a hexagonal shape, all mass points are in contact with the mass points of the neighboring cells and participate in cell-cell adhesion with the total energy of  $W^{adh} \sim NK^{adh} \cdot (R_c^{adh} - R_c^{rep})^2$ . Thus

$$K^{adh} \sim \frac{10^{-1}K^{spr}r^2}{N^2 \cdot (R_c^{adh} - R_c^{rep})^2}. \quad (4.5)$$

This estimate does not include the effects of the internal pressure force on cellular shapes, and hence the final calibration of  $K^{adh}$  is done during the simulations where we methodically vary numerical values for the adhesion constant and compare resulting

tissue topology with the experimental data.

3. *Viscous Damping:* Cells can undergo local rearrangements as well as large-scale migrations during tissue formation. The extent of these rearrangements depends on the interactions of cells with their exteriors. We can control the amount of cell rearrangements through a viscous damping force that acts between two neighboring cells. Let  $i$  and  $j$  be two mass points that belong to two different cells that are in contact. When the cells move along each other, the mass point  $i$  slides along mass point  $j$  with the relative velocity  $\mathbf{v}_{ij} = \mathbf{v}_i - \mathbf{v}_j$ . If  $\mathbf{v}_{ij}^\tau$  is the tangential component of the relative velocity, then the damping force acting on mass point  $i$  can be given as

$$\mathbf{F}_{ij}^{fric} = -\gamma_i \mathbf{v}_{ij}^\tau. \quad (4.6)$$

Furthermore, since we do not consider the cellular environment explicitly, the effect of motion on the viscous cytoplasm is mimicked through an additional viscous damping force with a coefficient  $c$  that acts on all mass points.

### 4.1.3 Cellular processes

Our model can account for cell polarity and several cellular processes including cell growth and division, and cell migrations. We discuss the modelling of those processes below.

1. *Cell Growth and Division:* The cell grows by gradually increasing internal pressure  $P$ . The growth through internal pressure is inspired by the fact that animal cells modulate their internal hydrostatic pressure before mitosis [11]. The current implementation of the model assumes that all cells have the same pressure which grows at the same constant rate, but the model can be easily extended to assume various growth mechanisms as well. The individual modelling of cells allows one to vary the internal pressure and the growth rate for each cell independently.

Once the cell area reaches a threshold value  $A^{div}$ , the cell divides into two daughter cells. The model is scale invariant, and without loss of generality we can choose the numerical value for  $A^{div}$  to be unity. This sets the length scale in our model. The increase in the internal pressure for mitotic cells observed by Stewart *et al.* [11] serves as a basis for the growth control through pressure in our model. To ensure that daughter cells grow similarly to the mother cell, both cells are assigned a pressure identical to the parental cell. During the division, new mass points are added along the division line so that the resulting two cells form closed loops and have the same number of mass

points as the initial cell. We consider three division mechanisms: *random*, divisions by the ‘*longest axis rule*’ or *Hertwig’s rule* and *asymmetric* cell division (Fig. 4.2). In

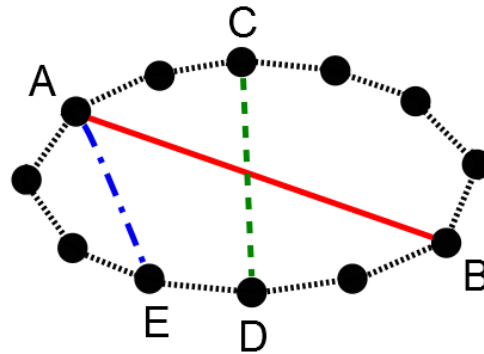


Figure 4.2: Three mechanisms of cell division. A *random* (AB) division line passes through the cell’s center of mass and has random orientation. Division based on *Hertwig’s rule* (CD) has a division line that is perpendicular perpendicular to the cell’s longest axis. An *asymmetric* division line (AE) splits the cell into two unequal sizes and has random orientation.

random division scheme, the division line passes through cell’s center of mass and has random orientation. This division line divides the cell into two roughly identical cells. Here we assume homogeneous cells, with all mass points having the same mass and all spring constants being the same. With that assumption, we consider a random division line to be one that connects a randomly chosen mass point to its diagonally opposite mass point (line AB in Fig. 4.2). Two other division mechanisms are chosen based on biological relevance. More than a century ago Hertwig proposed a division rule based on his observations on mitotic cells. For most cells the mitotic spindle aligns along the longest axis of the cell. Hence, the cell division plane is oriented perpendicular to the longest axis. This division scheme is known as the ‘*longest axis rule*’ or ‘*Hertwig’s rule*’. We implement the division according to the ‘*longest axis rule*’ by searching for the cell’s longest axis and then choosing the division line closest to the line that is perpendicular to the longest axis (line CD). Finally, in some cases, cells divide asymmetrically. During asymmetric division, two daughter cells end up with different sizes [69]. Numerically, we construct the asymmetric division line by considering the line which connects a randomly selected mass point with another one that is not diagonally opposite to the first mass point (Fig. 4.2 (AE)).

2. *Cell Polarity and Migration*: The model can account for cell polarity and migration (not included in this work). Polar cells are characterized by differences in shape,

structure or functionality of spatially different regions of the cell. An epithelial cell is an example of a polar cell, where an individual cell is divided into two distinct regions, apical and basolateral. The apical region faces the lumen or outer surface, while the basolateral region is in contact with the basal lamina or other cells. Exposure to different environments requires having different structure and functionality of apical and basolateral membranes of epithelial cell. Since our model the cell is presented as a collection of sub-cellular mass points, we can model cell polarity by varying properties of mass points that belong to distinct parts of the cell.

Collective cell migrations during the an embryonic development are an essential part of morphogenesis [97, 98]. Cell polarity plays an important role in cell migrations. For a cell to move in a specific direction, it should have defined front and rear parts. As a cell migrates, the leading edge extends towards the direction of motion, while the opposite edge retracts [136]. We can model the migration through modulation of the pressure forces acting on mass points that belong to the leading and the retracting edges of cell. If the mass points that belong to the leading edge are assigned a higher internal pressure  $P$  than the mass points of the neighbor cells, the leading edge extends outwards. Similarly, if the internal pressure of the mass points that belong to the rear edge of the cell is set to be lower than that of the internal pressure of the neighboring cell mass points, the rear edge retracts. Consequently, the cell moves generally in the direction of the motion of the leading edge.

## 4.2 Numerical Implementation

The system of cell mass points evolves according to the following set of equations of motion.

$$m\dot{\mathbf{r}}_i = \mathbf{F}_i^{\text{cell}} + \sum_j \mathbf{F}_{ij}^{\text{adh}} + \sum_j \mathbf{F}_{ij}^{\text{rep}} + \sum_j \mathbf{F}_{ij}^{\text{fric}} - c\mathbf{v}_i, \quad (4.7)$$

where  $m$  and  $\mathbf{r}_i$  are the mass and position of mass point  $i$  and  $c$  is the damping coefficient. The forces are given by Equations. 4.1, 4.4, 4.2 and 4.6. The first four terms characterise the physical properties of the cell and the cell-cell interactions as described above. The cellular environment is taken into account implicitly through viscous damping with the damping coefficient  $c$  (see above). We use the Verlet algorithm for numerical integration of Equation 4.7, where positions and velocities at each time step are



obtained through equations

$$\mathbf{r}_i(t + \Delta t) = 2\mathbf{r}_i(t) - \mathbf{r}_i(t - \Delta t) + \frac{\mathbf{F}_i(t)}{m_i} \cdot \Delta t^2 \quad (4.8)$$

and

$$\mathbf{v}_i(t + \Delta t) = \frac{\mathbf{r}_i(t + \Delta t) - \mathbf{r}_i(t)}{\Delta t}. \quad (4.9)$$

### 4.2.1 Simulation of Tissue Growth

We start the simulation of tissue growth from a few cells. As the system evolves according to Equation (4.7), the cell changes its shape due to the interactions with the external environment. At the beginning of the simulation the cell is assigned an initial pressure  $P_{init}$ , such that the resulting cell area is about the same as the threshold area  $A^{div}$ . Cell growth is achieved by increasing the internal pressure at a constant rate. All cells have the same internal pressure and the same pressure growth rate. Different pressures and growth rates can be used, but for simplicity and to demonstrate the model, we used same pressures and growth rates. After a fixed amount of time  $T^{div}$  we check the areas of all cells and the ones that have an area exceeding a threshold value divide according to the procedure described in Section 4.1.3. We discuss the choice of  $T^{div}$  in Section 4.2.2. Following the procedure above, we grow tissues up to 1500 cells.

We use open boundary conditions to mimic tissue growth in a natural environment. To study the properties of the growing tissue, data are typically collected from the central part, which we define as the disc with the radius  $R = 0.6R_{max}$ , where  $R_{max}$  is the largest distance of cells from the center of mass of the system at the given time, as shown in Figure 4.3. We estimated the effects of the boundary to be less than 10%.

All simulations are carried out for four samples in which we applied different initial configurations as follows: a single cell, and clusters of five, ten and twenty cells (Fig. 4.4). The initial configurations of cell clusters were generated by grouping cells together in a tissue-like structure. The systems were equilibrated at the constant pressure  $P$  prior the production simulations. We considered systems to be properly equilibrated when there were no noticeable changes in cell shapes. All results are averaged over those four samples and are reported in dimensionless units. Error bars correspond to the standard deviation over all four samples. Conversion between dimensionless and real units is discussed in the following section.

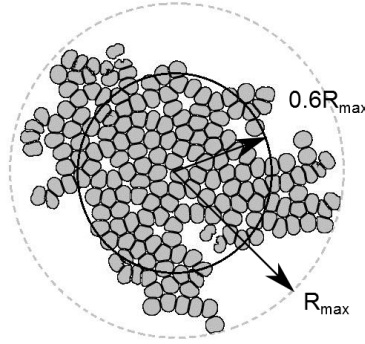


Figure 4.3: Data are collected from the central part of the tissue to avoid boundary effects.

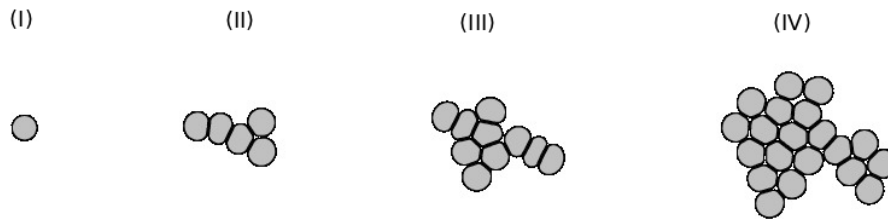


Figure 4.4: Initial configuration of four simulation samples. Cells are grouped in tissue-like structures and equilibrated prior to the beginning of the production simulations.

## 4.2.2 Parametrization

Each cell was constructed from 76 mass points resulting in smooth cellular shapes. All mass points have the same mass  $M$ . Numerical values for the mass should be large enough to prevent rapid oscillations of the model springs in the system. At the same time in the regime of quasi-equilibrium tissue growth, the mass should be small enough so that  $M\ddot{r}_i \ll 1$ . We found that  $M = 0.1$  with damping coefficient  $c = 1$  satisfies both conditions.

Next, we set the threshold area for cell division to unity so the distances between neighboring mass points is roughly  $\sim 0.1$ . The distance at which cells are considered to be in contact or  $R_c^{rep}$  is set to the same value. The cutoff distance for cell-cell adhesion  $R_c^{adh}$  is twice of the contact distance.

Division times for individual cells are characterized by the parameter  $T^{div}$ . The choice of  $T^{div}$  sets the time scale in our model. Typical cell division time has the

order of  $\sim 1$  h, while the characteristic time for tissue development is  $\sim 10$  h [11, 18]. Thus, cell division times are roughly 10 times shorter than the time scale of tissue morphogenesis. We pick  $T^{div}$  such that the characteristic time for tissue growth and formation in our model has the order of  $\sim 1$  in reduced units. This leads to  $T^{div}$  of order  $\sim 10^{-1}$ .

The initial pressure force  $P_{init}l$  and cell cortex contractility were chosen such that the resulting cell area is close to the threshold area  $A^{div}$ .  $K^{rep}$  and  $K^{adh}$  are first estimated with the help of Equations 4.3 and 4.5. We then calibrate these coefficients, along with the pressure force growth rate  $\Delta(Pl)$  and damping coefficient for cellular rearrangements  $\gamma$ , by methodically varying these parameters and comparing resulting tissue topologies with experimental data. The list of computational parameters and their numerical values in dimensionless units is presented in Table 4.1

Table 4.1: List of simulations parameters and their values in dimensionless units

| Parameter                          | Notation     | Numerical Value   |
|------------------------------------|--------------|-------------------|
| Mass points per cell               | $N$          | 76                |
| Mass                               | $M$          | 0.1               |
| Damping of the system              | $c$          | 1                 |
| Equilibrium spring length          | $l_0$        | 0.1               |
| Cell cortex contractility          | $K^{spr}$    | 1400              |
| Cell-cell adhesion coefficient     | $K^{adh}$    | 56                |
| Damping of cellular rearrangements | $\gamma$     | 20                |
| Threshold area                     | $A^{div}$    | 1                 |
| Initial pressure force             | $P_{init}l$  | 15                |
| Pressure force growth rate         | $\Delta(Pl)$ | $5 \cdot 10^{-5}$ |
| Repulsion cutoff distance          | $R_c^{rep}$  | 0.1               |
| Adhesion cutoff distance           | $R_c^{adh}$  | 0.2               |
| Simulation time step               | $\Delta t$   | 0.0001            |
| Division checkpoints               | $T^{div}$    | 0.2               |

We compare parameters in our model with experimentally observed physical properties of the cell. The parameters in our model are in reduced units, and to define the base for conversion to real units we match model cell mass, diameter and internal pressure force with the experimental values.

The average cell diameter is about  $10 \mu\text{m}$ . The diameter of the cell is of the order of unity in reduced units. Thus, the unit length has the real value of  $[l] = 10^{-5}$  m. Cells were chosen to have the mass of an average human cell, or  $10^{-12}$  kg [2]. The number of mass points per cell is  $\sim 100$ , and in reduced units, the total mass of the cell is approximately 10, leading to the mass unit value of  $[m] = 10^{-13}$  kg. To estimate

the real value of the unit force, we use the experimental value of the pressure force in the mitotic cell based on the work of Stewart et al. [11] The experimental pressure has the order of  $\sim 0.1 \text{ nN}/\mu\text{m}^2$ . The reduced pressure force throughout all simulations is of the order  $Pl \sim 10 \Rightarrow P \sim 10/l \sim 100[F]/[l]$  in two dimensions. Similarly, three dimensional pressure in reduced units has the numerical value of  $P \sim 100[F]/[l]^2$ . Substitution of the real value for the length unit and comparison with the real mitotic pressure leads to the force unit of  $[F] = 10^{-10} \text{ N}$ . The time unit can be derived as well,  $[t] = \sqrt{[m][l]/[F]} \sim 10^{-4} \text{ s}$ . To summarize: the conversions of base units are given as  $[m] = 10^{-13} \text{ kg}$ ,  $[l] = 10^{-5} \text{ m}$  and  $[t] = 10^{-4} \text{ s}$ . With these definitions, we can compare the physical properties of our model cell with the experimentally observed cell cortex contractility and cell-cell adhesion.

In their experiments with single mitotic cells, Stewart et al. evaluated the Young's modulus of mitotic HeLa cells to have the order of  $Y \sim 1 \text{ nN}/\mu\text{m}^2$  [11],  $Y \sim 10^3 [F] / [l]$  in dimensionless units. The three dimensional Young's modulus is related to the two dimensional Young's modulus as  $Y_{2D} \sim 4Y_{3D} \sim 10^3 [F] / [l]$ . At the same time, Young's modulus estimate for our model cells can be expressed through the spring constant  $K^{spr}$  as  $Y = K^{spr}l/d$ , where  $l$  is the spring length and  $d$  is the cortex thickness. We set the cortex thickness to be  $100 \text{ nm}$  [137], or  $10^{-2}$  in reduced units. The numerical value for Young's modulus estimated with our model then will be  $Y \sim 10^4 [F] / [l]$ , roughly 10 times higher than the experimentally observed stiffness for the HeLa cell cortex. This difference of order of magnitude can be explained by the fact that our model is two dimensional, whereas experimental data are obtained for three dimensional cells.

Cell-cell adhesion is mediated by adhesion proteins. Depending on the type of adhesion proteins, protein-ligand binding can have varying binding free energy. In particular, Sarda *et al.* [118] estimated the binding energy density for biotin-streptavidin to be  $\sim 10^5 k_B T / \mu\text{m}^2 = 10^{-16} \text{ J}/\mu\text{m}^2$ . The adhesion energy per single bond in our model is  $W^{adh} \sim K^{adh} \cdot (R_c^{adh} - R_c^{rep})^2 \sim 0.56 [F] / [l]$ . The unit length has 10 bonds, thus the binding energy density in our model is proportional to  $1 [F] / [l] \sim 10^{-15} \text{ J}$ . We conclude that our binding energy is roughly 10 times higher than the experimentally observed one. As in the case of Young's modulus, the order of magnitude difference can be explained by the two dimensionality of our model.

Finally, we compare the time scale in our model with the time scale of tissue growth in *Drosophila* imaginal wing disc. The time scale that characterizes tissue growth in our model can be estimated as the simulation time necessary to form a relatively stable configuration of cell nearest neighbors. It takes roughly 25 division cycles, or 5 reduced

time units, for the number of cell neighbors to stabilize. Our model is scale invariant, with the time and viscous damping coefficient scaling as  $c/t$ . In model units, both damping and time units are set to one. At the same time, *Drosophila* wing disc growth and formation has the characteristic time of  $\sim 10$  h [18], and the cytoplasmic viscosity, which corresponds to  $c$  is about  $10^3$  Pa-s [104]. Rescaling model parameters reveals that we, for computational efficiency, speed up the growth rate by roughly a factor 10 compared to *Drosophila* wing disc.

### 4.3 Summary

In this chapter, we presented a framework for proliferation of two-dimensional tissue, such as simple epithelium. Each cell is modelled individually, as a collection of sub-cellular mass points. Cell-cell adhesion and cortex contractility are considered in the model. Hydrostatic pressure is used to control the cell growth. To keep our model simple, we use linear spring forces to model cell mechanics and cell-cell interactions. With the assumption of identical cells, two parameters  $K^{spr}$  and  $K^{adh}$  describe the cell cortex's contractility and cell-cell adhesion. The cytoplasmic cellular environment is taken into account implicitly, as a viscous damping.

We introduced tissue proliferation as a repeating cycle of cellular growths and divisions and presented the numerical implementation of both processes. The possible extensions of the model to account for differential growth, cell polarity and migrations were discussed.

We discussed the parametrization of our model (the list of parameters in reduced units is presented in Table 4.1) and compared the physical properties of the cells in our model with the experimental measurements. Our comparison shows that the Young's modulus of the cell and cell-cell adhesion are roughly 10 times higher than the corresponding experimental values, which is a consequence of the two-dimensionality of our model. Comparison of model time scales with the time scales of epithelial growth showed that we have roughly 10 times faster growth.

## Chapter 5

# The Dynamics of Proliferating Epithelium

Epithelia are often used as model system to study tissue growth and morphogenesis. Proliferating epithelium is particularly well characterized in the *Drosophila* wing disc [74]. The wing primordium (wing imaginal disc) is singled out at the early stages of embryonic development, when it consists of just a few cells. As the wing undergoes proliferation, the number of cells increases more than  $\sim 1000$ -fold in just 4 days to form an adult fly wing [138].

Proliferation is characterized by the mitotic index, which defines the fraction of cells in mitosis. On average, the mitotic index in the proliferating wing disc has a value of  $\sim 1.7\%$  [24]. It, however, varies throughout tissue development [83]. The mitotic index is higher at the initial stages of development, when the growth is faster, and gradually decreases with time, as shown on Figure 5.1. The proliferation of the wing disc is spatially homogeneous, and mitotic cells are found throughout the entire tissue [24].

Despite the disorder introduced by cell division and rearrangement during tissue growth, cell packing topologies in proliferating epithelia are conserved among species [19]. The characteristic topology has a peak for hexagonal cells, and an asymmetric distribution of pentagons and heptagons. In particular, Gibson *et al.* [19] reported that 45.8% of cells in proliferating *Drosophila* wing disc have a hexagonal shape, 27.2% are pentagons and 20.3% are heptagons. The remaining 4.2% cells consists of tetragons and octagons.

In this chapter, we simulate tissue growth starting from a few cells and investigate several aspects of proliferation in our model as detailed in Chapter 4. The procedure

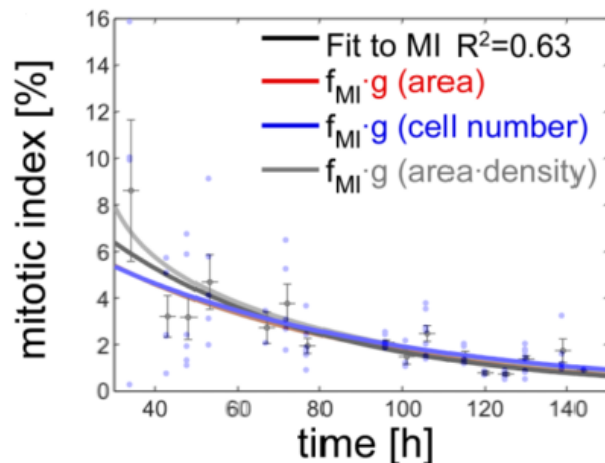


Figure 5.1: Mitotic index of *Drosophila* wing disc determined by PH3-staining. Raw data are displayed as blue points, black points correspond to the mitotic index averaged over tissue samples, and the black line is an exponential fit to averaged mitotic index, weighted with  $1/SE^2$ , where SE is the standard error of averaging. The figure is adapted from [83] and reprinted with permission from AAAS.

of the tissue growth is detailed in Section 4.1.3 and the simulation parameters can be found in Table 4.1. Here we give just a brief overview of the growth process, focusing on the details of simulations relevant to this chapter.

## 5.1 Time evolution of mitotic index

Tissue growth starts from a few cells that start to grow and divide. Periodically, every  $T^{div}$  steps, the areas of all cells were evaluated to establish their eligibility to divide. Cells with areas exceeding the threshold area  $A^{div}$  were divided through randomly oriented division planes. Figure 5.2 shows snapshots of the simulated tissue growth. To characterize proliferation in the model tissue, we follow the time evolution of the mitotic index for four simulation samples (the choice of samples is discussed Sect. 4.2.1). Since we use open boundary conditions, data are collected from the central part of the tissue, which we define as a disc with radius  $0.6R_{max}$ . Here,  $R_{max}$  is the maximum distance of cells from the center of mass of the tissue at the given time.

Every  $10T^{div}$  steps, starting from the time step when the examined tissue samples had at least 10 cells, we calculated the mitotic index as the ratio of cells that went through division to the total number of examined cells. Time evolutions of the mitotic

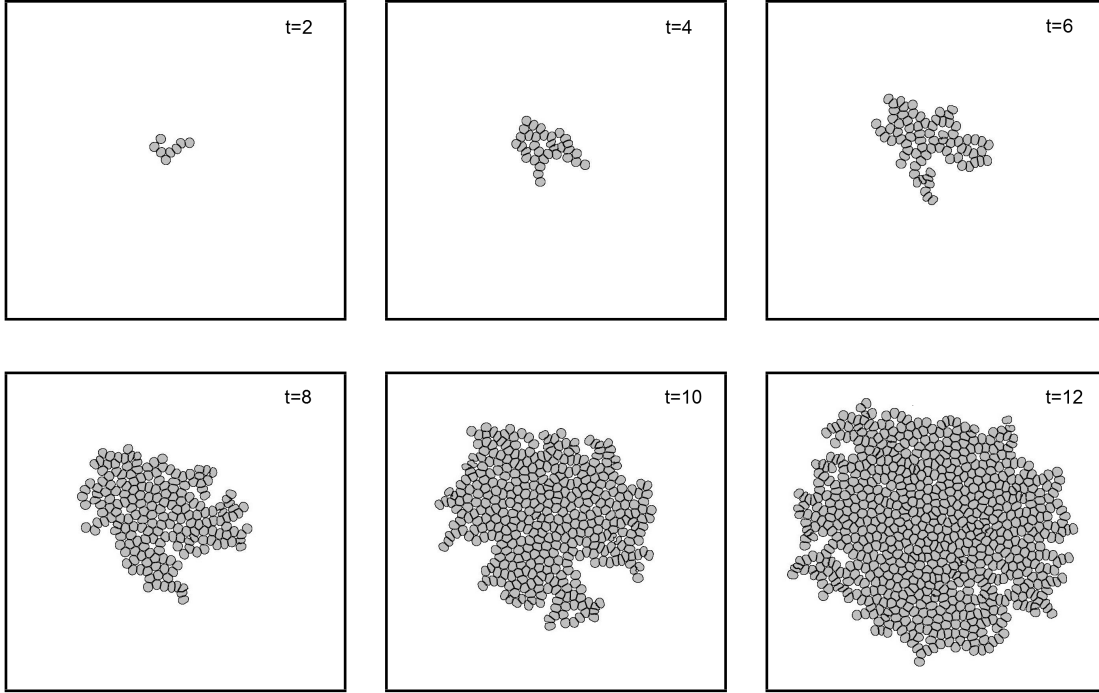


Figure 5.2: Snapshots of tissue growth in our model. Tissue starts its growth from a few cells which grow and divide through randomly oriented division planes. Snapshots show topological changes in tissue throughout simulation.

indices for all four simulation samples are shown in Figure 5.3 (blue points). Similar to the experimental procedure described by Wartlick *et al.* [83], data are averaged over simulation samples. The averaged data are then fitted to an exponential function using weighted least square fitting. We found that

$$f_{rand}(t) = 6.087 \exp(-0.2811t)$$

approximated the decay of simulated mitotic index ( $R^2 = 0.90$ ). Thus, the mitotic index of growing tissue in our model decays exponentially.

On average, the experimental value of the mitotic index of proliferating epithelium has a value of 1.7% [24]. To identify the proliferation regime as defined by experiments, we choose the time interval in our simulations, where simulated mitotic index has the value close to the experimentally observed one. For example, the vertical dashed lines in Figure 5.3 highlight the time interval that corresponds to the average mitotic index of 1.69% with standard deviation of 0.62%. We consider it to be the proliferation interval, or the interval of active growth state, for the model tissue.

We next examined the spatial distribution of mitotic cells. We sectioned the tissue



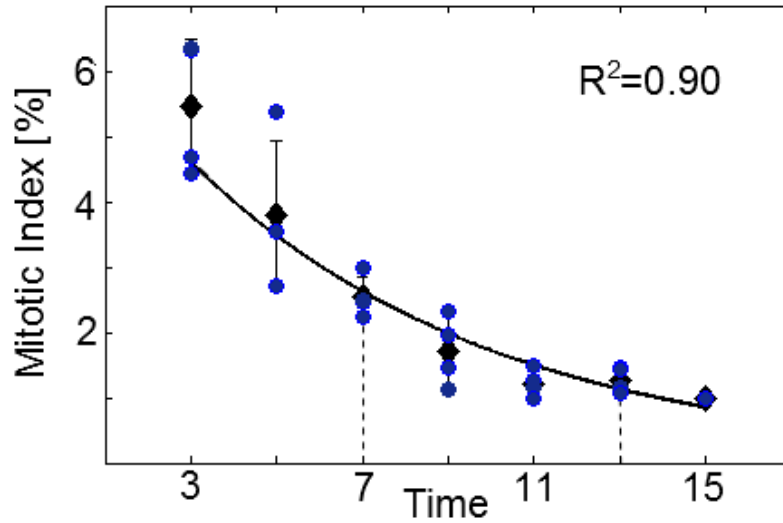


Figure 5.3: Time evolution of simulated mitotic index. Raw data are shown in blue. Similar to the experimental procedure described by Wartlick *et al.* [83] data are averaged over simulation samples (black points) and fitted to an exponential function (black curve). Dashed lines highlight the time intervals where average mitotic index has the value of  $1.69\%(\pm 0.62\%)$ .

into concentric rings, each with a thickness of  $0.1R_{max}$ . We then calculated the density of dividing cells in each ring. The time evolution of mitotic cell densities is shown in Figure 5.4. The time interval considered in Figure 5.4 corresponds to the proliferation regime. As we see from Figure 5.4, mitotic cells are found throughout the entire tissue. Divisions, however, are more frequent at the outer cell layers as seen on Figure 5.4. Therefore, on average, the distribution of dividing cells has a higher number of mitotic cells at the edges of tissue (Fig. 5.5).

## 5.2 Cell packing topology

Cell topology is characterised by the number of nearest neighbors. One can assign each cell a polygon type based on the number of its nearest neighbors. For instance, a cell with  $n$  nearest neighbors can be considered as an  $n$ -sided polygon. In this approximation, tissue is considered to be a polygonal network. In fact, cells in tightly connected tissues assume polygonal shapes, and representation of cells through polygons looks quite realistic. This resemblance serves as the basis for vertex models [28, 27]. Stable configurations of the epithelial junctional network throughout its proliferation, and

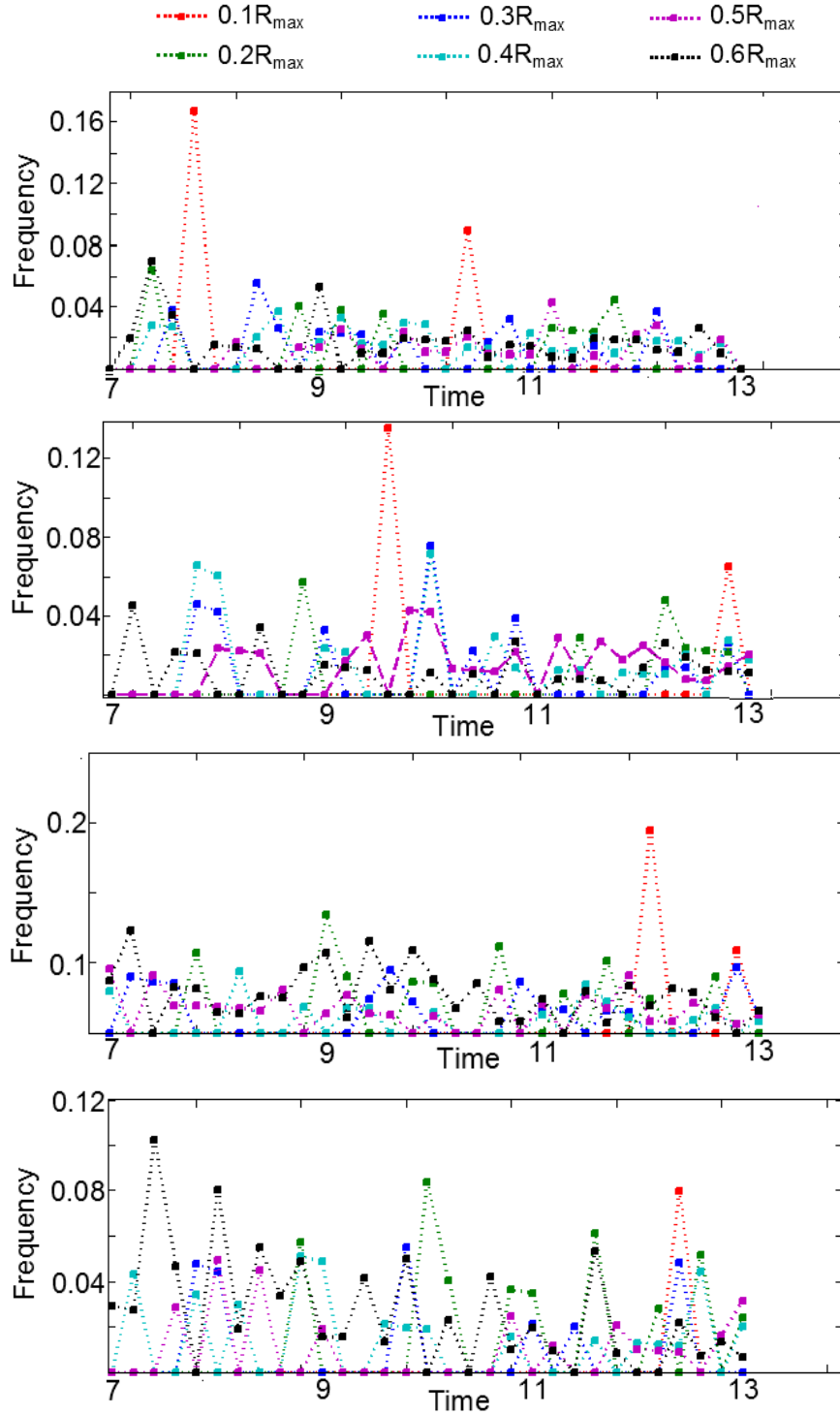


Figure 5.4: Spatial distribution of mitotic cells for proliferation time interval. In all four simulation samples mitotic cells are found throughout the entire tissue.

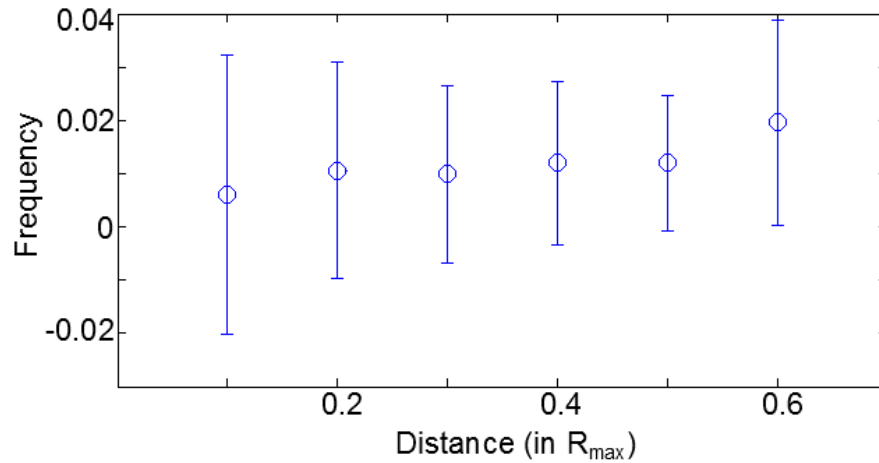


Figure 5.5: Spatial distribution of mitotic indices averaged over the proliferation time interval and simulation samples.

the ability to incorporate cell mechanics and proliferation into the vertex models make them attractive choice for studying tissue topology. However, cellular shapes are less realistic in these models.

We start to grow the tissue from several cells and follow the evolution of cell packing topologies. During tissue growth, cells assume polygonal shapes in our model (Fig. 5.6 (*Left*)), but, in contrast to vertex models, cell polygonal shapes arise naturally. To characterize cell polygon types in our model, we determine centers of mass of all

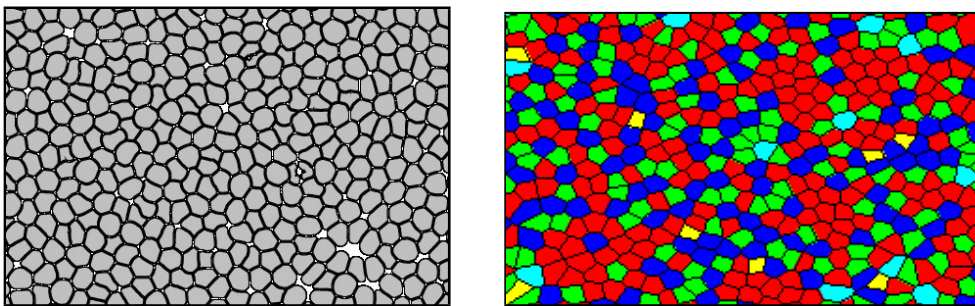


Figure 5.6: Two examples of cells in tissue at the end of two separate simulations. *Left*: Snapshot of a simulated tissue. *Right*: Cells shown as polygons through Voronoi diagram. Different colours indicate different polygon types. Pentagons, hexagons and heptagons are coloured as green, red and blue, correspondingly. Different polygons arise naturally due to cell-cell interactions.

cells and use them to construct a Voronoi diagram of the tissue (see Sect. 3.2.5). Figure 5.6 (*Right*) shows an example.

We calculated the fraction of  $n$ -sided polygons and recorded cell topology distribution every 500 time steps. The time evolution of cell polygonal types is shown in Figure 5.7. Cell polygon types change dramatically at the early stages of tissue development. After about 25 division cycles, the distribution of polygons stabilizes. As we can see from Figure 5.7, most of the cells assume shapes of 4- to 8-sided polygons, but small fractions of 3- and 9-sided polygons also exist (not shown on the graph). We found them to be less than 1%. Hexagonal shapes are the most frequent, followed by pentagons and heptagons as the next frequent shapes.

To compare the polygon distribution with that of experimentally observed *Drosophila* wing disc topology [19], we estimate the average number of cell polygon types during the proliferation regime. Proliferation time intervals for each simulation sample are calculated based on the mitotic index as described in the previous section. They are highlighted with the dashed vertical lines in Fig. 5.7. Figure 5.8 displays the simulated distribution cell polygonal shapes during proliferation, averaged over four samples. For comparison, the polygon distribution in proliferating *Drosophila* wing disc [19] is presented as well. Numerical values of cell polygon type frequencies for both simulations and experiments can be found in Table 5.1.

Table 5.1: Comparison of simulated and experimental fractions of cell polygon types

|             | Tetragons       | Pentagons        | Hexagons         | Heptagons        | Octagons        |
|-------------|-----------------|------------------|------------------|------------------|-----------------|
| Simulation  | $1.9 \pm 0.7\%$ | $27.6 \pm 2.1\%$ | $47.9 \pm 3.0\%$ | $20.1 \pm 1.9\%$ | $2.4 \pm 0.8\%$ |
| Experiments | $2.8 \pm 1.6\%$ | $27.2 \pm 1.8\%$ | $45.8 \pm 2.4\%$ | $20.3 \pm 2.5\%$ | 1.15%           |

As we can see, our model captures the main characteristics of experimentally observed tissue topology. The distribution has a peak for hexagonal cells and an asymmetric distribution of pentagons and heptagons. Numerical values are in good agreement with *Drosophila* wing topology.

### 5.3 Summary

Epithelial sheets are often used as a model system for studies of tissue growth and morphogenesis due to their simplicity. In particular, tissue proliferation has been extensively studied on epithelium of *Drosophila* fruit fly wing imaginal disc. Several features of proliferating epithelium include spatial homogeneity of growth, relatively constant fraction of cells in mitotic stage and the characteristic tissue topology [138, 24, 19].

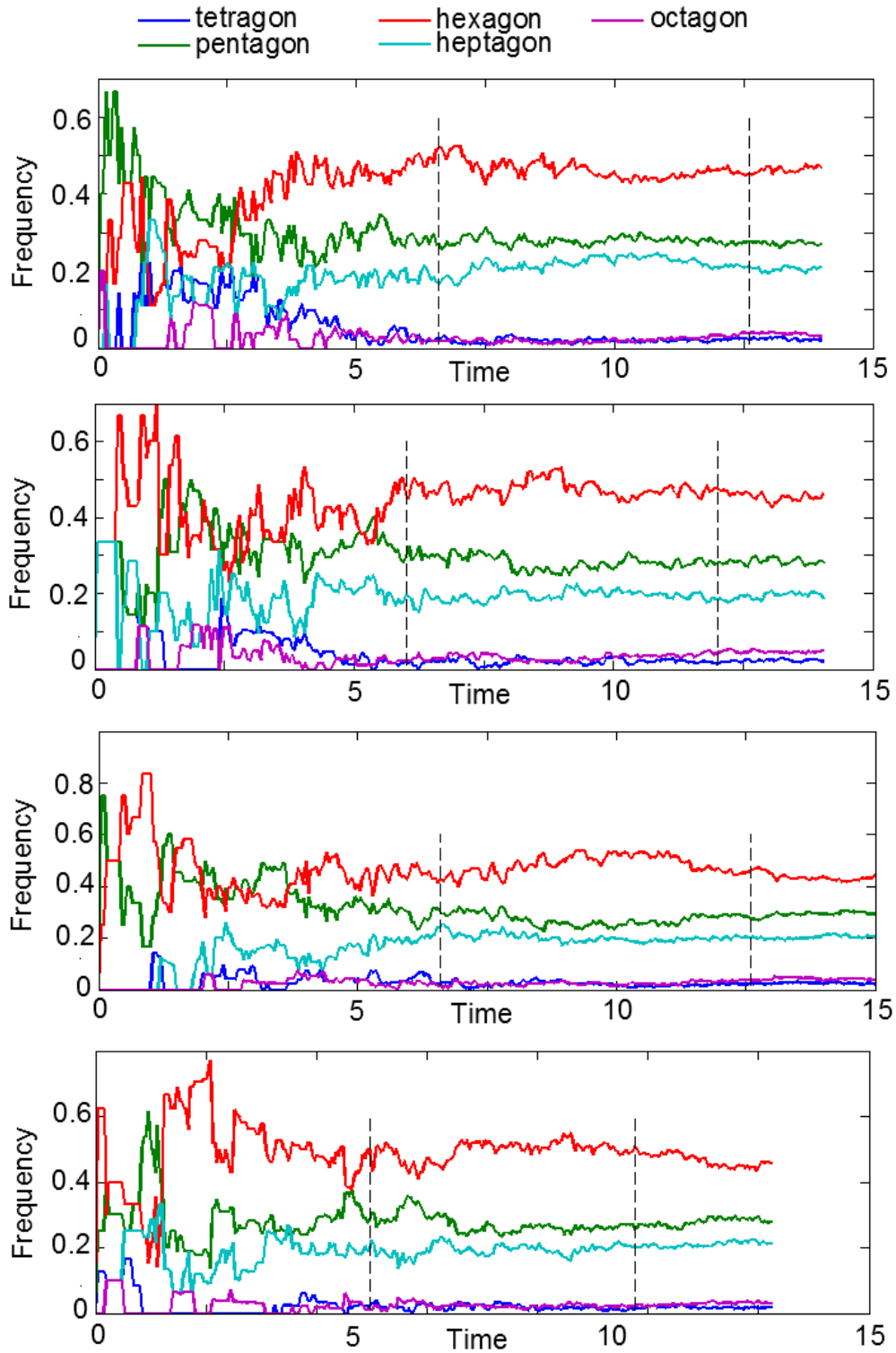


Figure 5.7: Time evolution of the polygon type distribution for four simulation samples. Blue dashed lines indicate the proliferation time intervals for each sample.

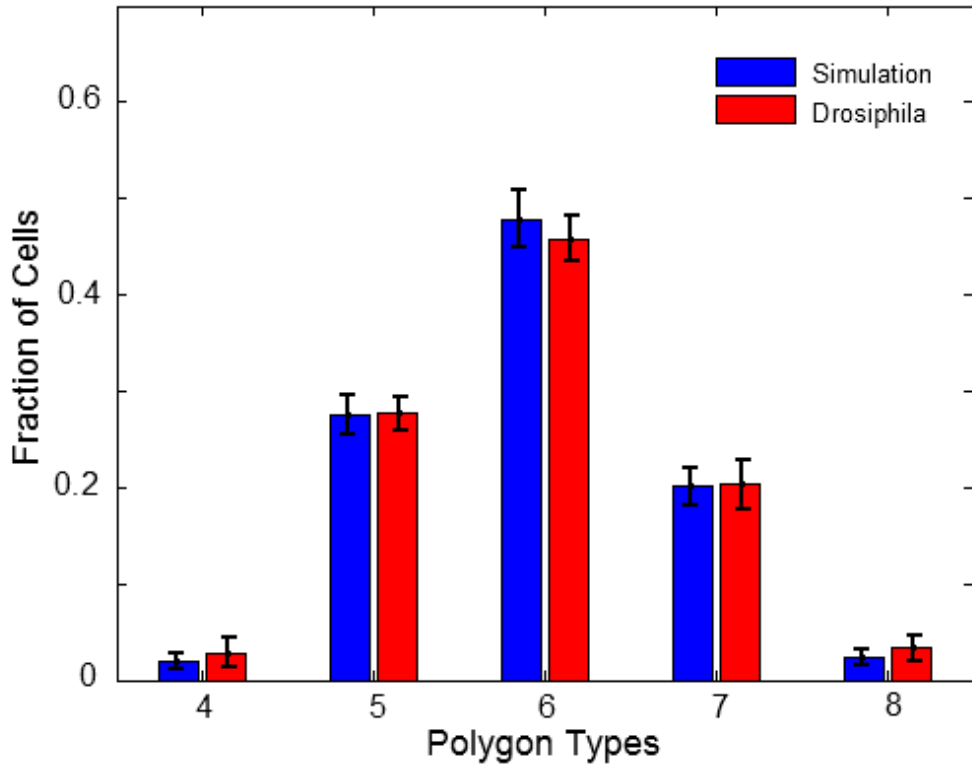


Figure 5.8: Polygon type distribution compared with experimentally observed topology of *Drosophila* wing epithelium topology. Simulation data are averaged for four samples. Error bars indicate the standard deviation over all four samples. Experimental data are taken from the work by Gibson *et al.* [19].

We examined the growth and the cellular packing topologies of proliferating tissue using the new mechanical model developed in this thesis (Chapt. 4). Time evolution of the mitotic index and the cell packing topologies in our model were compared with the experimentally obtained mitotic index and the topology of proliferating *Drosophila* wing disc [83, 19].

The mitotic index in simulated tissue decreases exponentially, similar to the experiments [83]. Dividing cells are found throughout the entire simulated tissue. It is, however, more likely to find mitotic cells closer to the tissue edges. Therefore, the density of dividing cells is higher at outer layers of tissue.

Several hypothesis have been suggested to explain tissue growth control [18]. Among them is the mechanical model for regulation of tissue growth [87]. According to the model proposed by Aegerter-Wilmsen *et al.* [87], peripheral regions of *Drosophila* wing disc compress its center, which inhibits the growth at the center. The larger size of the

disk leads to stronger compression, and that eventually ceases the growth. We believe that the decay of the mitotic index in our model is determined by the same mechanism. The growth rate of cells is defined by the growth rate of internal pressure assigned to each cell. Currently, we keep the growth rate of the internal pressure constant throughout the simulation, but as the tissue grows larger, the compression inside the tissue defined by the internal pressure grows as well. Increase in the compression gradually decreases the number of dividing cells, until the growth stops completely. That also explains the higher number of mitotic cells further from the tissue center.

Finally, we compared cellular packing in proliferating model tissue with the characteristic epithelial topology. Cellular packing topologies in our simulations are in a good agreement with experimentally observed epithelial packing topologies.

We conclude that our model can account for the main attributes of the epithelial growth, such as the time evolution of the mitotic index and the cell packing topologies.

## Chapter 6

# The Influence of Division Plane and Cellular Rearrangements on Cell Packing Topologies

Cell divisions are among the processes that alter tissue topology during its formation. In the previous chapter, we explored tissue growth and cell packing topologies when cells divide through randomly oriented symmetric division planes. In this chapter, we examine proliferation through two alternative biologically relevant division schemes. First, we consider division with a randomly oriented asymmetric division planes, which is an essential part of the cell differentiation process [69]. When a parental cell divides asymmetrically, two daughters may differ in cellular content or size, and consequently inherit different fates [2]. In this work we consider asymmetric divisions that generate daughter cells of different sizes. Another division plane of biological importance, which we consider here, is the division plane defined by the cell's geometry. Initially described by Hertwig in 1893, division based on the 'longest axis rule' or Hertwig's rule is influenced by the geometry of the cell: the cell division plane is directed along the line perpendicular to the cell's longest axis. In Section 6.1, we discuss tissue growth through asymmetric and Hertwig's division planes and compare results with the case of the random division scheme discussed in the previous chapter.

One of the benefits of single cell based models is the ability to account for cell rearrangements. As we discussed in Section 4.1.2, such rearrangements in our model are influenced by viscous damping. In Section 6.2 we examine the effects of rearrangements, influenced by viscous damping, on the tissue topology.



## 6.1 The effect of asymmetric division and division by Hertwig's rule on tissue topology

To analyse the impact of the division plane on tissue growth and topology, we grow tissues starting from a few cells, where each cell divides based on a specific division scheme. We first consider the asymmetric division scheme. The asymmetric division plane is chosen such that it has a random orientation and divides the cell into two unequal parts with areas  $A^{large}$  and  $A^{small}$ . We presented a general algorithm for construction of an asymmetric division plane in Section 4.1.3. Here, we choose the asymmetric division plane such that the ratio of  $A^{small}$  to  $A^{large}$  is roughly 0.5 for all instances of cell divisions. Instantaneous values of  $A^{small}/A^{large}$  ratio throughout the entire simulation are presented in Figure 6.1. On average, the ratio is about 0.45 with a standard

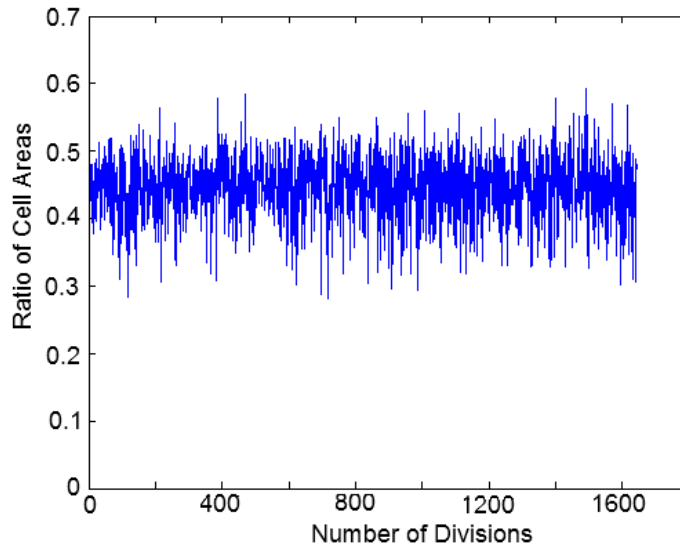


Figure 6.1: The ratio of small and large cell areas during the asymmetric division. On average, the larger cell is twice as big as the smaller cell.

deviation of 0.05. Thus, the larger cell is roughly twice as big as the smaller cell.

The second division scheme we consider is division by Hertwig's rule [12]. The division plane is chosen perpendicular to the cell's longest axis as described in Section 4.1.3.

Figures 6.2 and 6.3 show snapshots of tissue development for both division schemes.

Snapshots of tissue proliferating through random division planes were presented in Figure 5.2.

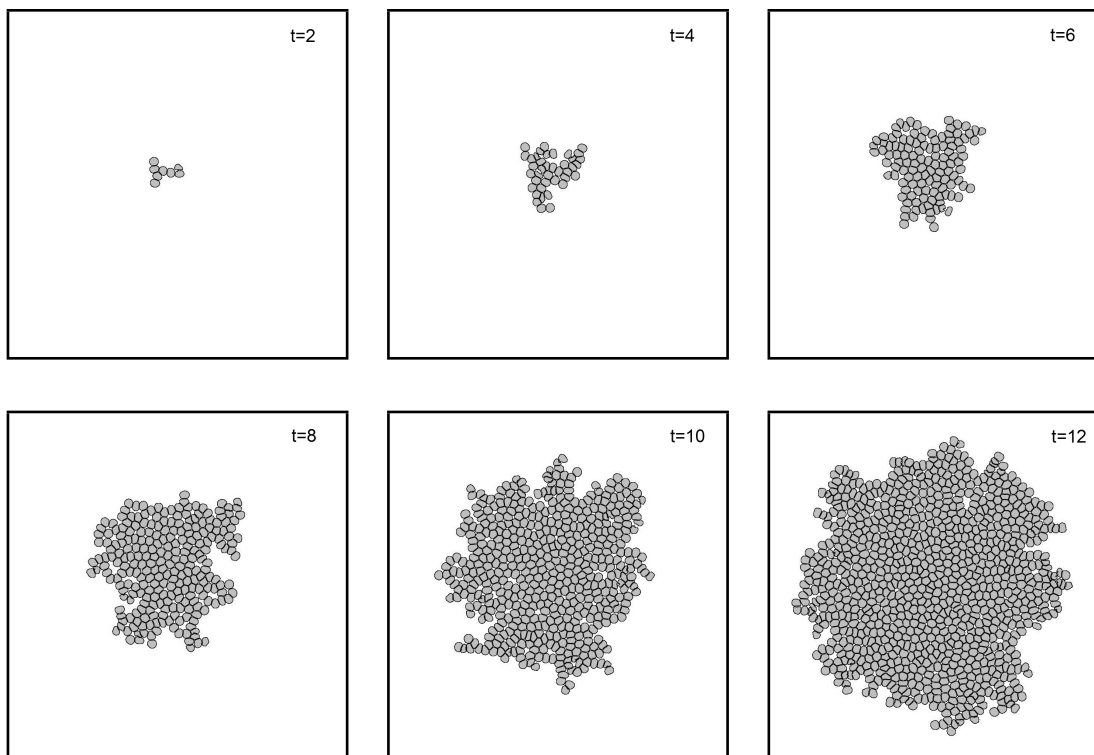


Figure 6.2: Snapshots from a simulation of tissue growth through asymmetric cell division.

To further investigate the impact of division planes on tissue proliferation, we examine the time evolutions of mitotic indices for asymmetric and Hertwig's division schemes (shown in Figs. 6.4 and 6.5), and compare them to the mitotic index of tissue growth through the random division scheme (Fig. 5.3).

Mitotic indices for both random (Fig. 5.3) and asymmetric (Fig. 6.4) division planes behave similarly. In both cases, mitotic indices are fitted to exponential functions of similar forms, using weighted least-squares fitting. The exponential fit to the mitotic index of the random division scheme is found to be

$$f_{rand}(t) = 6.087 \exp(-0.2811t)$$

with  $R^2 = 0.90$ , while the exponential fit to the mitotic index of the asymmetric division scheme is

$$f_{asymm}(t) = 3.349 \exp(-0.213t)$$

with  $R^2 = 0.75$ .

The time evolution of the mitotic index for division based on Hertwig's rule differs

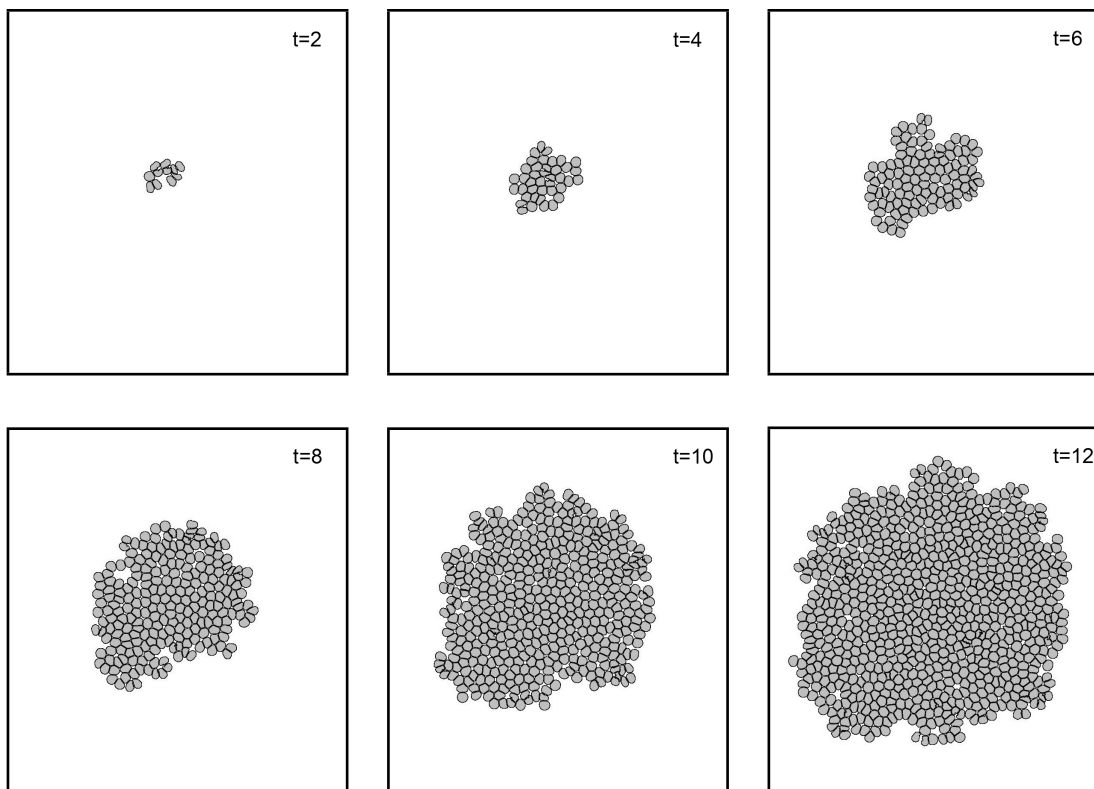


Figure 6.3: Snapshots from a simulation of tissue growth through Hertwig's division rule.

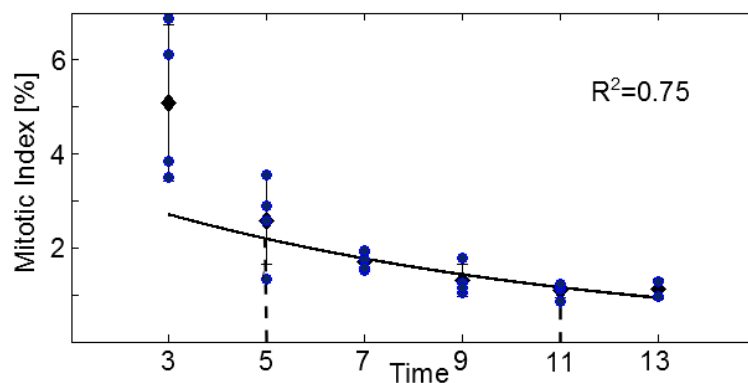


Figure 6.4: Mitotic index for asymmetric division plane. Raw data are shown in blue. Similar to the experimental procedure described by Wartlick *et al.* data are averaged over simulation samples (black points) and fitted to an exponential function (black curve) [83]. Dashed lines highlight time intervals where the average mitotic index has the value of 1.67% with a standard deviation of 0.74%.

from that of the division schemes mentioned above. The mitotic index decreases rapidly at the early stages of the growth. We were unable to find a single exponential fit to data

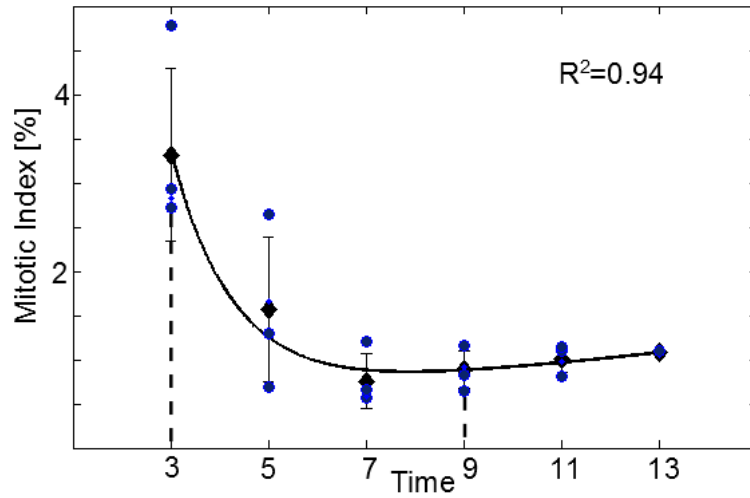


Figure 6.5: Mitotic index for longest axis division plane. Raw data are shown in blue. Similar to the experimental procedure described by Wartlick *et al.* [83] data are averaged over simulation samples (black points) and fitted to the sum of two exponential functions (black curve). Dashed lines highlight time intervals where average mitotic index has the value of  $1.63\%(\pm 1.21\%)$ .

points, so we approximated mitotic index with the sum of two exponential functions, namely

$$f_{hertwig}(t) = 13.4 \exp(-1.581t) + 0.54 \exp(0.115t)$$

with  $R^2 = 0.94$ . For comparison, all three mitotic indices are presented in Figure 6.6 .

Figure 6.6 shows that the mitotic index for Hertwig's division scheme is consistently lower compared to that for random symmetric or asymmetric division schemes, suggesting slower growth in the former case. Hertwig's division rule is based on cellular geometry. Division perpendicular to cell's longest axis generates more compact daughter cells and favours optimal cellular packing. In optimally packed tissues the growth of central cells is suppressed by the surrounding cells, resulting in a lower mitotic index.

We further examine cell packing topologies for asymmetric and Hertwig's division planes and compare them with the packing topologies for the random division scheme. We first identify time intervals where average mitotic indices are close to the experimental value of 1.7% (highlighted with dashed lines in Figs. 6.4, 6.5 and 5.3 correspondingly). As in the case of the random division plane, we follow the time evolution of cell polygonal types and collect statistics for the time intervals that correspond to proliferation. The time evolution of cell polygonal shapes generated by asymmetric

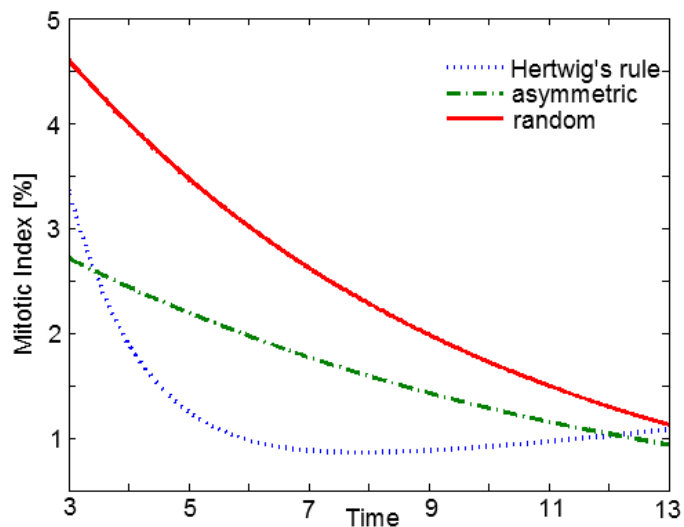


Figure 6.6: Functions fitted to mitotic indices for three division schemes: random (red), asymmetric (green) and Hertwig's rule (blue).

and orthogonal division schemes are shown in Figures 6.7 and 6.8 .

Average fractions of different polygons are then calculated over proliferation time intervals for four simulation samples. Although averaging does not reflect the dynamics of topology, it allows us to compare the distribution of cell shapes for various division schemes. Polygon type distributions for random, asymmetric and Hertwig's division schemes, along with the experimentally observed topology of fruit fly wing disc, are presented in Figure 6.9. Numerical values of cell polygon types are presented in Table 6.1.

Table 6.1: Comparison of fractions of cell polygon types for random, asymmetric and Hertwig's division schemes.

|               | Tetragons        | Pentagons        | Hexagons         | Heptagons        | Octagons          |
|---------------|------------------|------------------|------------------|------------------|-------------------|
| Random        | $1.9 \pm 0.7\%$  | $27.6 \pm 2.1\%$ | $47.9 \pm 3.0\%$ | $20.1 \pm 1.9\%$ | $2.4 \pm 0.8\%$   |
| Asymmetric    | $2.8 \pm 1.5\%$  | $27.8 \pm 3.4\%$ | $46.9 \pm 5.3\%$ | $19.7 \pm 2.4\%$ | $2.6\% \pm 1.2\%$ |
| Herwig's rule | $1.1 \pm 1.22\%$ | $26.7 \pm 3.3\%$ | $52.3 \pm 5.8\%$ | $18.5 \pm 3.8\%$ | $1.3\% \pm 1.2\%$ |
| Experiments   | $2.8 \pm 1.6\%$  | $27.2 \pm 1.8\%$ | $45.8 \pm 2.4\%$ | $20.3 \pm 2.5\%$ | 1.15%             |

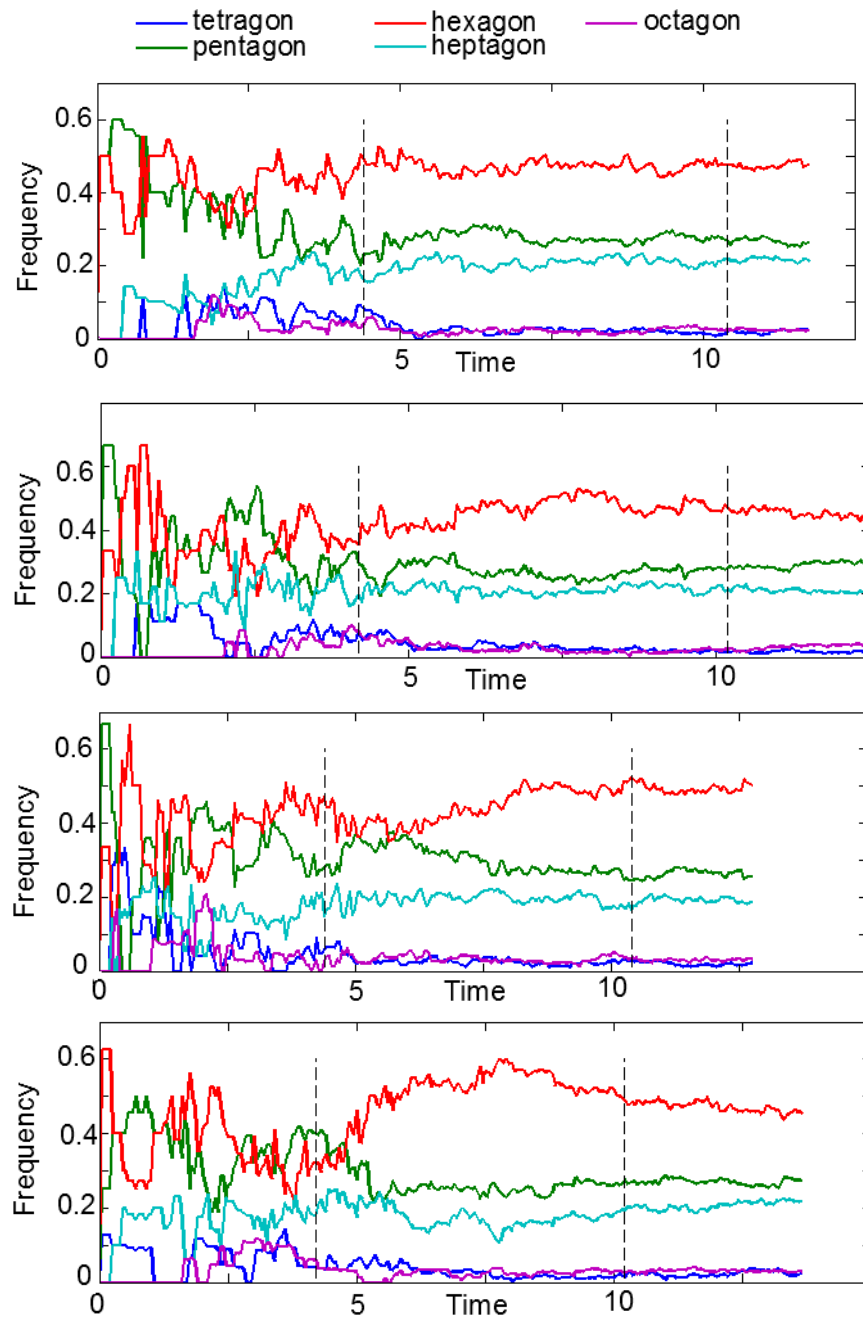


Figure 6.7: Time evolution of the polygon type distribution for the asymmetric division scheme. Blue dashed lines indicate the proliferation time intervals for each sample.

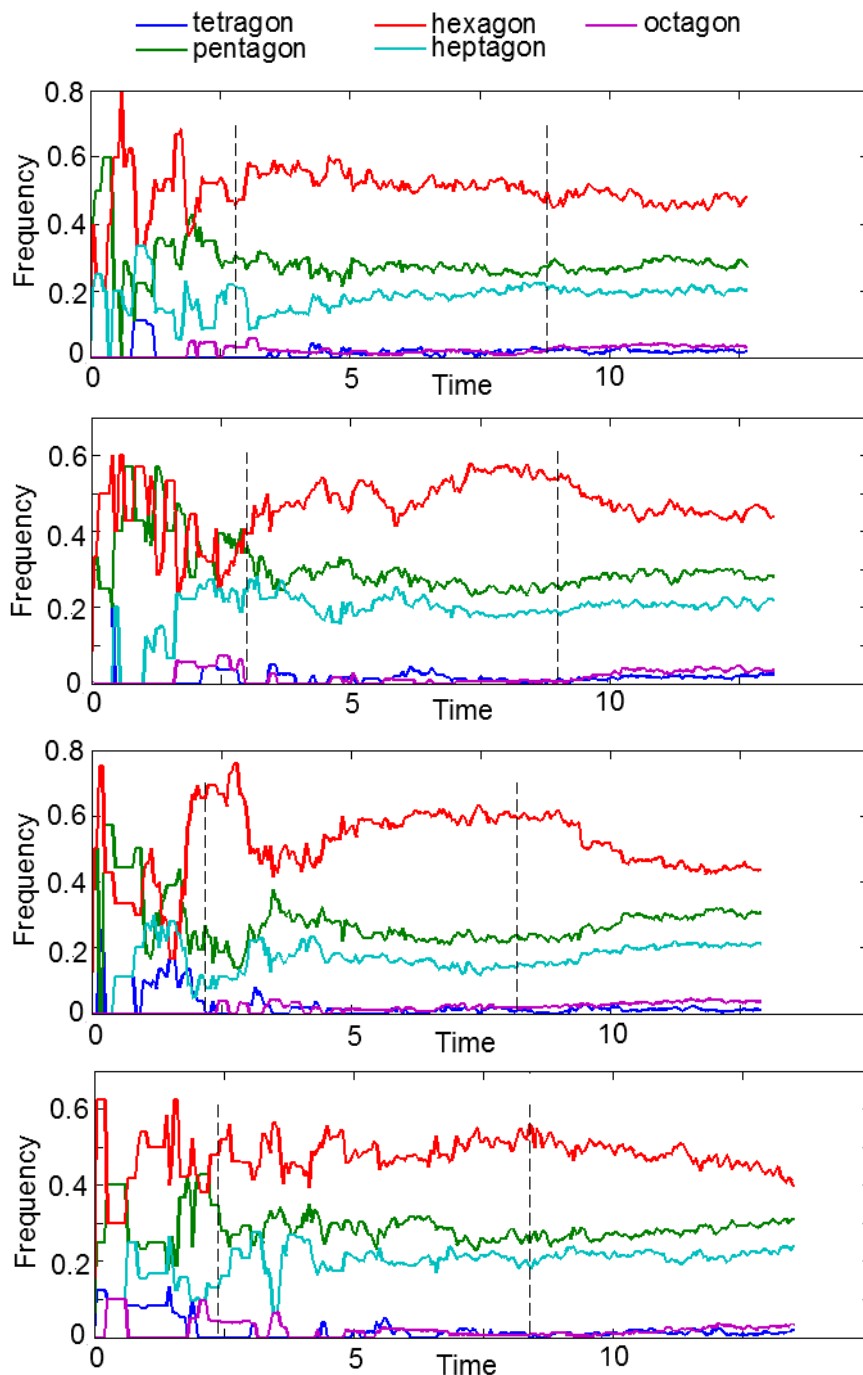


Figure 6.8: Time evolution of the polygon type distribution for Hertwig's division scheme. Blue dashed lines indicate the proliferation time intervals for each sample.

## 6.2 The effect of cellular rearrangements influenced by viscous damping on tissue topology

As we discussed in Section 4.1.2, the extent of cellular rearrangements due to cellular movements along each other is controlled by viscous damping. Damping is defined

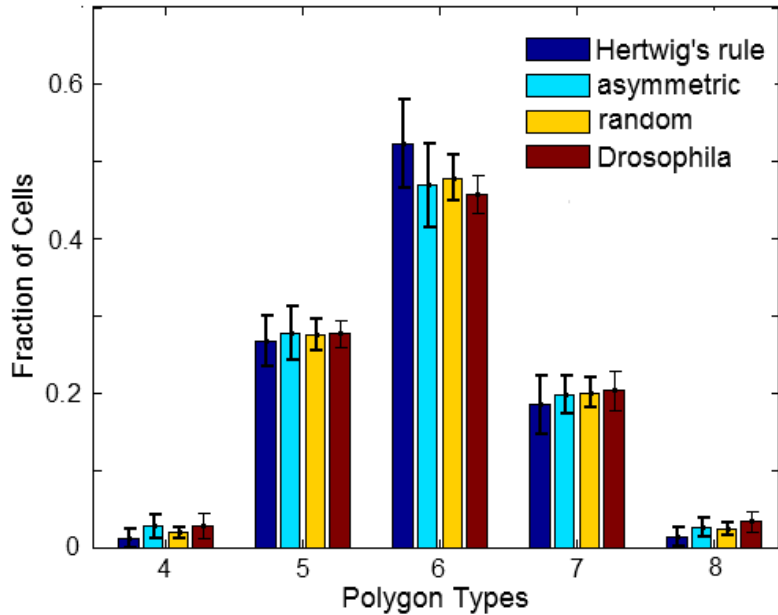


Figure 6.9: Cell polygon type distributions for three division schemes: Hertwig's, asymmetric and random. For comparison, distribution of cellular polygons in *Drosophila* wing is presented as well. All three cases lead to the characteristic distribution for proliferating epithelium.

by the coefficient  $\gamma$ , which is a free parameter in our model (see Sect. 4.1.2). During calibration, we found that a damping coefficient  $\gamma = 20$  leads to cell packing of proliferating tissue similar to those of observed experimentally in epithelium (Fig. 5.8).

In this section we consider two other growth mechanisms, with lower damping coefficients  $\gamma = 10$  and  $\gamma = 0$ . A damping coefficient  $\gamma = 10$  only partially restricts cellular rearrangements, whereas in the case of  $\gamma = 0$  cells are free to move along each other. Figures 6.10 and 6.11 show snapshots of tissue development for  $\gamma = 10$  and  $\gamma = 0$ , correspondingly.



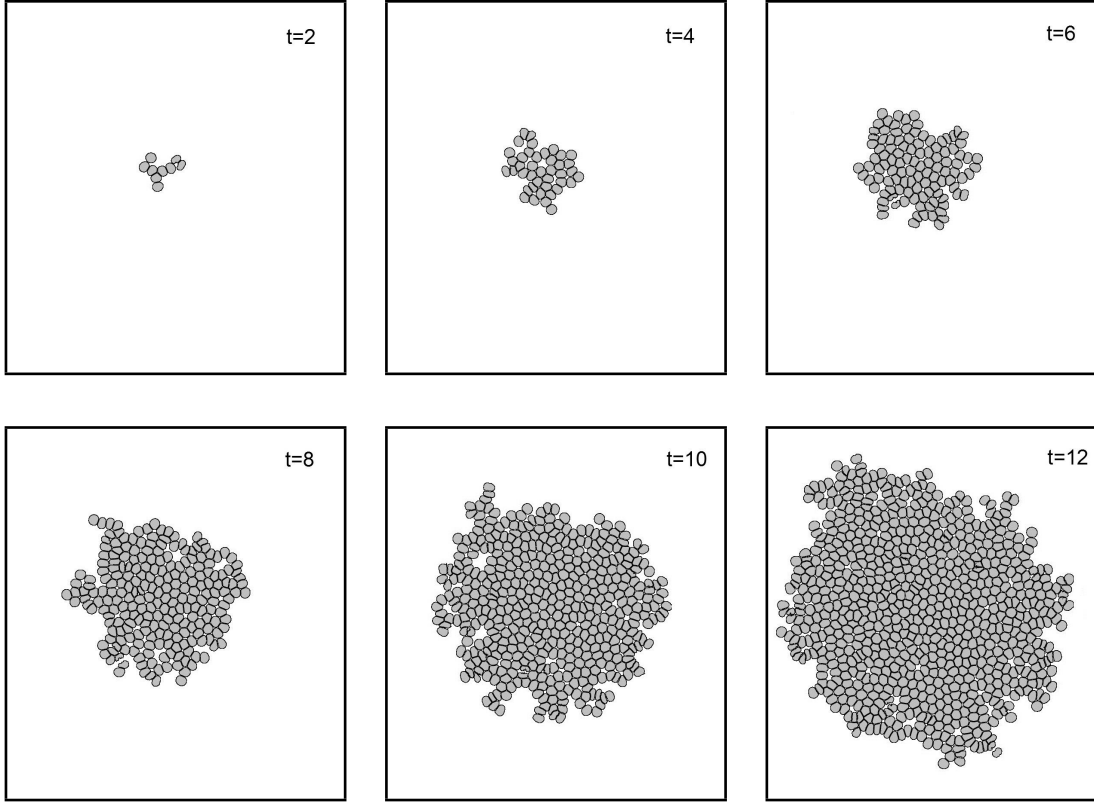


Figure 6.10: Snapshots of simulated tissue growth for damping coefficient  $\gamma = 10$ .

Visual inspection of the snapshots reveals that during tissue growth with free cellular rearrangements (the  $\gamma = 0$  case), cells are packed in more ordered structures. Indeed, Figure 5.6 shows snapshots of simulated tissues with three different values of  $\gamma$  parameter. All three systems had the same initial conditions and the three snapshots were taken at the same time. As Figure 6.12 shows,  $\gamma = 0$  leads to more ordered packing than does  $\gamma = 20$ .

To understand the differences in tissue growth and cell packing topologies for the three different damping coefficients, we consider the time evolution of mitotic indices for those three cases (see Figs. 6.13, 6.14 and 5.3).

To estimate time dependency of mitotic indices, data points are averaged over simulation samples and are fitted to exponential functions. The  $\gamma = 10$  case is fitted to

$$f_{\gamma=10}(t) = 12.23 \exp(-0.809t) + 0.2041 \exp(-0.6302t)$$

with  $R^2 = 0.98$  and the  $\gamma = 0$  case is fitted to

$$f_{\gamma=0} = 12.3 \exp(-1.013t)$$

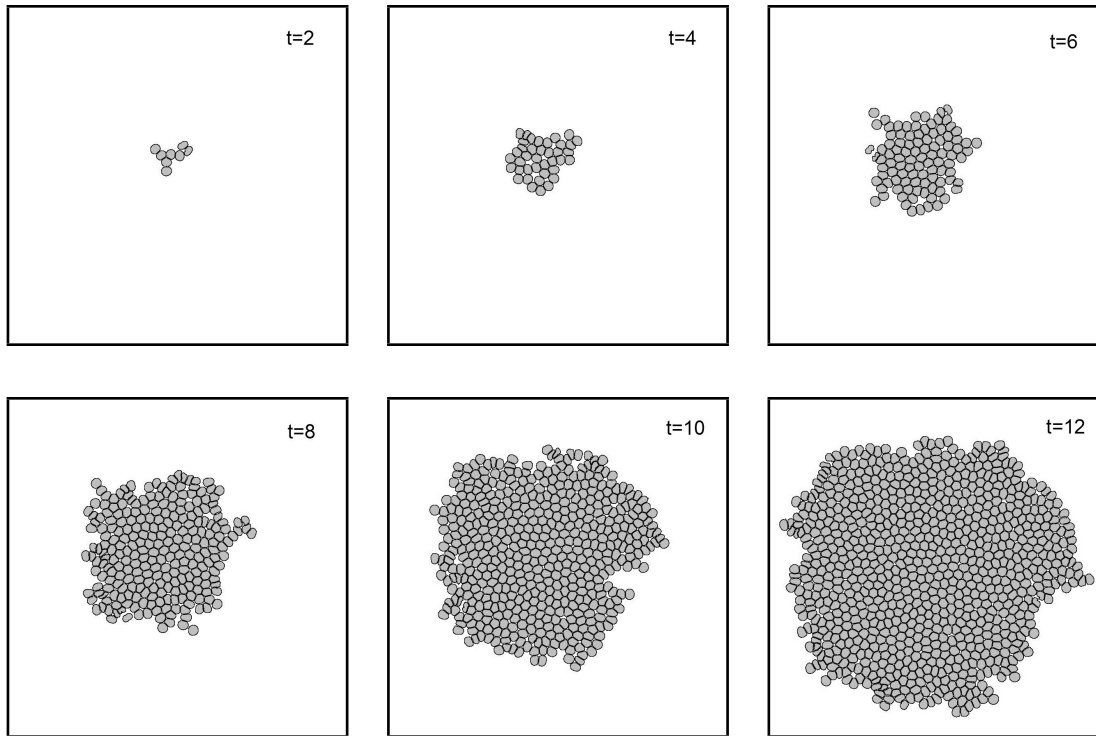


Figure 6.11: Snapshots of simulated tissue growth for damping coefficient  $\gamma = 0$ .

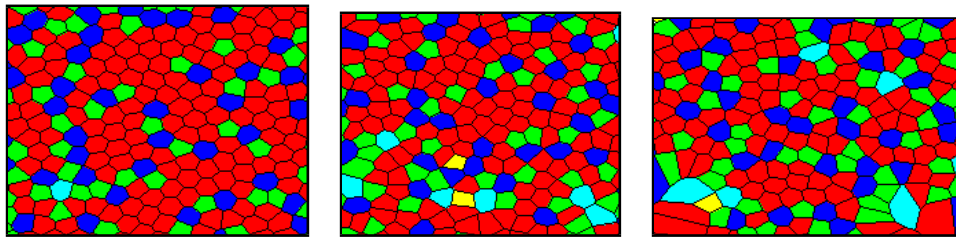


Figure 6.12: Snapshots of the Voronoi diagrams of the tissue for three different scenarios of cellular rearrangements. Cell polygon types coloured as green for pentagons, red for hexagons and blue for heptagons correspondingly. *Left to Right*:  $\gamma = 0$ ,  $\gamma = 10$ ,  $\gamma = 20$ . For the  $\gamma = 0$  case, cellular rearrangements are not suppressed. Cellular packing is shifted towards hexagons, compared to the  $\gamma = 10$  and  $\gamma = 20$  cases, where the amount of cellular rearrangements is restricted. All snapshots are taken at the same time with the same initial condition.

with  $R^2 = 0.95$ . In comparison with the  $\gamma = 20$  case, mitotic indices of both the  $\gamma = 10$  and  $\gamma = 0$  cases decrease faster (Fig. 6.15).

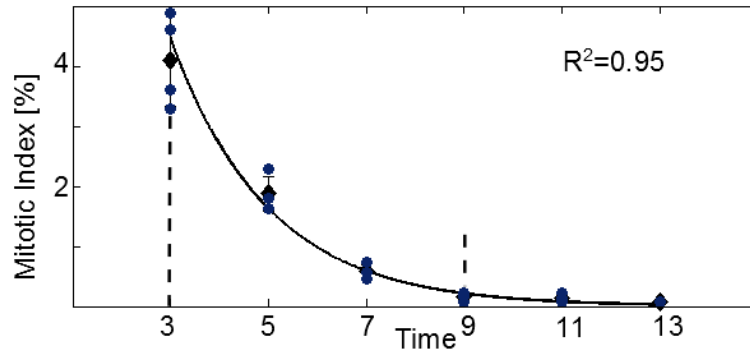


Figure 6.13: Mitotic index for the case of unrestricted cellular rearrangements defined by the absence of viscous damping  $\gamma = 0$ . Raw data are shown in blue. Data are averaged over simulation samples (black points) and fitted to the exponential (black curve). Dashed lines highlight time intervals where the average mitotic index has the value of 1.69% with a standard deviation of 1.63%.

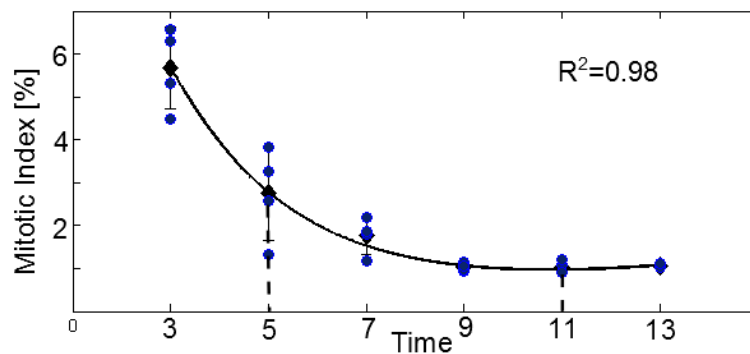


Figure 6.14: Mitotic index for the case of cellular rearrangements defined by viscous damping with the coefficient  $\gamma = 10$ . Raw data are shown in blue. Data are averaged over simulation samples (black points) and fitted to the sum of two exponential functions (black curve). Dashed lines highlight time intervals where the average mitotic index has the value of 1.63% with a standard deviation of 0.90%.

As Figure 6.15 shows, tissue growth with less restricted cellular rearrangements displays a more rapid decrease of mitotic index. The overall decrease in mitotic index results in more ordered packing of cells in tissues (see Figs 6.16 and 6.17).

Next, we identify proliferation time intervals and compare cell packing topologies of proliferation tissues for the cases of  $\gamma = 0$ ,  $\gamma = 10$  and  $\gamma = 20$ . The average distributions of polygonal cells for all three simulations as well as the packing topology in *Drosophila* wing discs are shown in Figure 6.18. Numerical values of cell polygon type frequencies are presented in Table 6.2. All three cases reproduce the characteristic

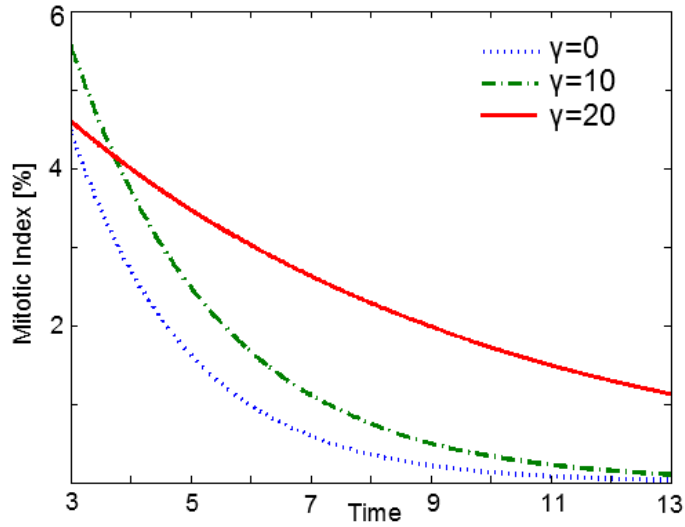


Figure 6.15: Functions fitted to mitotic indices for three various amounts of cellular rearrangements defined by the viscous damping coefficient  $\gamma$ .

Table 6.2: Comparison of fractions of cell polygon types for cellular rearrangements defined by viscous damping with  $\gamma = 20$ ,  $\gamma = 10$  and  $\gamma = 0$ .

|               | Tetragons       | Pentagons        | Hexagons         | Heptagons        | Octagons          |
|---------------|-----------------|------------------|------------------|------------------|-------------------|
| $\gamma = 20$ | $1.9 \pm 0.7\%$ | $27.6 \pm 2.1\%$ | $47.9 \pm 3.0\%$ | $20.1 \pm 1.9\%$ | $2.4 \pm 0.8\%$   |
| $\gamma = 10$ | $2.3 \pm 1.4\%$ | $25.3 \pm 2.6\%$ | $51.3 \pm 3.7\%$ | $18.7 \pm 2.1\%$ | $1.8\% \pm 0.9\%$ |
| $\gamma = 0$  | $1.7 \pm 1.8\%$ | $23.7 \pm 4.6\%$ | $57.4 \pm 8.0\%$ | $16.3 \pm 3.4\%$ | $0.8\% \pm 1.1\%$ |
| Experiments   | $2.8 \pm 1.6\%$ | $27.2 \pm 1.8\%$ | $45.8 \pm 2.4\%$ | $20.3 \pm 2.5\%$ | 1.15%             |

distribution, however, growth accompanied with free cellular rearrangements displays more optimally packed topologies. Unrestricted cellular rearrangements drive the packing of cells towards the optimal configuration at the initial stages of proliferation. The growth of the central part of the tissue is then restricted by surrounding cells, and overall tissue growth is quickly ceased.

### 6.3 Summary

In this chapter we considered the influence of two factors on proliferating tissue topology: the choice of the division plane, and the amount of cellular rearrangement defined by viscous damping.

We first considered cell packing topologies for various division planes. We found

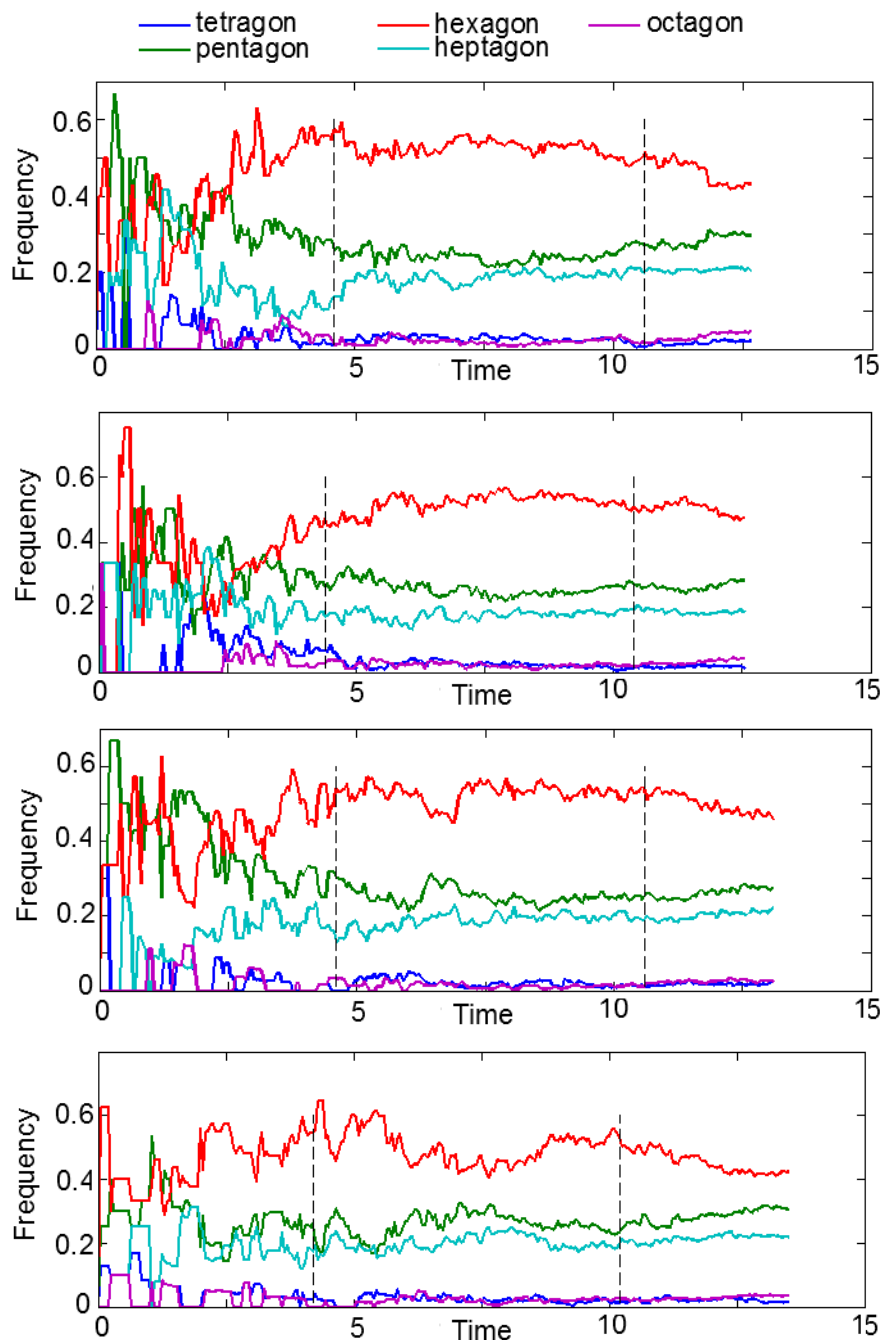


Figure 6.16: Time evolution of the polygon type distribution for the  $\gamma = 10$  case. Blue dashed lines indicate the proliferation time intervals for each sample.

that randomly oriented symmetric and asymmetric division planes lead to similar dynamics of tissue growth and cellular packing in proliferating tissue. Hence, the differences in sizes of daughter cells do not alter cell packing topology significantly. Cell packing topologies in tissues are influenced by cell mechanics [73, 26, 27]. Cell divi-

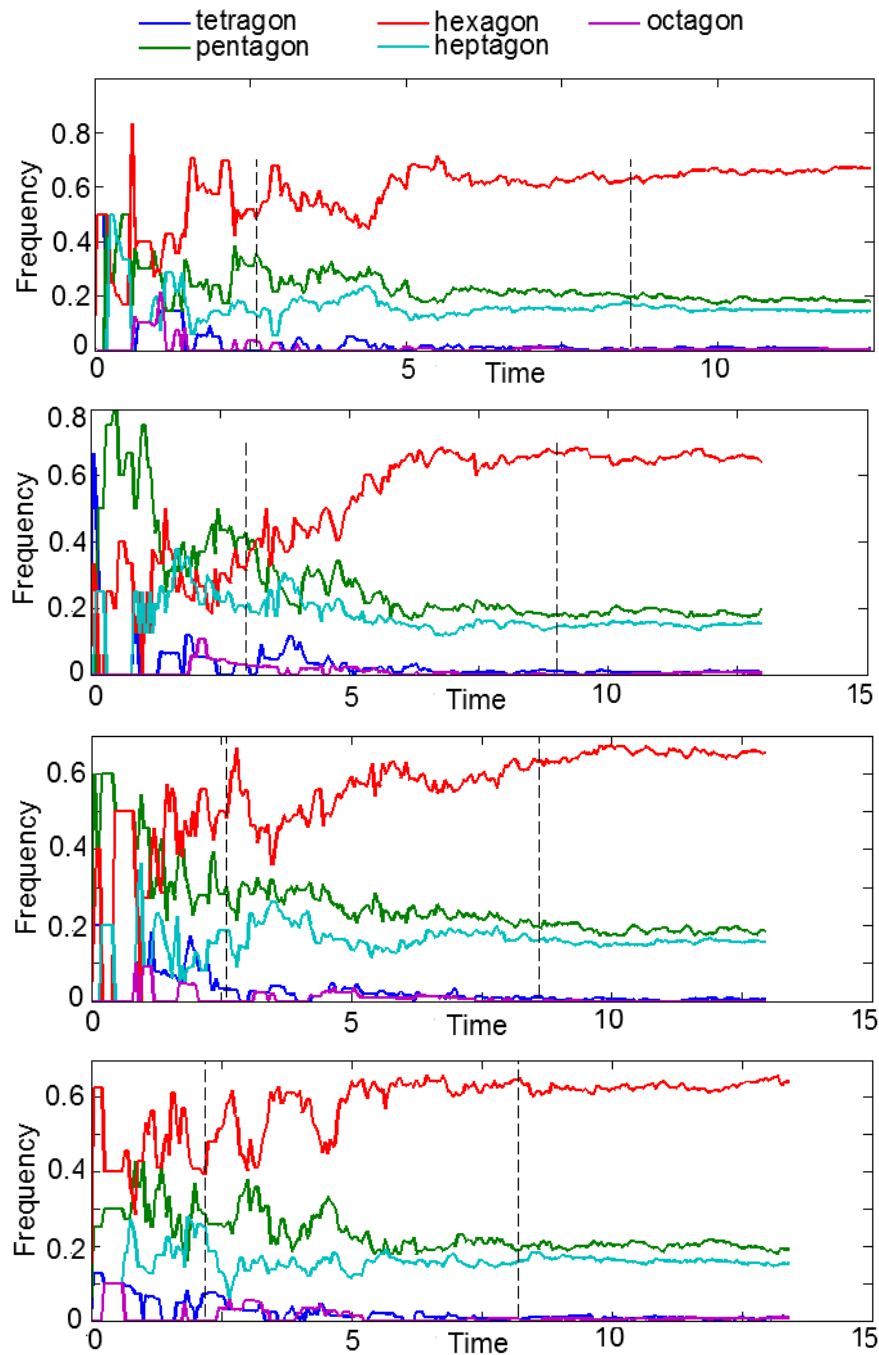


Figure 6.17: Time evolution of the polygon type distribution for the  $\gamma = 0$  case. Blue dashed lines indicate the proliferation time intervals for each sample.

sion introduces an imbalance in forces acting on mass points. Imbalance in net forces defines changes in cell shapes and topologies, and drives tissue towards its equilibrium state. Since during cell division, both daughter cells are assigned the same physical

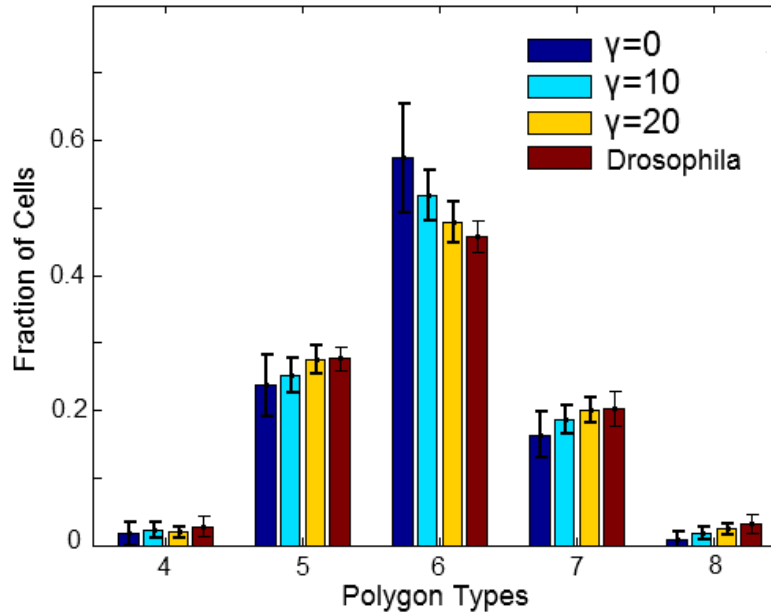


Figure 6.18: Polygon type distribution for various amount of cell rearrangements. All three cases reproduce characteristic distribution of polygon types in proliferating tissue. Growth mechanism associated unrestricted cellular rearrangements are characterized with more ordered packing of cells.

properties, forces arising during division tend to minimize size differences between two daughter cells, which explains cellular topologies being similar to a random division scheme.

Tissue growth based on Hertwig's division scheme differs from the two cases mentioned above. In this case, the mitotic index is lower compared to random and asymmetric division schemes, indicating slower growth of tissue. Division perpendicular to the cell's longest axis favours more compact optimal packing of cell in tissues starting from early development stages. The growth of the central part of the tissue is then suppressed due to surrounding cells, which decreases the average mitotic index. All three division schemes are characterised by cell packing topologies similar to the ones observed in *Drosophila* wing disc [19]. However, mean frequencies of hexagonal cells are slightly higher for Hertwig's division rule.

We also considered the effects of cellular rearrangement defined by viscous damping with the coefficient  $\gamma$  on tissue growth. We considered two values of the damping coefficient, where cell movements along each other are partially penalized ( $\gamma = 10$ ) or not penalized at all ( $\gamma = 0$ ). We compared those two cases with the case of  $\gamma = 20$ ,

which was examined in the previous chapter. We found that the case where cellular rearrangements are not suppressed displays a different growth mechanism. When  $\gamma = 0$ , the cells were able to move freely and rearrange themselves to form structures close to optimal packing at the early stages of growth. The growth of the central part of the tissue is then restricted by the surrounding cells and overall tissue growth is mainly localized within a few outer cell layers. This inhomogeneous growth quickly terminates cell divisions inside the tissue and the absence of proliferation leads to optimal hexagonal packing. All three cases lead to similar tissue topologies in the proliferation regime, however unrestricted cell rearrangements favour cell packing topologies with a higher percentage of hexagons.



# Chapter 7

## Conclusions and Future Works

### 7.1 Conclusions

During the development of multicellular organisms, various tissues and organs develop from a single fertilized egg by means of cell growth and division. Properly functioning tissues have precise shapes, sizes and topologies; thus various cellular processes that alter tissue topology must be highly coordinated. The mechanisms that govern tissue growth and morphogenesis are not completely understood [18]. To address this issue, numerical methods have been extensively used [25, 26, 27, 28, 29, 30, 31, 32].

In this work, we have developed a novel mechanical model for cell divisions and tissue formation, suitable to study growth and cell packing topologies in two-dimensional tissues, like epithelium. In contrast to vertex models [27], where polygonal cells are defined as part of the existing network, we treat each cell in a more realistic manner, independent of its neighbors. In our model, we consider the cell's cortex contractility and cell-cell adhesion. Viscous damping is used to take into account the cytoplasmic cellular environment.

We introduced proliferation as a repeated cycle of cellular growth and division. To control cell growth, we used osmotic-like internal pressure. This particular choice of growth mechanism is inspired by observations on mitotic cells according to which cells modulate their internal hydrostatic pressure before divisions [11]. In our model, interplay between cortex contractility, adhesion, and internal pressure defines cell shapes and packing topologies in tissues. Both growth and division introduce an imbalance of net forces acting on each cell that governs changes in cell shapes and their local rearrangements. We used this model to numerically study the dynamics of growth and cell packing topologies in proliferating two-dimensional tissues and compared outcomes

with proliferating *Drosophila* wing disc.

*Drosophila* wing growth can be characterized by the mitotic index. The mitotic index changes throughout the wing development. It is higher at the initial stages of development, when growth is faster, and decreases over the time [83]. We examined the time dependency of the mitotic index in our model and found that the mitotic index decreases exponentially, similar to experiments [83]. We then studied cell packing topologies. Cell shapes in tightly packed epithelial tissues resemble polygons, therefore cell packing in epithelium can be characterized by the fraction of cells of different polygon types. We showed that our model reproduces commonly observed cell packing topology in proliferating epithelial tissues, with a peak at hexagons and an asymmetric distribution of heptagons and pentagons [19]. We established a parameter set that matches well with the experimentally observed *Drosophila* wing epithelium topology.

In addition to a randomly oriented symmetric division plane, we considered two alternative biologically relevant division schemes. First, we considered a randomly oriented asymmetric division planes producing daughter cells with different sizes. The plane was chosen such that consistently the larger daughter cell had an area twice as large as the area of the smaller daughter cell. We found that the size difference in two newly generated cells does not have a significant impact on tissue growth or cell packing topologies. Since both daughter cells are assigned the same mechanical properties and same internal pressure, the force imbalance introduced by the division tends to minimize the size difference, and cells obtain similar shapes and topologies in tissue. The second division scheme we considered is division based on Hertwig's rule. Here, the division plane is chosen perpendicular to cell's longest axis. We found that division based on Hertwig's rule induces tissue growth that differs from growth mediated by the other two schemes mentioned above. The mitotic index is overall lower compared to mitotic indices of random symmetric and asymmetric division schemes. This indicates slower growth. Hertwig's division scheme favours more compact, close to optimal, packing of cells in tissues starting from the early developmental stages. The growth of the central part of the tissue is then suppressed by surrounding cells, resulting in overall an lower mitotic index.

We investigated the effects of cellular rearrangements defined by viscous damping in our model. As we mentioned above, cells change their shapes and rearrange themselves in response to an imbalance in forces introduced by growth and divisions. The amount of cellular rearrangement is controlled by viscous damping with the coefficient  $\gamma$ . We considered two values of  $\gamma$ :  $\gamma = 10$  (partially restricted rearrangements) and

$\gamma = 0$  (unrestricted cellular rearrangements). When cell rearrangements were not penalized by damping ( $\gamma = 0$ ), the growth mechanism of the tissue was different from the case when a penalty was applied (e.g., the  $\gamma = 10$  and  $\gamma = 20$  cases). A damping coefficient of  $\gamma = 0$  leads to a more ordered packing structure starting from the early development stages. Then, the growth is suppressed and limited to mainly outer layers of tissue. As expected, the absence of proliferation is reflected in a low mitotic index as well as optimal hexagonal packing.

## 7.2 Future Work

*Drosophila* wing growth and patterning is controlled by the concentration gradient of morphogens, such as Decapentaplegic and Wingless [83, 85]. Decapentaplegic and Wingless are expressed along the anterior-posterior and dorsal-ventral axes of the wing correspondingly. Combined, both morphogens create a graded concentration profile. The concentrations and signalling levels of morphogens are higher at the central part of the tissue and gradually decrease towards the edges. In our model, cell growth is controlled by the internal pressure. All cells are assigned the same pressure which increases at a constant rate. Individual treatment of cells allows the growth mechanisms to be altered on a single cell level. In particular, one can assign different internal pressures to cells based on their positions in tissue in an attempt to mimic concentration gradient of morphogens. Such distributions of internal pressures correspond to a more realistic growth of the tissue.

In this thesis, we presented a two-dimensional model for cell divisions for tissues that effectively behave as two-dimensional sheets, such as epithelium. Our model can be extended to the three-dimensional case in a straightforward manner. Equations of motion that govern the time evolution of the system have the same form in three dimensions, as they do in two dimensions. However, a more complex network of springs is needed to model elastic three-dimensional spheroid-like structures that represent cells in three dimensions. The algorithm for cell growth may be transferred to the three-dimensional case without any changes. As for the division algorithm, a division plane consisting of an elastic spring network should replace the previously used division line. A three-dimensional extension of our model will provide better insight into the growth of real three-dimensional tissues.

# Bibliography

- [1] D. E. Koshland. The Seven Pillars of Life. *Science*, 295(5563):2215–2216, 2002.
- [2] H. Lodish. *Molecular Cell Biology*. Macmillan, New York, 5 edition, 2008.
- [3] <http://celldynamics.org/celldynamics/research/cytokinesis/>.
- [4] J. M. Scholey, I. Brust-Mascher, and A. Mogilner. Cell Division. *Nature*, 422(6933):746–752, 2003.
- [5] J. D. Wang and P. A. Levin. Metabolism, Cell Growth and the Bacterial Cell Cycle. *Nature Reviews Microbiology*, 7(11):822–827, 2009.
- [6] Boundless Microbiology Open Textbook. *Microbiology*. 2013.
- [7] L. Dupuy, J. Mackenzie, and J. Haseloff. Coordination of Plant Cell Division and Expansion in a Simple Morphogenetic System. *Proceedings of the National Academy of Sciences*, 107(6):2711–2716, 2010.
- [8] H. R. Horvitz and I. Herskowitz. Mechanisms of Asymmetric Cell Division: Two Bs or Not Two Bs, That is the Question. *Cell*, 68(2):237–255, 1992.
- [9] D. Hanahan and R. A. Weinberg. Hallmarks of Cancer: The Next Generation. *Cell*, 144(5):646–674, 2011.
- [10] T. J. Mitchison and E. D. Salmon. Mitosis: A History of Division. *Nature Cell Biology*, 3(1):17–21, 2001.
- [11] M. P. Stewart, J. Helenius, Y. Toyoda, S. P. Ramanathan, D. J. Muller, and A. A. Hyman. Hydrostatic Pressure and the Actomyosin Cortex Drive Mitotic Cell Rounding. *Nature*, 469(7329):226–230, 2011.
- [12] N. Minc, D. Burgess, and F. Chang. Influence of Cell Geometry on Division-plane Positioning. *Cell*, 144(3):414–426, 2011.

- [13] S. W. Grill. Forced to Be Unequal. *Science*, 330(6004):597–598, 2010.
- [14] J. A. Theriot and T. J. Mitchison. Actin Microfilament Dynamics in Locomoting Cells. *Nature*, 352(6331):126–131, 1991.
- [15] Ch. Roubinet, P. T. Tran, and M. Piel. Common Mechanisms Regulating Cell Cortex Properties During Cell Division and Cell Migration. *Cytoskeleton*, 69(11):957–972, 2012.
- [16] A. Tardieu and M. Delaye. Eye Lens Proteins and Transparency: From Light Transmission Theory to Solution X-ray Structural Analysis. *Annual Review of Biophysics and Biophysical Chemistry*, 17(1):47–70, 1988.
- [17] R. J. Wootton. Functional Morphology of Insect Wings. *Annual review of entomology*, 37(1):113–140, 1992.
- [18] O. Wartlick, P. Mumcu, F. Jülicher, and M. Gonzalez-Gaitan. Understanding Morphogenetic Growth Control: Lessons from Flies. *Nature Reviews Molecular Cell Biology*, 12(9):594–604, 2011.
- [19] M. C. Gibson, A. B. Patel, R. Nagpal, and N. Perrimon. The Emergence of Geometric Order in Proliferating Metazoan Epithelia. *Nature*, 442(7106):1038–1041, 2006.
- [20] D. Frenkel and B. Smit. *Understanding Molecular Simulation: From Algorithms to Applications*. Access Online via Elsevier, 2001.
- [21] P. Espanol and P. Warren. Statistical Mechanics of Dissipative Particle Dynamics. *EPL (Europhysics Letters)*, 30(4):191, 1995.
- [22] S.-Jan. Marrink and H. J. C. Berendsen. Simulation of Water Transport Through a Lipid Membrane. *The Journal of Physical Chemistry*, 98(15):4155–4168, 1994.
- [23] P. B. Canham. The Minimum Energy of Bending as a Possible Explanation of the Biconcave Shape of the Human Red Blood Cell. *Journal of Theoretical Biology*, 26(1):61–81, 1970.
- [24] M. Milán, S. Campuzano, and A. García-Bellido. Cell Cycling and Patterned Cell Proliferation in the Wing Primordium of *Drosophila*. *Proceedings of the National Academy of Sciences*, 93(2):640–645, 1996.

- [25] F. Graner and J. A. Glazier. Simulation of Biological Cell Sorting using a Two-Dimensional Extended Potts Model. *Physical Review Letters*, 69(13):2013, 1992.
- [26] J. Käfer, T. Hayashi, R. W. Marée, A. F. M. and Carthew, and F. Graner. Cell Adhesion and Cortex Contractility Determine Cell Patterning in the *Drosophila* Retina. *Proceedings of the National Academy of Sciences*, 104(47):18549–18554, 2007.
- [27] R. Farhadifar, J.-Ch. Röper, B. Aigouy, S. Eaton, and F. Jülicher. The Influence of Cell Mechanics, Cell-Cell Interactions, and Proliferation on Epithelial Packing. *Current Biology*, 17(24):2095–2104, 2007.
- [28] L. Hufnagel, A. A. Teleman, H. Rouault, S. M. Cohen, and B. I. Shraiman. On the Mechanism of Wing Size Determination in Fly Development. *Proceedings of the National Academy of Sciences*, 104(10):3835–3840, 2007.
- [29] E. Palsson and H. G. Othmer. A Model for Individual and Collective Cell Movement in *Dictyostelium Discoideum*. *Proceedings of the National Academy of Sciences*, 97(19):10448–10453, 2000.
- [30] D. Drasdo, R. Kree, and J. S. McCaskill. Monte Carlo Approach to Tissue-Cell Populations. *Physical Review E*, 52(6):6635, 1995.
- [31] T. J. Newman. Modeling Multi-Cellular Systems using Sub-Cellular Elements. *arXiv preprint q-bio/0504028*, 2005.
- [32] K. A. Rejniak, H. J. Kliman, and L. J. Fauci. A Computational Model of the Mechanics of Growth of the Villous Trophoblast Bilayer. *Bulletin of Mathematical Biology*, 66(2):199–232, 2004.
- [33] P. Sahlin and H. Jönsson. A Modeling Study on How Cell Division Affects Properties of Epithelial Tissues under Isotropic Growth. *PloS One*, 5(7):e11750, 2010.
- [34] T. Aegerter-Wilmsen, A. C. Smith, A. J. Christen, Ch. M. Aegerter, E. Hafen, and K. Basler. Exploring the Effects of Mechanical Feedback on Epithelial Topology. *Development*, 137(3):499–506, 2010.

- [35] K. A. Rejniak. An Immersed Boundary Framework for Modelling the Growth of Individual Cells: An Application to the Early Tumour Development. *Journal of Theoretical Biology*, 247(1):186–204, 2007.
- [36] A. R. A. Rejniak, K. A. and Anderson. A Computational Study of the Development of Epithelial Acini: I. Sufficient Conditions for the Formation of a Hollow Structure. *Bulletin of Mathematical Biology*, 70(3):677–712, 2008.
- [37] T. J. Newman. Grid-free Models of Multicellular Systems, with an Application to Large-Scale Vortices Accompanying Primitive Streak Formation. *Current Topics in Developmental Biology*, 81:157–182, 2008.
- [38] S. A. Sandersius and T. J. Newman. Modeling Cell Rheology with the Subcellular Element Model. *Physical Biology*, 5(1):015002, 2008.
- [39] S. A. Sandersius, M. Chuai, C. J. Weijer, and T. J. Newman. Correlating Cell Behavior with Tissue Topology in Embryonic Epithelia. *PloS One*, 6(4):e18081, 2011.
- [40] D. A. Lauffenburger and A. F. Horwitz. Cell Migration: A Physically Integrated Molecular Process. *Cell*, 84(3):359–369, 1996.
- [41] G. M. Cooper and R. E. Hausman. *The Cell*. ASM press Washington, 2000.
- [42] B. Lewin. *Cells*. Jones & Bartlett Learning, 2007.
- [43] H. Schiessel. The Physics of Chromatin. *Journal of Physics: Condensed Matter*, 15(19):R699, 2003.
- [44] R. B. Gennis. *Biomembranes: Molecular Structure and Function*. Springer-Verlag New York, 1989.
- [45] R. J. Pelham and F. Chang. Actin Dynamics in the Contractile Ring During Cytokinesis in Fission Yeast. *Nature*, 419(6902):82–86, 2002.
- [46] S. J. Singer and G. L. Nicolson. The Fluid Mosaic Model of the Structure of Cell Membranes. *Science*, 175(23):720–731, 1972.
- [47] K. Simons and E. Ikonen. Functional Rafts in Cell Membranes. *Nature*, 387(6633):569–572, 1997.

- [48] R. J. Cherry, P. R. Smith, I. E. G. Morrison, and N. Fernandez. Mobility of Cell Surface Receptors: A Re-Evaluation. *FEBS Letters*, 430(1):88–91, 1998.
- [49] G. Vereb, J. Szöllősi, J. Matko, P. Nagy, L. Farkas, T. and Vigh, L. Matyus, T. A. Waldmann, and S. Damjanovich. Dynamic, Yet Structured: The Cell Membrane Three Decades After the Singer–Nicolson Model. *Proceedings of the National Academy of Sciences*, 100(14):8053–8058, 2003.
- [50] Sh. Gadde and R. Heald. Mechanisms and Molecules of the Mitotic Spindle. *Current Biology*, 14(18):R797–R805, 2004.
- [51] Y.-L. Shih and L. Rothfield. The Bacterial Cytoskeleton. *Microbiology and Molecular Biology Reviews*, 70(3):729–754, 2006.
- [52] R. Lipowsky, E. Sackmann, et al. Handbook of Biological Physics. *Structure and Dynamics of Membranes*, 1, 1995.
- [53] Qi Wen and Paul A Janmey. Polymer Physics of the Cytoskeleton. *Current Opinion in Solid State and Materials Science*, 15(5):177–182, 2011.
- [54] U. S. Schwarz and S. A. Safran. Physics of Adherent Cells. *Reviews of Modern Physics*, 85(3):1327, 2013.
- [55] A. J. Levine, D. A. Head, and F. C. MacKintosh. The Deformation Field in Semiflexible Networks. *Journal of Physics: Condensed Matter*, 16(22):S2079, 2004.
- [56] P. A. Janmey. Mechanical Properties of Cytoskeletal Polymers. *Current Opinion in Cell Biology*, 3(1):4–11, 1991.
- [57] J. Stricker, T. Falzone, and M. L. Gardel. Mechanics of the F-actin Cytoskeleton. *Journal of Biomechanics*, 43(1):9–14, 2010.
- [58] A. Diz-Muñoz, M. Krieg, M. Bergert, I. Ibarlucea-Benitez, D. J. Muller, E. Paluch, and C.-Ph. Heisenberg. Control of Directed Cell Migration in Vivo by Membrane-to-Cortex Attachment. *PLoS Biology*, 8(11):e1000544, 2010.
- [59] H. Herrmann, H. Bär, L. Kreplak, S. V. Strelkov, and U. Aebi. Intermediate Filaments: From Cell Architecture to Nanomechanics. *Nature Reviews Molecular Cell Biology*, 8(7):562–573, 2007.



- [60] M. Schopferer, H. Bär, B. Hochstein, S. Sharma, N. Mücke, H. Herrmann, and N. Willenbacher. Desmin and Vimentin Intermediate Filament Networks: Their Viscoelastic Properties Investigated by Mechanical Rheometry. *Journal of Molecular Biology*, 388(1):133–143, 2009.
- [61] E. Nogales. Structural Insights into Microtubule Function. *Annual Review of Biochemistry*, 69(1):277–302, 2000.
- [62] M. Sato, W. H. Schwartz, S. Ch. Selden, and Th. D. Pollard. Mechanical Properties of Brain Tubulin and Microtubules. *The Journal of Cell Biology*, 106(4):1205–1211, 1988.
- [63] F. Gittes, B. Mickey, J. Nettleton, and J. Howard. Flexural Rigidity of Microtubules and Actin Filaments Measured from Thermal Fluctuations in Shape. *The Journal of Cell Biology*, 120(4):923–934, 1993.
- [64] M. Osawa, D. E. Anderson, and H. P. Erickson. Reconstitution of Contractile Ftsz Rings in Liposomes. *Science*, 320(5877):792–794, 2008.
- [65] W. Margolin. Sculpting the Bacterial Cell. *Current Biology*, 19(17):R812–R822, 2009.
- [66] S. Cooper. A Unifying Model for the G1 Period in Prokaryotes and Eukaryotes. *Nature*, 280(5717):17–19, 1979.
- [67] O. Michelsen, M. J. T. de Mattos, P. R. Jensen, and F. G. Hansen. Precise Determinations of C and D Periods by Flow Cytometry in *Escherichia coli* K-12 and B/r. *Microbiology*, 149(4):1001–1010, 2003.
- [68] L. G. Smith. Plant Cell Division: Building Walls in the Right Places. *Nature Reviews Molecular Cell Biology*, 2(1):33–39, 2001.
- [69] S. W. Grill and A. A. Hyman. Spindle Positioning by Cortical Pulling Forces. *Developmental Cell*, 8(4):461–465, 2005.
- [70] S. W. Grill, P. Goënczy, E. H. K. Stelzer, and A. A. Hyman. Polarity Controls Forces Governing Asymmetric Spindle Positioning in the *Caenorhabditis Elegans* embryo. *Nature*, 409(6820):630–633, 2001.
- [71] C. Cabernard, K. E. Prehoda, and C. Q. Doe. A Spindle-Independent Cleavage Furrow Positioning Pathway. *Nature*, 467(7311):91–94, 2010.

- [72] J. A. Knoblich. Asymmetric Cell Division: Recent Developments and Their Implications for Tumour Biology. *Nature Reviews Molecular Cell Biology*, 11(12):849–860, 2010.
- [73] T. Hayashi and R. W. Carthew. Surface Mechanics Mediate Pattern Formation in the Developing Retina. *Nature*, 431(7009):647–652, 2004.
- [74] W. T. Gibson and M. C. Gibson. Cell Topology, Geometry, and Morphogenesis in Proliferating Epithelia. *Current Topics in Developmental Biology*, 89:87–114, 2009.
- [75] U. Tepass, G. Tanentzapf, R. Ward, and R. Fehon. Epithelial Cell Polarity and Cell Junctions in *Drosophila*. *Annual Review of Genetics*, 35(1):747–784, 2001.
- [76] J. A. Zallen. Planar Polarity and Tissue Morphogenesis. *Cell*, 129(6):1051–1063, 2007.
- [77] Anne-Kathrin Classen, Kurt I Anderson, Eric Marois, and Suzanne Eaton. Hexagonal Packing of *Drosophila* Wing Epithelial Cells by the Planar Cell Polarity Pathway. *Developmental Cell*, 9(6):805–817, 2005.
- [78] J. T. Blankenship, S. T. Backovic, J. S. P. Sanny, O. Weitz, and J. A. Zallen. Multicellular Rosette Formation Links Planar Cell Polarity to Tissue Morphogenesis. *Developmental Cell*, 11(4):459–470, 2006.
- [79] L. L. Wong and P. N. Adler. Tissue Polarity Genes of *Drosophila* Regulate the Subcellular Location for Prehair Initiation in Pupal Wing Cells. *The Journal of Cell Biology*, 123(1):209–221, 1993.
- [80] B. M. Gumbiner. Cell Adhesion: The Molecular Basis of Tissue Architecture and Morphogenesis. *Cell*, 84(3):345–357, 1996.
- [81] A. Hornbruch and L. Wolpert. Cell Division in the Early Growth and Morphogenesis of the Chick Limb. *Nature*, 1970.
- [82] L. Wolpert, Ch. Tickle, Th. M. Jessell, P. Lawrence, E. Meyerowitz, E. Robertson, E. Lawrence, and M. McClements. *Principles of Development*, volume 3. Oxford University Press Oxford, 2002.

- [83] O. Wartlick, P. Mumcu, A. Kicheva, T. Bittig, C. Seum, F. Jülicher, and M. Gonzalez-Gaitan. Dynamics of Dpp Signaling and Proliferation Control. *Science*, 331(6021):1154–1159, 2011.
- [84] T. Aegerter-Wilmsen, M. B. Heimlicher, A. C. Smith, P. B. de Reuille, R. S. Smith, C. M. Aegerter, and K. Basler. Integrating Force-sensing and Signaling Pathways in a Model for the Regulation of Wing Imaginal Disc Size. *Development*, 139(17):3221–3231, 2012.
- [85] C. J. Neumann and S. M. Cohen. Long-range Action of Wingless Organizes the Dorsal-Ventral Axis of the *Drosophila* Wing. *Development*, 124(4):871–880, 1997.
- [86] B. I. Shraiman. Mechanical Feedback as a Possible Regulator of Tissue Growth. *Proceedings of the National Academy of Sciences of the United States of America*, 102(9):3318–3323, 2005.
- [87] T. Aegerter-Wilmsen, Ch. M. Aegerter, E. Hafen, and K. Basler. Model for the Regulation of Size in the Wing Imaginal Disc of *Drosophila*. *Mechanisms of development*, 124(4):318–326, 2007.
- [88] U. Nienhaus, T. Aegerter-Wilmsen, and C. M. Aegerter. Determination of Mechanical Stress Distribution in *Drosophila* Wing Discs Using Photoelasticity. *Mechanisms of Development*, 126(11):942–949, 2009.
- [89] Th. Schwann. *Microscopical Researches into the Accordance in the Structure and Growth of Animals and Plants*. Sydenham Society, 1847.
- [90] D. W. Thompson. On Growth and Form. 1942.
- [91] F. T. Lewis. The Effect of Cell Division on the Shape and Size of Hexagonal Cells. *The Anatomical Record*, 33(5):331–355, 1926.
- [92] F. T. Lewis. The Correlation Between Cell Division and the Shapes and Sizes of Prismatic Cells in the Epidermis of Cucumis. *The Anatomical Record*, 38(3):341–376, 1928.
- [93] R. W. Korn and R. M. Spalding. The Geometry of Plant Epidermal Cells. *New Phytologist*, 72(6):1357–1365, 1973.

- [94] A. B. Patel, W. T. Gibson, M. C. Gibson, and R. Nagpal. Modeling and Inferring Cleavage Patterns in Proliferating Epithelia. *PLoS Computational Biology*, 5(6):e1000412, 2009.
- [95] Th. Lecuit and P.-F. Lenne. Cell Surface Mechanics and the Control of Cell Shape, Tissue Patterns and Morphogenesis. *Nature Reviews Molecular Cell Biology*, 8(8):633–644, 2007.
- [96] A. R. A. Anderson, M. A. J. Chaplain, and K. A. Rejniak. *Single-Cell-Based Models in Biology and Medicine*. Springer, 2007.
- [97] R. Keller and M. Danilchik. Regional Expression, Pattern and Timing of Convergence and Extension During Gastrulation of *Xenopus Laevis*. *Development*, 103(1):193–209, 1988.
- [98] M. Chuai, W. Zeng, X. Yang, V. Boychenko, J. A. Glazier, and C. J. Weijer. Cell Movement During Chick Primitive Streak Formation. *Developmental Biology*, 296(1):137–149, 2006.
- [99] W.-T. Chen. Mechanism of Retraction of the Trailing Edge During Fibroblast Movement. *The Journal of Cell Biology*, 90(1):187–200, 1981.
- [100] E. Abu Shah and K. Keren. Mechanical Forces and Feedbacks in Cell Motility. *Current Opinion in Cell Biology*, 25(5):550–557, 2013.
- [101] R. J. Hawkins, R. Poincloux, O. Bénichou, M. Piel, P. Chavrier, and R. Voituriez. Spontaneous Contractility-Mediated Cortical Flow Generates Cell Migration in Three-Dimensional Environments. *Biophysical Journal*, 101(5):1041–1045, 2011.
- [102] P. Recho, Th. Putelat, and L. Truskinovsky. Contraction-Driven Cell Motility. *Physical Review Letters*, 111(10):108102, 2013.
- [103] Ch. S. Peskin. The Immersed Boundary Method. *Acta Numerica*, 11(0):479–517, 2002.
- [104] V. M Laurent, E. Planus, R. Fodil, and D. Isabey. Mechanical Assessment by Magnetocytometry of the Cytosolic and Cortical Cytoskeletal Compartments in Adherent Epithelial Cells. *Biorheology*, 40(1):235–240, 2003.

- [105] M. H. Sadd. *Elasticity: Theory, Applications, and Numerics*. Access Online via Elsevier, 2009.
- [106] L. D. Landau and E. M. Lifshitz. *Theory of Elasticity*, 1986.
- [107] L. D. Landau. *Fluid Mechanics: Volume 6 (Course of Theoretical Physics)*. 1987.
- [108] G. Falkovich. *Fluid Mechanics: A Short Course for Physicists*. Cambridge University Press, 2011.
- [109] D. S. Chandrasekharaiah and L. Debnath. *Continuum Mechanics*. Academic Press San Diego, 1994.
- [110] D. Leckband and J. Israelachvili. Intermolecular Forces in Biology. *Quarterly Reviews of Biophysics*, 34(2):105, 2001.
- [111] J. N. Israelachvili. *Intermolecular and Surface Forces*. Academic Press, 2011.
- [112] I.-E. Dzyaloshinskii, E. M. Lifshitz, and L. P. Pitaevskii. General Theory of Van Der Waals' Forces. *Physics-Uspekhi*, 4(2):153–176, 1961.
- [113] S. A. Safran. *Statistical Thermodynamics of Surfaces, Interfaces, and Membranes*. Addison-Wesley Reading, 1994.
- [114] D. Boal. *Mechanics of the Cell*. Cambridge University Press, 2012.
- [115] J. M. Halbleib and W. J. Nelson. Cadherins in Development: Cell Adhesion, Sorting, and Tissue Morphogenesis. *Genes & Development*, 20(23):3199–3214, 2006.
- [116] R. O. Hynes. Integrins: Bidirectional, Allosteric Signaling Machines. *Cell*, 110(6):673–687, 2002.
- [117] C. Selhuber-Unkel, T. Erdmann, M. Lopez-Garcia, U. S. Kessler, H. and Schwarz, and J. P. Spatz. Cell Adhesion Strength is Controlled by Intermolecular Spacing of Adhesion Receptors. *Biophysical Journal*, 98(4):543–551, 2010.
- [118] S. Sarda, D. Pointu, F. Pincet, and N. Henry. Specific Recognition of Macroscopic Objects by the Cell Surface: Evidence for a Receptor Density Threshold

- Revealed by Micrometric Particle Binding Characteristics. *Biophysical Journal*, 86(5):3291–3303, 2004.
- [119] H. J. C. Berendsen. Molecular Dynamics Simulations: The Limits and Beyond. In *Computational Molecular Dynamics: Challenges, Methods, Ideas*, pages 3–36. Springer, 1999.
- [120] R. W. Pastor. Techniques and Applications of Langevin Dynamics Simulations. In *The Molecular Dynamics of Liquid Crystals*, pages 85–138. Springer, 1994.
- [121] S. E. Feller, Y. Zhang, R. W. Pastor, and B. R. Brooks. Constant Pressure Molecular Dynamics Simulation: The Langevin Piston Method. *The Journal of Chemical Physics*, 103:4613, 1995.
- [122] G. S. Grest and K. Kremer. Molecular Dynamics Simulation for Polymers in the Presence of a Heat Bath. *Physical Review A*, 33(5):3628, 1986.
- [123] R. Kubo. The Fluctuation-Dissipation Theorem. *Reports on Progress in Physics*, 29(1):255, 1966.
- [124] G. K. Gupta, R. Sacks-Davis, and P. E. Tescher. A review of Recent Developments in Solving ODEs. *ACM Computing Surveys (CSUR)*, 17(1):5–47, 1985.
- [125] L. Kong, R. Liu, and X. Zheng. A Survey on Symplectic and Multi-Symplectic Algorithms. *Applied Mathematics and Computation*, 186(1):670–684, 2007.
- [126] L. Verlet. Computer “Experiments” on Classical Fluids. I. Thermodynamical Properties of Lennard-Jones Molecules. *Physical Review*, 159(1):98, 1967.
- [127] D. C. Rapaport. *The Art of Molecular Dynamics Simulation*. Cambridge University Press, 2004.
- [128] W. C. Swope, H. C. Andersen, P. H. Berens, and K. R. Wilson. A Computer Simulation Method for the Calculation of Equilibrium Constants for the Formation of Physical Clusters of Molecules: Application to Small Water Clusters. *The Journal of Chemical Physics*, 76:637, 1982.
- [129] W. F. van Gunsteren and H. J. C. Berendsen. Computer Simulation of Molecular Dynamics: Methodology, Applications, and Perspectives in Chemistry. *Angewandte Chemie International Edition in English*, 29(9):992–1023, 1990.

- [130] Sh.-sh. Wang and J. A. Krumhansl. Superposition Assumption. II. High Density Fluid Argon. *The Journal of Chemical Physics*, 56:4287, 1972.
- [131] F. Aurenhammer. Voronoi Diagrams: A Survey of a Fundamental Geometric Data Structure. *ACM Computing Surveys (CSUR)*, 23(3):345–405, 1991.
- [132] E. Wigner and F. Seitz. On the Construction of Metallic Sodium. *Phys. Rev.*, 43(804).
- [133] A. H. Thiessen. Precipitation Averages for Large Areas. *Monthly Weather Review*, 39(7):1082–1089, 1911.
- [134] J. A. Åström and M Karttunen. Cell Aggregation: Packing Soft Grains. *Physical Review E*, 73(6):062301, 2006.
- [135] P. Kunda, A. E. Pelling, T. Liu, and B. Baum. Moesin Controls Cortical Rigidity, Cell Rounding, and Spindle Morphogenesis During Mitosis. *Current Biology*, 18(2):91–101, 2008.
- [136] A. J. Ridley, M. A. Schwartz, K. Burridge, R. A. Firtel, M. H. Ginsberg, G. Borisy, J. Th. Parsons, and A. R. Horwitz. Cell Migration: Integrating Signals from Front to Back. *Science*, 302(5651):1704–1709, 2003.
- [137] G. T. Charras, Ch.-K. Hu, and T. J. Coughlin, M. and Mitchison. Reassembly of Contractile Actin Cortex in Cell Blebs. *The Journal of Cell Biology*, 175(3):477–490, 2006.
- [138] A. Garcia-Bellido and J. R. Merriam. Parameters of the Wing Imaginal Disc Development of *Drosophila* Melanogaster. *Developmental Biology*, 24(1):61–87, 1971.

# Curriculum Vitae

**Name:** Anna Mkrtchyan

**Post-Secondary Education and Degrees:**

|   |                  |           |
|---|------------------|-----------|
| Yerevan State University<br>M.Sc in Physics | Yerevan, Armenia | 2005-2007 |
| Yerevan State University<br>B.Sc in Physics | Yerevan, Armenia | 2001-2005 |

**Honours and Awards:**

|                                 |           |
|---------------------------------|-----------|
| Ontario Graduate Scholarship    | 2013-2014 |
| Graduate Student Teaching Award | 2013      |

**Related Work Experience:**

|   |                 |           |
|---|-----------------|-----------|
| Teaching Assistant<br>The University of Western Ontario | London, Ontario | 2009-2013 |
|---|-----------------|-----------|

**Publications:**

A. Mkrtchyan, J. Åström, M. Karttunen. A new model for cell division and migration with spontaneous topology changes. *Soft Matter* (2013). *submitted*.

T. Hynninen, C.L. Dias, A. Mkrtchyan, V. Heinonen, M. Karttunen, A.S. Foster, T. Ala-Nissila. A molecular dynamics implementation of the 3D Mercedes-Benz water model. *CPC*, 183(2) pp 363-369 (2012).

Y. Mamasakhlisov, B. A. Todd, A. Badasyan, A. Mkrtchyan, V. Morozov, V. A. Parsegian. DNA stretching and multivalent cation-induced condensation. *Phys. Rev. E*, 80(3), 031915 (2009).